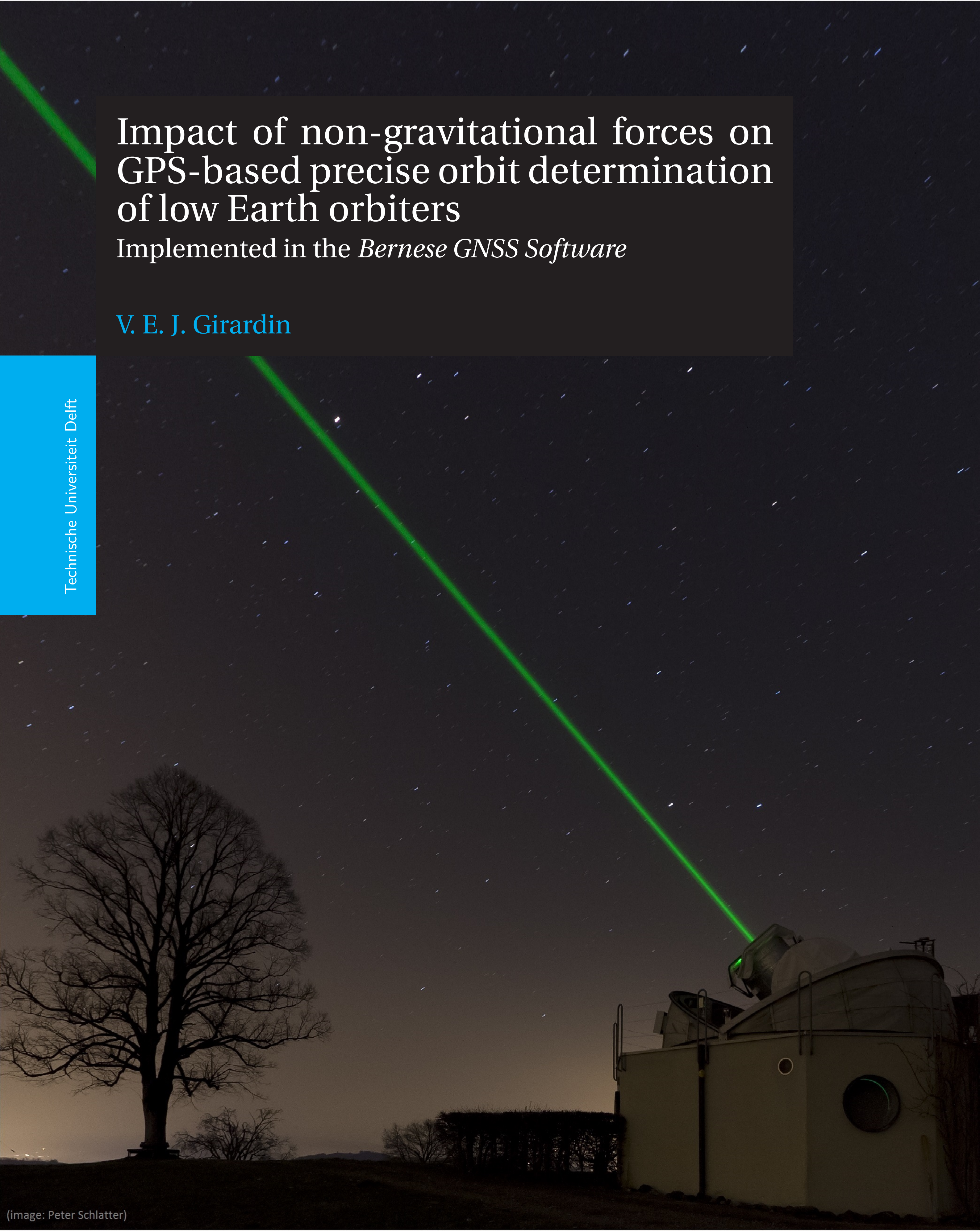

Impact of non-gravitational forces on GPS-based precise orbit determination of low Earth orbiters

Implemented in the *Bernese GNSS Software*

V. E. J. Girardin

Technische Universiteit Delft

(image: Peter Schlatter)

TU Delft Delft University of Technology

AIUB

Challenge the future

IMPACT OF NON-GRAVITATIONAL FORCES ON GPS-BASED PRECISE ORBIT DETERMINATION OF LOW EARTH ORBITERS

IMPLEMENTED IN THE *Bernese GNSS Software*

by

V. E. J. Girardin

in partial fulfillment of the requirements for the degree of

Master of Science
in Applied Physics

at the Delft University of Technology,
to be defended publicly on Thursday October 13, 2016 at 2:00 PM.

Registration number : 091#16#MT#FPP

Supervisors:	Prof. dr. ir. P. N. A. M. Visser,	Chair, TU Delft, Astrodynamics and Space missions
	Prof. dr. A. Jäggi,	Chair, AIUB (University of Bern), Physics and Astronomy
	Dr. D. Arnold,	AIUB (University of Bern)
Thesis committee:	Prof. dr. ir. P. N. A. M. Visser,	Chair, TU Delft, Astrodynamics and Space missions
	Prof. dr. A. Jäggi,	Chair, AIUB (University of Bern), Physics and Astronomy
	Dr. ir. E. J. O. Schrama,	TU Delft, Astrodynamics and Space missions
	Ir. P. P. Sundaramoorthy	TU Delft, Space Systems Engineering
	Dr. D. Arnold,	AIUB (University of Bern)

This thesis is confidential and cannot be made public until December 31, 2016.

ABSTRACT

The modelling of non-gravitational forces acting on a satellite (especially a GNSS satellite) started half a century ago. Their modelling to low Earth orbiters (LEOs), however, are more recent because of the dominating atmospheric drag, the modelling of which requires the precision of recent atmospheric models.

However, this is not an issue for precise orbit determination (POD), as of the method used to compute the reduced-dynamic orbit. The method is using piecewise constant accelerations (PCA), which are absorbing the non-conservative forces that are not modelled. One expects the implementation of non-gravitational forces to reduce the amplitude and mean values of the PCA of the satellite's reduced-dynamic orbit.

In this thesis assignment, four non-gravitational forces has been considered large enough for improving the POD of GPS-based LEO using the Bernese-GNSS Software: the aerodynamic forces, the solar radiation pressure and the reflected and emitted Earth radiation pressure.

For each force, a modelling method has been chosen and implemented into the Bernese GNSS Software. The impact of the modelled non-gravitational forces has been evaluated with Swarm and GRACE LEOs with all the available validation and comparison methods: PCA, accelerometer data, GPS observation fit, satellite laser ranging observations and K/Ka-band ranging measurements.

As expected, the implementation of all the forces reduces the standard deviation of the PCA in each direction, for both Swarm C (-8% in radial, -56% in along-track and -22% in cross-track) and GRACE A (-73% in radial, -75% in along-track and -20% in cross-track). Regarding the mean values for Swarm C a large reduction is observed in: along-track (-129%) and cross-track (-97%) direction, but the mean acceleration in radial direction increase by a few percent (7%). For GRACE A the mean values of the PCA are reduced along each orbital axis (-88% in radial, -112% in along-track and -23% in cross-track). In addition to the PCA reduction, the precision of the reduced-dynamic orbit has also been improved by the modelling of the non-gravitational forces. In terms of values an *a posteriori* σ of unit weight of 1.96 mm has been reduced to 1.93 mm for Swarm and from 2.3 mm to 1.45 mm for GRACE.

Finally, different parameterizations of the aerodynamic forces (the largest at LEO altitude) have been carried out in order to determine the best atmospheric model and gas-surface interaction algorithm for LEO POD improvement. The impact of a horizontal wind model has been tested. More specifically; modelling the gas-surface interaction with Goodman's model using the DTM2013 atmospheric model with the horizontal wind correction HWM14 have shown the best results in LEO POD.

Keywords : Bernese GNSS Software, GRACE, K/Ka-band ranging (KBR), Low Earth Orbiter (LEO), Non-gravitational forces modelling, piecewise constant accelerations (PCA), reduced-dynamic orbit, Satellite Laser Ranging (SLR), Swarm

PREFACE

This Master thesis assignment has been a cooperation between the Delft University of Technology (TU Delft) in the Netherlands and the Astronomical Institute of the University of Bern (AIUB) in Switzerland. This long assignment took nine months to find the relevant non-conservative forces, find out the most suitable algorithms, implement the models and finally, test and validate the new orbits.

Dealing with such a broad topic required great effort, creativity and imagination, but in the end this project has been very rewarding. Understanding the cutting-edge field of precise orbit determination of low Earth orbiters and contributing to improving the complex and powerful *Bernese GNSS Software* has been a great experience for me. I take this opportunity to thank Prof. Dr. Ir. P. N. A. M. Visser, Prof. Dr. A. Jäggi and Dr. D. Arnold for their patience, who sometimes spent more time teaching me English than Physics. A special thanks to Dr. D. Arnold for his generous support and valued insights into the encountered problems throughout the whole assignment. I also would like to address a cordial thanks to Dr. E. Doornbos for giving me the unique opportunity to individually compare my models with the data he computed himself.

Fruit d'une coopération entre l'École Polytechnique de Delft (TU Delft) aux Pays-Bas et l'Institut d'Astronomie de l'Université de Berne (AIUB) en Suisse, ce travail de Master a duré plus de neuf mois afin de parvenir aux objectifs fixés. Du choix des forces non-gravitationnelles adéquates à la validation des nouvelles orbites en passant par l'implémentation et les tests nécessaires, des efforts considérables ont été déployés. Ce fut aussi très enrichissant de travailler avec des experts dans un domaine de pointe telle que la détermination précise d'orbites de satellites, et de finalement contribuer à l'amélioration du fameux « Bernese GNSS Software ». Par ailleurs, je tiens à remercier mes superviseurs, Prof. Dr. Ir. P. N. A. M. Visser, Prof. Dr. A. Jäggi and Dr. D. Arnold, pour leur patience, qui parfois ont passé plus de temps à corriger mon anglais que mon travail. Je remercie en particulier Dr. D. Arnold pour sa précieuse aide tout au long de mon projet. Je souhaite également remercier Dr. E. Doornbos pour m'avoir donné l'unique opportunité de vérifier mes modèles séparément, en me fournissant généreusement les même données qu'il á calculées lui-même.

V. E. J. Girardin
Bourrignon (Switzerland), September 2016

CONTENTS

LIST OF FIGURES

LIST OF TABLES

1

INTRODUCTION

1.1. CONTEXT

The low Earth orbit provides the best condition to study the atmosphere, oceans, meteorology and the gravity field. For all of the satellite applications, the position of the satellite is of prime importance. Indeed for highly precise applications, knowing the exact location of the satellite largely improves the quality and precision of the measurements. Explicitly compute the non-gravitational forces do not necessarily increase the precision of the orbit. The Precise Orbit Determination (POD) can make use of the estimation of pseudo-stochastic orbit parameters like piecewise constant accelerations (PCA) to determine the reduced-dynamic orbit of the satellite. The piecewise constant accelerations are absorbing the non-gravitational forces, if they are not accounted for. In other words, the reduced-dynamic orbit determination that uses PCA, indirectly accounts for the non-gravitational forces even if they are not explicitly modelled. Implementing the non-gravitational forces into the *Bernese GNSS Software*[1] has other beneficial factors, not just improving the reduced-dynamic orbit. First, a better understanding of the non-gravitational forces would ensure that the PCA are properly modelled. Secondly, when implemented the non-conservative forces should reduce the PCA for a similar reduced-dynamic orbit, which is considered as an improvement. To a larger extent, precise modelling of the non-gravitational perturbations action on Low Earth Orbiters (LEOs) would lead to finer atmospheric models, more accurate gravity field measurements and to more precise atmospheric re-entry trajectories. An accurate modelling of the non-gravitational forces, combined with today's precise gravity field model could lead to longer orbit predictions. Such a capability is useful if a satellite becomes uncontrollable or if communication is lost. This means risks of satellite collisions would be reduced. In addition, a better understanding of the forces acting on satellite helps when designing spacecraft's for longer lasting, safer missions.

In this project, the relevant forces for LEO POD improvement will be first identified in literature. Secondly, for each relevant force, a modelling method will be chosen (based on the available resources). Thirdly, they will be implemented into the *Bernese GNSS Software* and tested. Finally, their POD impact will be assessed on LEOs of two different satellite missions, namely Swarm and Gravity Recovery And Climate Experiment (GRACE), see Sec. 5.2. Testing the models onto two different types of satellites shows the credibility and the adaptability of each model implemented. Due to its ultra-precise K-band instrument, GRACE offers additional validation possibilities.

One will see that the parameterization leading to the largest improvement is not unanimously defined. For this reason, several parameterizations will be tested in order to "experimentally" find out which parameterization shall be used.

---

[1] Developed by the Astronomical Institute of the University of Bern (AIUB) in Switzerland, the *Bernese GNSS Software* is a high-precision multi-GNSS data processing software [3].

1.2. CHAPTER OVERVIEW

Chapter 2 presents most of the existing non-gravitational perturbations and shows by means of literature that only four are relevant for LEOs. Namely atmospheric drag, Solar Radiation Pressure (SRP), emitted and reflected Earth Radiation pressure (ERP).

Chapter 3 focuses on the aerodynamic forces, cased by Gas-Surface Interaction (GSI) of atmospheric particles with the satellite surface. Starting with a literature study that reviews how the techniques to compute the atmospheric drag have evolved. It will be shown that one model of computing the GSI became a benchmark, but one parameter called "accommodation coefficient" is controversial.

Chapter 4 concentrates on radiation pressure, arising from photon-surface interactions of the satellite with any powerful source of photons. First, the physics underlying the photon-surface interaction is addressed and detailed. Then the three main sources of radiation pressure are mathematically described; direct solar rays, the solar rays reflected by the Earth's surface (or atmosphere) and the infrared (IR) rays emitted by the Earth.

In Chapter 5 the requirements and technical aspects of the implementation are addressed. First, the way non-gravitational accelerations are introduced in the *Bernese GNSS Software* for POD is portrayed. Then, the implementation of models of Earth and the LEOs, required to compute the surface force is discussed. Finally, a few tests conducted to check the implementation correctness are presented.

Chapter 6 compares the modelled non-gravitational accelerations of Swarm with the ones computed by E. Doornbos, who kindly gave me this precious data. In addition, the impact of different parametrizations will be evaluated.

Chapter 7 assesses the impact of the implemented forces on the orbits of GRACE and Swarm. Statistics are provided for all the validation methods used: accelerometer data, piecewise constant accelerations, GPS data fit, Satellite Laser Ranging (SLR) and K/Ka-Band Ranging (KBR).

In Chapter 8 the orbits using different parameterizations for the computation of the aerodynamic forces are compared. The setting that gives the smallest difference w.r.t. the observations is determined with the orbital validation methods described in Chapter 7.

Finally Chapter 9 recalls the important results of Chapters 6, 7 and 8, and draws a conclusion. A critical assessment is given about the implemented models, their weaknesses, limits and inconsistencies, of which would require more tests to achieve a higher reliability and quality. Finally, a short subsection addresses the recommendations for further improvements that could be applied to the implemented models.

2

TYPES OF NON-GRAVITATIONAL FORCES

In this Chapter, known non-gravitational perturbations acting on orbiting spacecrafts will be discussed, in order to determine which forces shall be implemented for LEO POD. Based on the target satellites several perturbations can be safely neglected.

Different types of satellites will be discussed in this chapter, as satellites can come in different shapes and sizes, meaning each satellite will encompass different properties. This deviation in form and size must be considered for each satellite due to the perturbations acting on them.

The Earth observation satellite ERS-1[1] (Fig. 2.1) was orbiting at LEO altitude, the cannonball satellite LAGEOS (Fig. 2.2) orbiting at medium Earth orbit (MEO) altitude and the Galileo satellite (Fig. 2.3) orbiting at MEO altitude.

Figure 2.1: Earth observation satellite, ERS-1 (Courtesy by ESA)

Figure 2.2: Cannonball satellite LAGEOS, (Courtesy by NASA)

Figure 2.3: High Earth orbiter, GNSS Galileo (Courtesy by ESA)

In general, non-gravitational forces are a result of momentum exchange of particles (or photons) with the satellite surface [4], or due to photons emitted by the satellite. Most of the known non-gravitational perturbations that are likely to act on spacecraft and the respective corrections are listed below.

- Aerodynamic forces due to the electrically neutral atmosphere
- Aerodynamic forces due to charged particles
- Aerodynamic forces from interplanetary dust
- Aerodynamic forces from space debris
- Direct solar radiation pressure
    - Penumbra correction

---

[1] The first European Remote-Sensing Satellite (ERS-1) has been launched in 1991 in order to study and monitor changes of the Earth atmosphere.

  - Solar irradiance variation
  - Poynting-Robertson effect
  - Light aberration
- Earth emitted radiation pressure
- Earth reflected radiation pressure
- Moon emitted radiation pressure
- Moon reflected radiation pressure
- Thermal satellite re-radiation[2]
  - The Yarkovsky effect
  - The Yarkovsky-Schach effect
- Antenna thrust
- Earth magnetic field perturbation

One has to consider the altitude of the satellites: Low Earth orbiters are orbiting below 1600 km or 2000 km above sea level (it is a matter of definition) [5]. However, most of LEOs (such as Swarm and GRACE that will be used for validation) are below 1000 km where the atmospheric drag is expected to be the strongest force, followed by the solar radiation pressure [6]. So those two forces shall be implemented, but they can be of different nature and involve several corrections.

The aerodynamic forces are caused by interactions of the satellite surface with a particle (charged or neutral), or with a larger object (dust or debris). First the **charged particles** are neutral atmospheric particles ionized by solar radiations, they are much less abundant at LEO altitude than high orbits [7]. This point is stressed by X. Zhu who claims, "The thermosphere is subject to additional electric and magnetic forces, not important in the middle and lower atmosphere, due to its partially ionized atmosphere" [8]. There is another source of ionised particles: the solar wind. However, most of the particles are canalised by the Van Allen radiation belts and remain within the belts, due to the Lorentz force. Charged particles coming from the Sun are only abundant there. Furthermore, the inner radiation belt does not stand below an altitude of 1000 km, since most of LEOs (such as Swarm and GRACE) are orbiting beneath the inner belt it is not relevant to implement the charged particles drag for LEO POD. Secondly, the **aerodynamic forces due to neutral particles** are by far the largest non-gravitational forces acting on LEO [6] because atmospheric particles are still present at LEO altitude. Finally, forces caused by **interplanetary dust** and **orbital debris**. The latter is expected to increase due to human activity at LEO altitude [9]. But their influence is estimated to be a negligible 1/10000 of the SRP [4]. Additionally, the largest populations of orbital debris are situated from 900 km to 1000 km and from 1400 km to 1500 km above see level [9]. Indeed they are at the LEO altitude, but since Swarm and GRACE are well below it, it is safe to not account for interplanetary dust and orbital debris drag in this project.

The **direct solar radiation pressure** is the second largest non-conservative force acting on a LEO below 1000 km [6]. Note that SRP is the largest non-conservative force at higher altitude, therefore its magnitude is often used as reference when comparing non-gravitational forces. Precisely modelling the SRP involves a few different phenomena: penumbra correction of SRP, solar irradiance variation, Poynting-Robertson effect and light aberration. However, they are not all relevant for LEO POD. First the **penumbra correction of SRP** is due to Sun's disc partially shadowed by the Earth when the satellite enters or leaves the Earth shadow (i.e. when it is in partial eclipse). Taking this into account ensures a smoother and more accurate transition between eclipse and sunlight. Therefore, it will be implemented for a better result. Different algorithms exist to compute the correction of SRP due to penumbra. Simple methods such as given by [6] or [10] are preferred over complex ones like [11] or [12]. Very precise penumbra correction of SRP modelling but are not expected to have a visible impact on POD. Secondly, the **solar irradiance variation** is about 1.4 W/m^2 during one Solar cycle [13]. A Solar cycle lasts between 9 and 14 years, leading to a negligible impact over the complete cycle [13]. Thirdly, the **Poynting-Robertson drag** is due to a higher momentum of the re-emitted blue-shifted photons in the direction of motion, which is only 1/10000 of the SRP [4]. This effect is negligible for precise orbit determination purposes. Finally, the **light aberration** has been theoretically discovered by

---

[2] It is also called thermal force, or thermal re-emission.

James Bradeley around 1728 [14]. Using Eq. 2.1 from [14], one can compute the magnitude of the correction due to light aberration. For a typical LEO with a relative atmospheric speed of about 7000 m/s, the light aberration correction ($\vec{a}_{rad}/\vec{a}'_{rad}$) represents a reduction of 2/100000 of the SRP. Obviously it can be safely neglected for LEO POD of arcs covering only one day.

$$\|\vec{a}'_{rad}\| = \|\vec{a}_{rad}\|\left(1 - \frac{\|\vec{V}_{sat}\|}{c}\right) \tag{2.1}$$

$\vec{a}'_{rad}$	radiation acceleration corrected with the light aberration
$\vec{a}_{rad}$	radiation acceleration
$\vec{V}_{sat}$	satellite velocity
c	speed of light

The Earth radiation pressure includes both the sunlight reflected by the Earth atmosphere or surface (i.e. the albedo) and the thermal IR radiations emitted by the Earth. **Reflected radiation pressure** can be up to 35% of the SRP [15], so this force should not be neglected. **IR emitted radiation pressure** is smaller than the reflected one. However, it is acting day and night with an average acceleration of 17% of the SRP [6]. Those forces are assumed large enough for LEO POD improvement, thus will be implemented.

The **Moon radiation pressure** is never mentioned in literature, thus cannot be assumed negligible. The Moon radiation pressure force has been modelled close to full Moon conditions (i.e. when the pressure force is the largest) and it is only 1/10000000 of the SRP (see Appendix B). It will be excluded for future POD.

The **re-radiation forces** of a spacecraft can be up to 10% of the SRP for GNSS satellites[3] [16]. This force is due to the heating of the satellite after being exposed to SRP and ERP, where the contribution of the ERP to the thermal force is less than 1% [16]. In addition, modelling the thermal re-radiation raises the problem of knowing accurate panel properties. As stated by E. Doornbos about thermal force : "Highly-detailed surface properties and temperature information, and complicated computations are required" [17]. Unfortunately, the required surface properties for computing the thermal force are not accessible for this project. Furthermore, inaccurate estimation of the parameters can lead to largely different results [18]. For those reasons, the thermal force will not be implemented in this project. It would then be inconsistent to implement smaller forces: to be implemented, we decide that a force must at least reach 10% of the SRP. The effects due to IR re-radiation coupled with thermal inertia, i.e. **Yarkovsky effect** and **Yarkovsky-Schach effect**, will thus not be implemented [4].

In principle, satellites are electromagnetically neutral, ergo the **Earth's magnetic field** does not create any force on them. However, part of their surface may become charged after a collision with an atmospheric particle or by photoelectric effect with radiations. While the magnetic field slows down the rotation of canonball satellites such as LAGEOS [19], it also creates a Lorentz force likely to modify the satellite's orbit. According to [4], it is approximately 1/20000 of the SRP, thus negligible.

A GNSS satellite with a powerful emitting antenna can be affected by the **antenna thrust**, a small acceleration pointing into the direction opposite to the antenna.. This thrust is comparable (in terms of magnitude) with reflected ERP [16]. However, LEO S-band antenna maximal power is 10 times smaller [20] than GNSS antenna. Unlike GNSS, they are not continuously emitting, therefore it is too small to produce any relevant thrust for POD.

Table 2.1 summarizes some of the surface forces estimated by "Deutsches Geodätisches Forschungsinstitut" (DGFI) for ERS-1 satellite [4]. Indeed the values in this table have been estimated for a satellite orbiting at 800 km (300 km higher than Swarm or GRACE). Therefore Table 2.1 only intends to give the reader an idea of the non-conservative forces' orders of magnitude.

Based on the discussion above, 4 non-gravitational forces (See Fig. 2.4) are considered relevant for LEO POD: aerodynamic forces (i.e. atmospheric drag and lift), direct solar radiation pressure (with the penumbra correction) and emitted and reflected Earth radiation pressure. While most of the orbital results are presented in Chapters 7 and 8, the influence of the individual models are assessed in Chapter 6 and Appendix E.

---

[3] LEOs are closer to the Earth surface, which means ERP is expected to be smaller for GNSS satellites. On the other hand GNSS satellite have larger solar cells always facing the Earth, which have higher absorption and thermal emissivity coefficients magnifying the thermal re-emission. Consequently, it is difficult to know whether or not the re-radiation forces is larger on LEOs.

Non-gravitational force	**Prevailing direction**	**DGFI Estimated Magnitude (m/s^2)**
Neutral atmospheric drag	along-track	$6 \cdot 10^{-8}$
Charged, particle drag	along-track	$5 \cdot 10^{-11}$
Direct solar radiation pressure	sun-satellite	$6 \cdot 10^{-8}$
Earth albedo radiation pressure	radial	$6 \cdot 10^{-9}$
Earth IR radiation pressure	radial	$6 \cdot 10^{-9}$
Yarkovsky-Schach effect	sun-satellite	$2 \cdot 10^{-9}$
Poynting-Robertson effect	along-track	$3 \cdot 10^{-12}$
Electromagnetic forces	perpendicular to velocity	$3 \cdot 10^{-13}$
Drag from interplanetary dust	along-track	$1 \cdot 10^{-12}$

Table 2.1: Orders of magnitude of the non-gravitational perturbations estimated for ERS satellites at 800 km altitude. For Swarm and GRACE (around 500 km altitude), atmospheric drag will be dominant and much bigger than SRP.

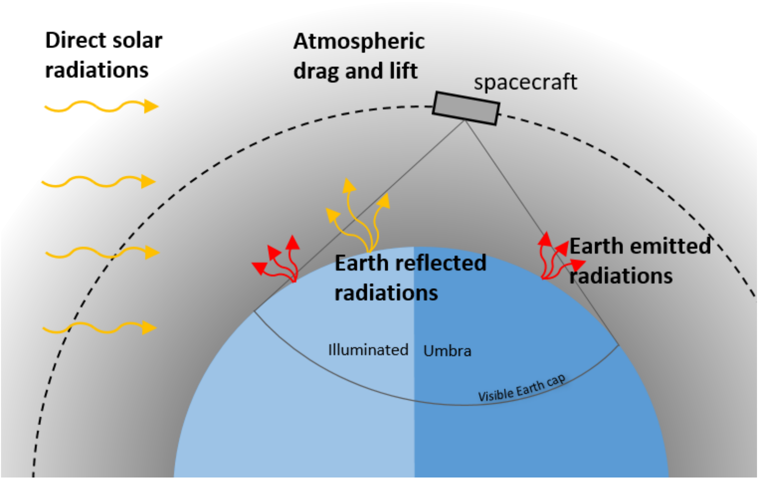

Figure 2.4: Graphical representation of the four relevant non-gravitational forces acting upon LEOs

3

AERODYNAMIC FORCES

This Chapter includes the mathematical description of the aerodynamic forces that will be implemented in the *Bernese GNSS Software*. The differences in algorithms used to model the aerodynamic forces will be focused on acutely.

3.1. GENERAL ASPECTS

At LEO altitude the aerodynamic forces are not a consequence of pressure unbalance or viscosity, as it is for an aircraft, but are due to interactions between the satellite surface and individual particles (molecules, atoms, ions). Due to the change in momentum of the particle hitting the satellite, these interactions lead to a drag force acting in the opposite direction of the LEO's velocity. When the satellite surface is not perpendicular to the flow, the interaction can also lead to a small force perpendicular to the velocity. By convention this force is called "lift". Therefore both are categorized as "aerodynamic" forces, even though their origin is not the same as lift and drag forces of an aircraft. The drag and lift forces are given by [21]

$$\vec{F}_{D,L} = \frac{1}{2}\rho\vec{v}^2 A_{ref} C_{D,L}\vec{e}_{D,L}, \tag{3.1}$$

where the reference area A_{ref} is the projected area of the satellite along the velocity axis. It is also common to use the so-called ballistic coefficient b or its inverse B (Eq. 3.2). However, the ballistic coefficient can vary by a large factor [22], meaning it will not be used in this assignment.

$$B = \frac{1}{m}\frac{1}{b} = C_D\frac{A_{ref}}{m}. \tag{3.2}$$

ρ	atmospheric density
$\vec{v}$	velocity of satellite w.r.t. the atmosphere
A_{ref}	reference area
$C_{D,L}$	drag and lift coefficients
$\vec{e}_{D,L}$	unit vectors in direction of drag and lift force
m	satellite mass

So far most scientific articles agree with the theory. They start deviating with the definition of C_D and C_L.

3.2. MATHEMATICAL MODELS

In this section, the algorithms used today to model the aerodynamic drag and lift are derived from early theoretical methods. The derivation of nowadays models has not been found in literature, therefore it is detailed in this section.

3.2.1. GAS-SURFACE INTERACTION

With the purpose of finding the most realistic equations to compute the atmospheric drag of LEO satellites, different methods have been investigated during the last decades. An overview of the existing descriptions of

GSI (gas-surface interaction) is given in [23], so will not be repeated here. It will be shown how the models have evolved into recent[1] ones.

The first two scientists, who rigorously set up the basics of GSI for determining the drag and lift coefficients, were Lee H. Sentman [1] and R. Schamberg [25] half a century ago. They both assumed that the satellite is moving in a “free molecular flow”, which implies that the collisions between gas molecules are negligible[2]. In addition the satellite surface is assumed to be convex, such that each gas molecule can be reflected only once. The point of divergence between Sentman and Schamberg was about the nature of the gas molecules in the upper atmosphere and the nature of the reflection at the satellite surface.

Sentman assumed that the incident and reflected molecules were in equilibrium with themselves. As a consequence the kinetic theory states that their velocities are specified by the Maxwellian velocity distribution corresponding to the atmospheric temperature [24]. He also assumed that the reflection is solely diffuse (Fig. 3.1).

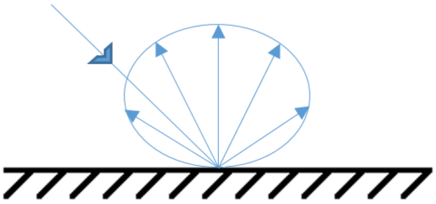

Figure 3.1: Diffuse reflection (Sentman)

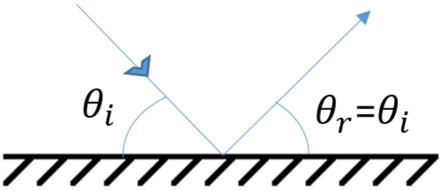

Figure 3.2: Specular reflection (Schamberg)

On the other hand, Schamberg assumed hyper-thermal flow, which implies that the effect of random motion of the molecules can be completely neglected [25]. Schamberg’s model corrects the thermal motion by a Joule gas approximation. The interaction with the surface is described by the relation of incident and reflected angle (According to Fig. 3.2 these angles are equal), the speed of the reflected molecules, and the angular width of the reflected beam [6]. As a consequence, the reflection can be modelled as specular (Fig. 3.2). This is a fundamental difference with Sentman’s model.

In terms of numerical values for C_D, Schamberg estimated the drag coefficient equal to 2.5 to 3.0 for any satellite, but admitted that it is a rough estimation due to the lack of experimental data. Sentman did not give a concrete value for estimating the drag coefficient, but emphasized how much C_D may vary with the flow angle or with the shape of the satellite. A few years later, in 1965, [26] considered 2.2 to be an acceptable estimation of the drag coefficient of a so called “compact satellite”[3]. Cook’s method is based on Schamberg’s model (it also assumes hyper-thermal flow), but makes use of the "thermal accommodation coefficient" α (as defined by Schaaf & Chambre [27]) for computing the drag coefficient.

In 1987, it has been shown that satellites orbiting at 225 km on a circular orbit mostly experience diffuse reflections with gas-molecules (97% diffuse and 2-3% quasi-specular) [28]. Even if that gave favour to Sentman’s method, both methods (Cook and Sentman) where still used. In order to decide which of those methods should be used, K. Moe and E. K. Sutton tried to compare them. In 1998, Moe & al. [29] computed C_D with both methods at different altitudes. They did not give favour to one method, but emphasized the importance of having more measurements to remove the uncertainty rising with altitude. In 2009 Sutton performed precise computations using both methods and concluded “further tuning of Sentman’s formulas can yield an increased accuracy, (...)” [30]. Then according to E. K. Sutton, Sentman’s model seems to give the most accurate lift and drag coefficient. However, it is using a theoretical value of the temperature ratio of the re-emitted to the incident particle (T_r/T_i), the definition of which is controversial. As the re-emitted temperature of the particle is unknown, this ratio is often substituted by a term depending on the surface temperature T_w, the incident temperature T_i and an accommodation coefficient α. While T_w is assumed equal to 300 K [31], the temperature of the incoming particle was assumed to be equal to the atmospheric temperature (i.e $T_i = T_a$) in some recent publications, such as [32] and [33]. But in 2008, G. Koppenwallner showed that $T_i = T_a$ is a

---

[1] Recent equations means equations published after Moe & al. [24] in 2004, because after 2004 Sentman’s method is re-interpreted and often used.

[2] The consistency of this assumption is verified when computing the Knudsen number of a LEO [6]

[3] When the ratio of the satellite maximum to minimum diameter is less than 1.5, and the satellite does not have large external structure like solar panels [12].

misinterpretation of Sentman's method [34]. According to him, the *kinetic temperature*[4] should be used for T_i (see subsection 3.2.3). On the other hand, the thermal accommodation coefficient α also appears to be problematic. It characterizes the collision between the gas-molecule and the satellite surface, which depends in a complex way on the spacecraft surface material, the chemical constituents of the thermosphere, the molecular weight, and the temperature of the incoming particle. The problem is that each of these parameters may vary with altitude, solar activity [36] and, of course, with atmospheric model [37].

Sentman's model assumes convex satellite surface and no interaction between the particles. However, nowadays Ray Tracing Panel (RTP) methods are able to account for multiple collisions of the particle with the satellite, [13] such as the Test Particle Monte Carlo (TMPC) [23], and momentum exchange between the particles, such as the Direct Simulation Monte Carlo (DSMC). Powerful software like the Rarified Aerodynamics Modeling System for Earth Satellites (RAMSES) [38] and Analysis of Non-Gravitational Accelerations due to Radiation and Aerodynamics (ANGARA) [39] are based on the DSMC (it requires large computational load). However, the precision gained in using RTP method is too small for POD improvement (see Chapter 6 where accelerations based on RTP are compared with accelerations computed with conventional methods).

3.2.2. LIFT AND DRAG COEFFICIENTS MODELLING

The drag coefficient C_D can be assumed constant for the entire spacecraft. In this case it is usually estimated as a free parameter in orbit determination programs. However, in this assignment, both the lift and drag coefficients will be modelled with a special procedure that allows to compute the the lift coefficient C_L [40].

One of the methods to model the drag and lift coefficients of a complicated shape is to represent the shape as a set of flat panels and to treat each panel independently. Compared to Finite Element Method (FEM), this method has the advantage of lower computational load and simplicity (see Sec. 5.2). For even more simplicity the panels are considered independently, which the possible shadowing of one panel over others. This effect is called self-shadowing, but is assumed negligible since the shapes of Swarm and GRACE are not expected to produce large self-shadowing. A more in-depth discussion about the different satellite modelling methods is given in Sec. 5.2.

In a representation of a satellite by a collection of independent flat panels each panel contributes to the drag and lift force according to Eq. 3.1, one can write

$$\vec{F}_{D,L} = \sum_{i=1}^{n} \frac{1}{2} \rho \vec{v}^2 A_{ref} C_{D_i,L_i} \vec{e}_{D_i,L_i} \,. \tag{3.3}$$

Note that A_{ref} is neither related to the orientation nor to the dimensions of the single panel because it is an agreed value for the entire vehicle [10] (usually the cross-sectional area in the direction of the satellite velocity vector). One can now focus on the computation of the lift and drag coefficients of individual panels, $C_{L,i}$ and $C_{D,i}$, based on Sentman's method as suggested by the literature review.

Sentman computed the force dF exerted by a flow of gas on an element of area dA, assuming free molecule flow and diffuse reflection. All steps taken by Sentman are well detailed in his publication [1], therefore the general equation that establishes the basis to compute the drag and lift coefficients is directly given in Eq. 3.6. The main steps leading from this equation to the recent equations in, e.g., E. Doornbos' PhD thesis [10], are summarized here (because they have never been detailed in literature).

The gas flow is characterized by its mass velocity vector $\vec{q} = -\vec{v}$ (the bulk velocity of the gas relative to the surface). The velocities of the molecules and atoms due to the random thermal motion are assumed to obey a Maxwell distribution. If the temperature of the gas is T the most probable thermal velocity of the particles is given by [41]

$$c_{mp} = \sqrt{\frac{2kT}{m_p}} \,, \tag{3.4}$$

where m_p is the mean molecular mass of the atmospheric composition and k the Boltzmann constant. The quantity

$$s = \frac{\|\vec{q}\|}{c_{mp}} \tag{3.5}$$

---

[4] The kinetic theory states that the temperature (or kinetic temperature) of a perfect gas is proportional to the average molecular kinetic energy [35].

is called the speed ratio and determines the relative importance of the bulk velocity and the random thermal motion of the gas particles.

For the computation of the force a local coordinate system x, y, z on the element of area dA is chosen such that the positive y axis is pointing along the inward directed normal vector of the surface, while x and z are tangential to the surface (see Fig. 3.3). Denoting by ϵ, γ, and η the direction cosines between $\vec{q}$ and the local coordinate axes x, y, z and by k, l, and t the direction cosines between the direction in which the force is desired and the local coordinate axes x, y, z, the force coefficient is given by [1]

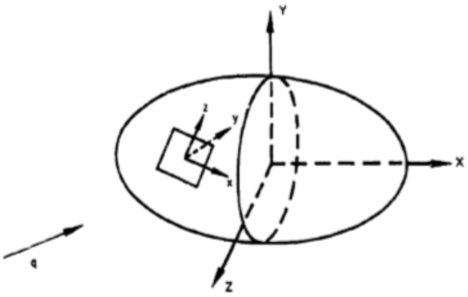

Figure 3.3: Axis systems used by Sentman [1] (Courtesy : L. H. Sentman)

$$\begin{aligned} dC &\equiv \frac{dF}{\frac{1}{2}\rho\vec{v}^2 A_{ref}} \\ &= \frac{dA}{A_{ref}}\left\{(\epsilon k+\gamma l+\eta t)\left[\gamma(1+erf(\gamma s))+\frac{1}{s\sqrt{\pi}}e^{-\gamma^2 s^2}\right]\right. \\ &\left.+\frac{l}{2s^2}(1+erf(\gamma s))+\frac{l}{2}\sqrt{\frac{T_r}{T_i}}\left[\frac{\gamma\sqrt{\pi}}{s}(1+erf(\gamma s))+\frac{1}{s^2}e^{-\gamma^2 s^2}\right]\right\}. \end{aligned} \tag{3.6}$$

Here, T_i and T_r denote the temperatures of the incoming and the re-emitted particles and

$$erf(x) \equiv \frac{2}{\sqrt{\pi}}\int_0^x e^{-t^2}dt \tag{3.7}$$

is the error function. Assuming a one-sided flat plate, the integration over the whole surface is trivial,

$$C = \frac{A}{A_{ref}}\left\{(\epsilon k+\gamma l+\eta t)\left[\gamma Z+\frac{P}{\sqrt{\pi}}\right]+lGZ+\frac{l}{2s}\sqrt{\frac{T_r}{T_i}}\left[\gamma\sqrt{\pi}Z+P\right]\right\}, \tag{3.8}$$

where A is the surface of the plate and where the following quantities have been introduced:

$$G=\frac{1}{2s^2}, \quad P=\frac{1}{s}e^{-\gamma^2 s^2}, \quad Z=1+erf(\gamma s). \tag{3.9}$$

Using Eqs. 3.4 and 3.5 one can write [42]

$$\frac{1}{s}\sqrt{\frac{T_r}{T_i}}=\frac{V_r}{V_i}, \tag{3.10}$$

where $V_i = \|\vec{q}\|$ and V_r is the most probable thermal velocity of the re-emitted particles. Denoting by $\vec{e}_q$ the velocity unit vector and by $\vec{e}_F$ the unit vector pointing into the direction in which the force is desired, one can write

$$k\epsilon+l\gamma+t\eta=\vec{e}_q\cdot\vec{e}_F=\begin{cases}1, & \text{for drag}\\ 0, & \text{for lift}\end{cases}, \tag{3.11}$$

since, by definition, the drag force points into the same direction as $\vec{q}$ and the lift force is perpendicular to $\vec{q}$. For drag $l=\gamma$ and thus the drag and lift coefficients for a one-sided flat plate are given by

$$\begin{cases} C_D &= \frac{A}{A_{ref}}\left\{\gamma Z(1+G)+\frac{P}{\sqrt{\pi}}+\frac{\gamma}{2}\frac{V_r}{V_i}(\gamma\sqrt{\pi}Z+P)\right\}, \\ C_L &= \frac{A}{A_{ref}}\left\{lGZ+\frac{l}{2}\frac{V_r}{V_i}(\gamma\sqrt{\pi}Z+P)\right\}. \end{cases} \tag{3.12}$$

If $\vec{n}$ is the outward pointing normal vector on the surface one has

$$\gamma = -\vec{e}_q \cdot \vec{n} \quad \text{and} \quad l = -\vec{e}_L \cdot \vec{n}, \tag{3.13}$$

where

$$\vec{e}_L = -\frac{(\vec{e}_q \times \vec{n}) \times \vec{e}_q}{|(\vec{e}_q \times \vec{n}) \times \vec{e}_q|} \tag{3.14}$$

is the unit vector pointing into the direction of the lift force. Note that with this method, the value of A_{ref} is not relevant for computing the total acceleration because when C_L or C_D are substituted back into Eq. 3.3, A_{ref} is cancelled.

3.2.3. ACCOMMODATION COEFFICIENT α

The velocity ratio V_r/V_i in Eqs. 3.12 can be related to the accommodation coefficient. Initially introduced by Knudsen in 1911 [43] to express the "exchange of temperature of a gas particle hitting a surface", the accommodation coefficient definition has been extended to "exchange of thermal energy transfer" by Cook [26] and finally to "exchange of thermal energy flux" by Koppenwallner [42]. As α forms the basis for defining the velocity ratio V_r/V_i, those changes have influenced the velocity ratio over the last decades. Cook's velocity ratio, e.g., is given by Eq. 3.15, Moe's by Eq. 3.16 [24] and Koppenwallner's definition by Eq. 3.17. In the end, Koppenwallner gave a detailed study in which he demonstrates that the exact velocity ratio to use is Eq. 3.17, leading to more accurate results. Thus Eq. 3.17 will be used for the implementation in the *Bernese GNSS Software*.

$$\frac{V_r}{V_i} = \sqrt{1+\alpha\left(\frac{T_w}{T_i}-1\right)}\Big\} \tag{3.15}$$

$$\frac{V_r}{V_i} = \sqrt{\frac{2}{3}\left[1+\alpha\left(\frac{2RT_w}{(2/3)\,{V_i}^2}-1\right)\right]}\Big\} \tag{3.16}$$

$$\frac{V_r}{V_i} = \sqrt{\frac{1}{2}\left[1+\alpha\left(\frac{2RT_w}{(1/2)\,{V_i}^2}-1\right)\right]}\Big\} \tag{3.17}$$

T_w	satellite panel temperature
R	universal gas constant 8.3144598 $Jmol^{-1}K^{-1}$

The determination of the theoretical value of α is often based on the hard sphere theory[5] like in [26, 44],

$$\alpha = \frac{f\mu}{(1+\mu)^2}, \tag{3.18}$$

$$\mu = \frac{m_p}{m_s}. \tag{3.19}$$

m_p	average molecular mass of the atmospheric composition
m_s	mass of the surface atoms/molecules
f	interaction factor (between 2 and 4)

The factor f is usually set to 3.6 when the GSI is assumed diffuse [32] (one should remember that Sentman's model assumes diffuse GSI). Further investigations show that α is varying with altitude [33] and solar activity [36]. The altitude correction is indirectly accounted for via the atmospheric model outputs m_p and

---

[5] Molecules and atoms are assumed to be impenetrable hard sphere.

n_0. In order to take the solar activity into account, [45] makes use of the Langmuir adsorption isotherm[6] to define α:

$$\alpha = \frac{KP}{1+KP}, \tag{3.20}$$

$$P = n_0 T_a. \tag{3.21}$$

K	constant
n_0	number of oxygen atoms per cubic meter
T_a	atmospheric temperature

The atmospheric temperature is again indirectly accounting for the solar activity via the atmospheric model. The value of the constant K depends on the source. While [47] uses $K = 5.0 \times 10^{-17}$ [10], [45] calculated that $K = 7.5 \times 10^{-17}$ gives the best Langmuir isotherm fit *for spherical objects*[7] [45]. A more recent publication of Pilinski [48] defines the Semi-Empirical Satellite Accommodation Model for Spherical and Randomly Tumbling Objects (SESAM), a method for computing α which unites both the hard sphere theory and the method using the Langmuir parameter. However, due to problems in the implementation and since SESAM is designed for randomly tumbling objects, this method will not be further investigated in this project.

To summarize, the correct definition of the accommodation coefficient is still controversial. Therefore both methods (Goodman's with Eq. 3.18 and Pilinski's with 3.20) with various coefficient will be tested, in order to find which model shall be used.

3.3. ATMOSPHERIC MODELS

Atmospheric models have a key role in the aerodynamic forces modelling. Indeed, the density (ρ) in Eq. 3.1, the mean molecular mass (m_p) used in Eq. 3.19 and the partial oxygen atom density (n_0) in Eq. 3.21 are solely given by atmospheric models. The methods to build the different atmospheric models are not in the scope of this assignment. The evolution of the different models is detailed in [22]. The two following atmospheric models are used for this assignment: NRLMSISE-00[8] and DTM2013. According to [10], NRLMSISE-00 should be used when the densities of individual atomic or molecular species are required, but that was before DTM2013 was released. DTM2013 seems to be a better model since it has been built with very accurate data from recent satellites such as CHAMP, GRACE or GOCE. Furthermore, the JB2008 model has been used to build DTM2013 [50]. Because the literature cannot give favour to one of those models, both will be tested for validation, which is an important assessment to do in order to find the best model for computing the aerodynamic forces.

The two models require a few solar and geomagnetic indices. The NRLMSISE-00 atmospheric model needs the daily F10.7 flux, the 81 day average of F10.7 and the geomagnetic ap indices. On the other hand DTM2013 also needs the daily F10.7 flux and the 81 day average of F10.7, but uses the geomagnetic Kp indices. Figs. 3.4 and 3.5 illustrate the densities computed by NRLMSISE-00 and DTM2013. Both models show a clear sensitivity to the sunlight (denser atmosphere near zero longitude). In general, the DTM2013 seems to estimate a lower density. Even if the estimated density differences between the two models seem small, they are expected to have visible impact on LEO POD.

Since the impacts of the atmospheric models output are large, they are considered as the primary source of error (especially the density) in the computation of the aerodynamic forces. For this reason, an elaborated method has been developed to correct density models such as the High Accuracy Satellite Drag Model (HASDM) or the Near Real-Time Density Model (NRTDM). For example, HASDM is estimating a scaling factor to determine the "true" density from the trajectories of inactive satellites and orbiting debris. Even if using those corrections has shown improvements ([51] and [47] respectively) they will not be implemented in the frame of this project.

---

[6] The definition from [46]: "The Langmuir adsorbtion isotherm describes the fraction of monolayers surface adsorption by a particular species as a function of the partial pressure of that species at a certain surface temperature".

[7] Validation with simplified spherical satellite is not presented in this document. Therefore the two different coefficients $K = 5.0 \times 10^{-17}$ and $K = 7.5 \times 10^{-17}$ will be tested, in order to not be restricted to the spherical assumption. In addition this will show if $K = 7.5 \times 10^{-17}$ is also suitable for panels.

[8] It is the most up to date and accurate model of the NRLMSIS series [49]

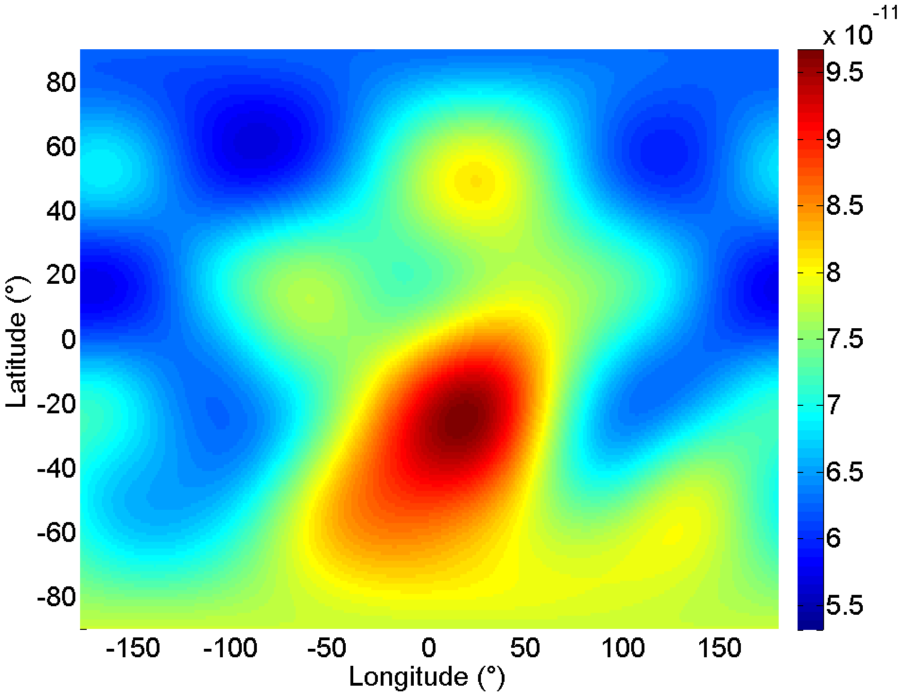

Figure 3.4: Densities computed by NRLMSISE-00 at 250 km high, the 14.12.2011 at noon UT. The unit is kg/m^3.

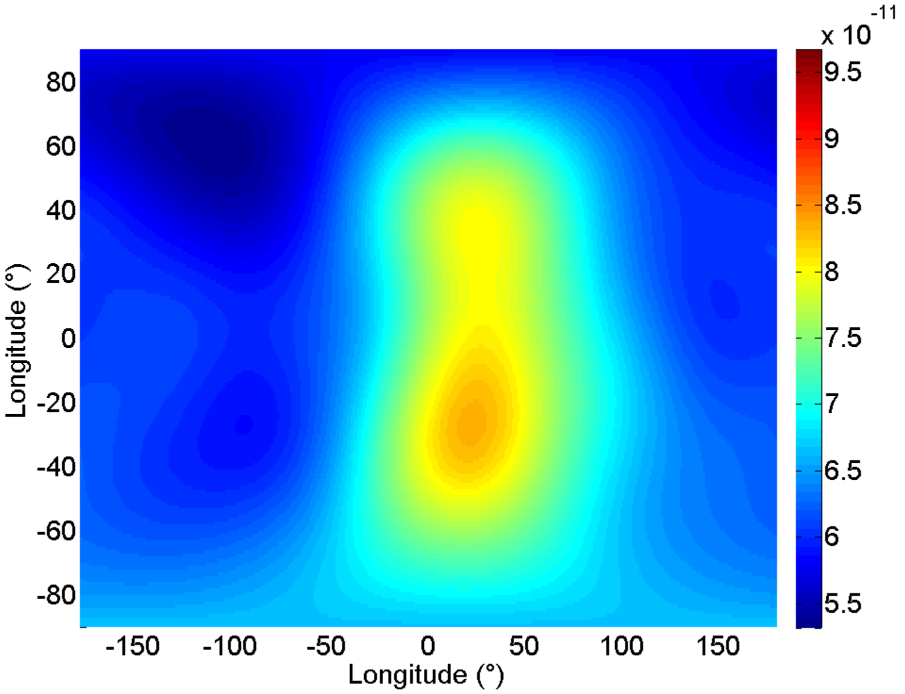

Figure 3.5: Densities computed by DTM2013 at 250 km high, the 14.12.2011 at noon UT. The unit is kg/m^3.

4

RADIATION PRESSURE FORCES

In this Chapter, the nature of the radiation pressure force is presented. Then the Solar radiation pressure, the emitted Earth radiation pressure and the reflected radiation pressure are discussed. For each force a modelling method is chosen for implementation.

4.1. GENERAL ASPECTS

Radiation pressure acting on a satellite is due to an interaction (reflection or absorption) of the satellite surface with electromagnetic radiations. The latter experiences a change in momentum and thus creates a pressure force on the satellite. Even if the force due to a single interaction is extremely small, large light flux (such as solar flux) may lead to a non-negligible acceleration [6]. Apart from the direct solar radiation pressure, the Earth albedo and infrared thermal radiation are the most important sources for radiation pressure.

The acceleration due to the radiation force is given by Eq. 4.1. The detailed steps to derive the light flux from the energy carried by a photon can be found in [16] or [6], thus will not be repeated in this document. The acceleration due to radiation pressure acting on paneled satellite is given by Eq. 4.1, either as function of the pressure P or as function of the light energy flux ϕ:

$$\ddot{\vec{r}} = \sum_{i=1}^{n} \vec{C}_{r,i} \frac{A_{ref}}{m} P = \sum_{i=1}^{n} \vec{C}_{r,i} \frac{A_{ref}}{m} \frac{\phi}{c} . \tag{4.1}$$

$\vec{C}_{r,i}$	vectorial radiation pressure coefficient of the panel
A_{ref}	reference area (agreed value for the entire satellite)
P	radiation pressure
ϕ	light energy flux
c	speed of light
n	number of panels
m	mass of the satellite

Similarly to the computation of the aerodynamic force, a special attention will be given to the $\vec{C}_{r,i}$, based on the photon-surface interaction.

4.2. PHOTON-SURFACE INTERACTION

The direction of the force depends on the nature of the interaction of the photon with the panel surface. One distinguishes between absorption, diffuse reflection and specular reflection. Fig. 4.1 shows the resulting radiation pressure forces directions depending on the kind of interaction, where $\hat{r}_{so,sa}$ (standing for Source-Satellite vector) is the unit vector of the photon's unit velocity direction.

The cosine γ of the panel's normal vector $\hat{n}$ with the photon's velocity vector $\hat{r}_{so,sa}$ is given by

$$\gamma = -\hat{r}_{so,sa} \cdot \hat{n} . \tag{4.2}$$

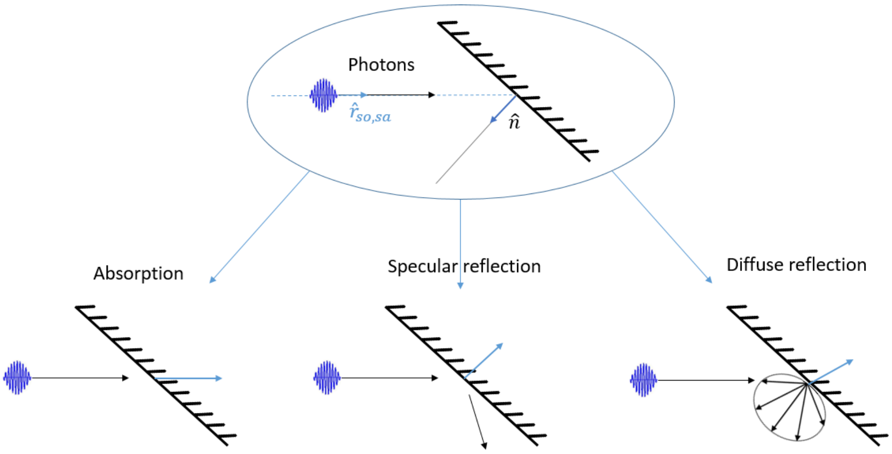

Figure 4.1: Basic types of photon-surface interaction. Black arrows indicate the trajectory of the photon, the blue ones indicate the direction of the resulting radiation pressure forces

The radiation coefficients of the three interactions will be presented as in [10]. Eq. 4.3 gives the resulting vector coefficient when photons are absorbed by the panel, where the area A_i is the actual area of the panel. Note that the product $A_i\gamma$ gives the projected area perpendicular to the photon's velocity vector.

$$\vec{C}_{a,i} = \begin{cases} 0 & \text{if } \gamma \leq 0 \\ \hat{r}_{so,sa}\dfrac{A_i\gamma}{A_{ref}} & \text{if } \gamma > 0 \end{cases} \tag{4.3}$$

The next formula (Eq. 4.4) gives the coefficient of a diffuse reflection, where the direction of the reflected radiation is independent of the direction of the incident one. The probability of the re-emission direction can be described by Lambert's cosine law [10].

$$\vec{C}_{d,i} = \begin{cases} 0 & \text{if } \gamma \leq 0 \\ (\hat{r}_{so,sa} - \dfrac{2}{3}\hat{n})\dfrac{A_i\gamma}{A_{ref}} & \text{if } \gamma > 0 \end{cases} \tag{4.4}$$

Finally, the coefficient of a specular reflection is given as follows:

$$\vec{C}_{s,i} = \begin{cases} 0 & \text{if } \gamma \leq 0 \\ -2\gamma\hat{n}\dfrac{A_i\gamma}{A_{ref}} & \text{if } \gamma > 0\,, \end{cases} \tag{4.5}$$

In general radiation pressure-induced accelerations are due to a mixture of those three interactions. So their respective probabilities must be introduced: p_d is the probability to have a diffuse reflection, p_s stands for a specular reflection and $(1 - p_s - p_d)$ for an absorption[1]. Then at least p_d and p_s of each panel have to be known, which are the so-called "optical properties" of the panel. Unlike the accommodation coefficient α discussed in Sec. 3.2.3, p_d and p_s can easily be measured on the ground. The vector of the radiation pressure coefficient may be written as follows:

$$\vec{C}_{r,i} = (1 - p_s - p_d)\vec{C}_a + p_s\vec{C}_s + p_d\vec{C}_s \tag{4.6}$$

It is then important to mention that optical properties of the panels (p_d and p_s) depend on the wavelength of the photons, thus the coefficients of the photon-surface interactions will be different when the emitted ERP or the reflected ERP and the SRP are computed.

4.3. DIRECT SOLAR RADIATION PRESSURE

The details of the algorithm to implement the SRP are given in this Section, including the distance and the penumbra correction. It is only the aspects relevant for the implementation of the force that will be detailed, for more in-depth information in those aspects the reader is referred to [10, 15, 52].

---

[1] This only true because one assumes to have no other interaction.

4.3.1. State of the art

SRP is the main non-conservative force acting on GNSS satellites and a lot of effort has been invested to model SRP for GNSS orbit determination [53, 54]. The main source of uncertainties in modelling the SRP comes from the optical properties of the modelled satellite. In this assignment, LEOs are modelled as a set of panels (i.e. macro-models), where each panel has its own optical properties: p_d and p_s.

The Sun emissivity is assumed constant[2] (see Chapter 2), but the Sun-Earth distance is varying. Therefore the reference radiation pressure force at one astronomical unit from the Sun must be corrected with the actual Sun-satellite distance. In addition, the penumbra corrections must also be accounted for. It is due to Sun's disc partially shadowed by the Earth when the satellite enters or leaves the Earth shadow. Taking this into account ensures a smoother and more accurate transition between eclipse and sunlight (See Fig. 4.2). Most scientific articles [55, 56] and books [6, 10, 57] agree on the algorithm to compute the SRP, but not on the penumbra correction modelling. Because accurately model the penumbra correction requires to account for the atmospheric refraction in addition to the shadowed Sun's disc. Only very complex algorithms are able to compute the atmospheric refraction. While [6] or [10] are simple methods, [52] and [12] are examples of complex ones which are accounting for the atmospheric refraction. For Swarm, the penumbra correction is only lasting two minutes per semi-orbit (see Sec. 6.2.1) when the satellite is going from sunlight to eclipse or *vice-versa*. In the scope of this assignment a simple penumbra correction will be implemented. The chosen method is used in the ANGARA software [39] and outlined in [10].

It is important to mention that the reflected photons are assumed to not strike other surfaces. Because the second interaction of the same photon with another satellite surface requires ray-tracing techniques [13], which are excluded in the scope of this assignment.

4.3.2. Mathematical model

With the chosen method we are dealing with the penumbra correction in a purely geometric way and that there is refraction which changes the picture but to take this into account is rather sophisticated. The position of the satellite, the Sun and the Earth need to be known. As a result, a satellite entering into eclipse is still in penumbra even though it should be geometrically in umbra (illustrated by Fig. 4.2) because this phenomenon extends the penumbra and squeezes the umbra.

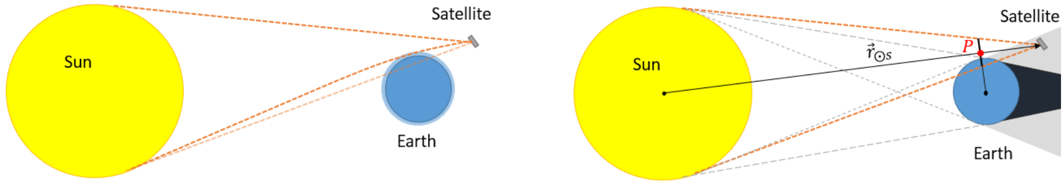

Figure 4.2: Illustrated eclipse transition geometry caused by the atmospheric refraction (on the left) and position of the point "P" used for computing the eclipse parameter

The chosen method to compute the penumbra correction is detailed in [10]. Only a few parameters have to be known for computing the so-called eclipse parameter η (Eq. 4.10): the position of the satellite, the position of the Sun, the Earth's mean radius and the Sun's mean radius. First the point "P" is positioned on the Sun-satellite vector, where it is perpendicular to the Earth mean radius surface (see Fig. 4.2 right). With the vectors

$$\vec{r}_{p,sa} = (\hat{r}_{\odot,sa} \cdot \vec{r}_{\oplus,sa})\hat{r}_{\odot,sa}\,, \tag{4.7}$$

and

$$\vec{r}_{\oplus,p} = \vec{r}_{\oplus,sa} - \vec{r}_{p,sa}\,, \tag{4.8}$$

one can compute the so-called eclipse parameter

$$\eta = \frac{\| \vec{r}_{\oplus,p} \| - R_{\oplus}}{\| \vec{r}_{p,sa} \| \, R_{\odot}} \| \vec{r}_{\odot,sa} \| \,. \tag{4.9}$$

Since the shadow function solely depends on η, it indicates whether the satellite is in eclipse, partial eclipse or full sunlight

---

[2] It has been determined based on the thermal emissivity of the Sun's surface temperature (assumed to be a perfect black body).

$$\begin{cases} \eta < -1 & full \quad eclipse \\ -1 \leq \eta \leq 1 & partial\, eclipse \\ \eta > 1 & full \quad sunlight. \end{cases} \tag{4.10}$$

$\vec{r}_{p,sa}$	P - satellite vector
$\vec{r}_{\oplus,p}$	Earth - P vector
$\vec{r}_{\odot,sa}$	Sun - satellite vector
$\vec{r}_{\oplus,sa}$	Earth - satellite vector
$R_{\odot}$	Sun mean radius 695700000 m
$R_{\oplus}$	Earth mean radius 6371000 m
η	eclipse parameter

This allows to compute the so-called geometric shadowing factor

$$f_g = 1 - \frac{1}{\pi} \arccos(\eta) + \frac{\eta}{\pi}\sqrt{1-\eta^2}. \tag{4.11}$$

Finally the shadow function f_s is given by

$$f_s = f_g f_a, \tag{4.12}$$

where the parameter f_a is the amount of sunlight that is not absorbed by the atmosphere. Precise determination of this factor can quickly lead to an extremely complicated computation [58]. Indeed photons of different wavelengths interact differently with the chemical composition and density of the atmosphere. Since accurately computing this factor is beyond the scope of this assignment, f_a will initially be set to 1 and its impact will be empirically investigated in Chapter 6.

The acceleration due to solar radiation pressure is given as follows:

$$\ddot{\vec{r}}_{SRP} = \sum_{i=1}^{n} \vec{C}_{r,i} \frac{A_{ref}}{m} \left(\frac{1AU}{\|\vec{r}_{\odot,sa}\|} \right)^2 f_s \quad P_{1AU}. \tag{4.13}$$

AU	astronomical unit 149597870700 m
P_{1AU}	radiation pressure at 1 AU from the Sun

In $\vec{C}_{r,i}$, the source-satellite vector $\vec{r}_{so,sa}$ is $\vec{r}_{\odot,s}$. Note that the distance correction with the astronomical unit has been accounted for.

4.4. EARTH RADIATION PRESSURE

Similarly to the SRP, the algorithms used to compute emitted ERP and reflected ERP are given in this Section. Since the Earth is modelled either as a sphere with uniform reflectivity and emissivity or as a map of local reflectivity and emissivity values, the ERP can be modelled analytically (see Appendix B) or numerically (detailed in this Section).

4.4.1. STATE OF THE ART

Earth radiation pressure (ERP) is separated into two categories, reflected[3] (short-wavelength) and emitted (long-wavelength) radiations. On one hand, the long-wavelength radiation is due to thermal infrared emission of the Earth, thus acting day and night. In terms of magnitude, it can be up to 17% of the SRP magnitude [6]. On the other hand, the reflected radiations are mostly in the visual spectrum range (like the direct radiation pressure). This force is larger and can be up to 35% of the SRP magnitude for LEOs [15], but is only acting while the satellite is illuminated by parts of the Earth exposed to sunlight.

For modelling the force due to ERP, both the satellite and the Earth have to be modelled. The LEOs are represented as a collection of independent flat panels. The Earth can be modelled differently regarding the algorithm used, either as a perfect sphere with a single mean emissivity and reflectivity coefficient, or as a grid of elements each containing local reflectivity and emissivity coefficients (see Sec. 5.3).

---

[3] Also called albedo ERP

The mathematical background to numerically compute ERP has not changed since the method described by Knocke [59] became a benchmark inside the geodetic community. Indeed its simplicity makes it easy to implement and its flexibility allows to use Earth maps of different precisions. The major assumption to make in order to use this model is that the Earth's surface (or atmosphere) is Lambertian[4]. The Earth maps are constructed from data of Earth observing satellite missions, like Earth Radiation Budget Experiment (ERBE) [60] or the ongoing Clouds Earth's Radiant Energy System (CERES) [61]. In this assignment, the CERES data are used to obtain the emissivity and reflectivity of the Top-Of-Atmosphere[5] (TOA) elements that are used to model the Earth (see Sec. 5.3 for more details).

4.4.2. NUMERICAL MODEL

The numerical method computes the force exerted by each TOA element on each panel of the satellite. The given equations are based on [15]. First of all, one has to consider whether the force is zero or if it has to be computed. To do so, three cosine angles have to be computed (see Fig. 4.3 and 4.1): φ checks if the TOA element is illuminated by sunlight (Eq. 4.14), β if the TOA element is visible from the satellite (Eq. 4.15) and finally γ if the panel is oriented toward the Earth (Eq. 4.2 where $\hat{r}_{so,sa}$ being $\hat{r}_{TOA,sa}$).

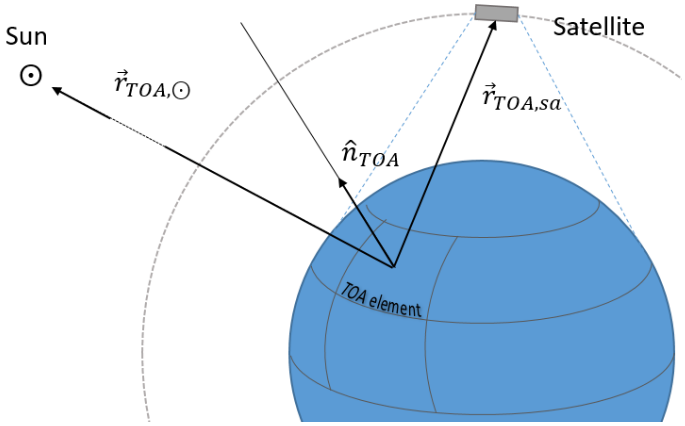

Figure 4.3: Illustration of the geometry Sun, satellite, and TOA element.

$$\varphi = \hat{r}_{TOA,\odot} \cdot \hat{n}_{TOA} \tag{4.14}$$

$$\beta = \hat{r}_{TOA,sa} \cdot \hat{n}_{TOA} \tag{4.15}$$

$\hat{r}_{TOA,\odot}$	normalized TOA - Sun vector
$\hat{r}_{TOA,sa}$	normalized TOA - satellite vector
$\hat{n}_{TOA}$	normal vector of the TOA element

With the distance correction of the solar pressure, the reflected ERP from TOA element j can be computed as follows [15],

$$P_{j,refl} = \begin{cases} 0 & \text{if } \varphi_j \leq 0 \text{ or } \beta_j \leq 0 \\ \left(\frac{1AU}{\|\vec{r}_{TOA_j,\odot}\|}\right)^2 P_{1AU} \frac{a_j}{\pi \|\vec{r}_{TOA_j,sa}\|^2} A_{TOA_j}\, \varphi_j\, \beta_j & \text{if } \varphi_j > 0 \text{ and } \beta_j > 0 \end{cases} \tag{4.16}$$

correspondingly, the emitted ERP from TOA element j is

$$P_{j,emit} = \begin{cases} 0 & \text{if } \beta_j \leq 0 \\ \left(\frac{1AU}{\|\vec{r}_{TOA_j,\odot}\|}\right)^2 P_{1AU} \frac{e_j}{4\pi \|\vec{r}_{TOA_j,sa}\|^2} A_{TOA_j}\, \beta_j & \text{if } \beta_j > 0. \end{cases} \tag{4.17}$$

---

[4] The surface has a solely diffuse reflection and emission

[5] This is the surface approximately 30 km above the Earth surface [62].

$\vec{r}_{TOA_j,\odot}$	Sun-TOA_j vector
$\hat{r}_{TOA_j,sa}$	normalized TOA_j - satellite vector
$\hat{n}_{TOA_j}$	normal vector of the TOA_j element
a_j	reflectivity (albedo) of the TOA_j element
e_j	emissivity of the TOA_j element
A_{TOA_j}	area of the TOA_j element (see Sec. 5.3.1)

Summing the influence of all N TOA elements upon all n panels, one obtains the total acceleration due to reflected ERP

$$\ddot{\vec{r}}_{refl} = \sum_{j=1}^{N} \sum_{i=1}^{n} \vec{C}_{r,i,j} \frac{A_{ref}}{m} P_{j,refl}, \tag{4.18}$$

and due to emitted ERP

$$\ddot{\vec{r}}_{emit} = \sum_{j=1}^{N} \sum_{i=1}^{n} \vec{C}_{r,i,j} \frac{A_{ref}}{m} P_{j,emit}. \tag{4.19}$$

In both Eq. 4.18 and Eq. 4.19, the source-satellite vector $\vec{r}_{so,sa}$ in $\vec{C}_{r,i,j}$, is $\vec{r}_{TOA_j,sa}$.

5

IMPLEMENTATION

This Chapter provides an overview the requirements to implement the four non-gravitational forces detailed in Chapters 3 and 4. First, the accuracy of the computed accelerations is discussed. Secondly, the implementation of the computed accelerations in the precise orbit determination of the *Bernese GNSS Software* is detailed. Thirdly, the chosen Earth and satellite modelling methods are explained. Finally, a few results are shown to demonstrate the consistency of the implemented forces with the theory.

5.1. IMPLEMENTATION OF NON-GRAVITATIONAL FORCES FOR LEO POD IN THE *Bernese GNSS Software*

An in-depth presentation of the methods of GPS-based LEO POD is not in the scope of this report. Details can be found, e.g., [5, 14].

Satellite orbit determination primarly requires observation data (related to the satellite position or velocity), furnished by a satellite tracking system. Laser tracking systems, such as Satellite Laser Ranging (SLR), measure the range between a ground station and a satellite[1] by means of ultra-short laser pulses. On the other hand, any radar tracking system measures the distance (or slant range) between transmitter and receiver[2], as well as the line-of-sight relative velocity (or range-rate) of the satellite. These pieces of information are extracted by measuring the electromagnetic wave propagation properties between the transmitter and the receiver [6].

The GPS-based microwave tracking positioning method became a benchmark for LEO orbit determination since its accuracy has been successfully tested upon the Topex/Poseidon satellite in 1992 [63]. GPS satellites generate 2 microwave carrier phase signals with distinct frequencies, $L_1 = 1575.42 MHz$ and $L_1 = 1227.60 MHz$, which are both carrying three binary codes, the Coarse-Acquisition code (C/A), Precise code (P) and the encrypted version of P (Y). The geometric distance can be computed to each single GPS satellite (${\rho_1}^{i,j,k,l}$ on Fig. 5.1). One needs at leat 4 GPS satellites to obtain the LEO position in 3-dimensional space and the receiver clock correction. The distances can be derived either from the code observation[3] or from the phase observation. The latter is two to three orders of magnitude more accurate than the code observation, thus preferred for precise orbit determination [5]. It is common practice to combine both techniques to eliminate specific error sources.

There are three main approaches to determine a LEO orbit from GPS data; the dynamic approach, the kinematic approach and the reduced-dynamic approach. The dynamic approach makes use of force models (gravitational and non-gravitational) to set up the equation of motion, of which the satellite trajectory is a particular solution. In practice it is carried out iteratively to obtain an optimal least-squares estimation of the satellite reduced-dynamic orbit. In return the equation of motion can be solved numerically at any time to provide the satellite position. On the other hand, a kinematic orbit is independent from *a priori* force models, thus according to D.-J. Peng "As a pure geometrical orbit determination method, [kinematic POD] (...) is particularly suitable for the LEOs perturbed strongly by the atmospheric drag" [63], but very sensitive to

---

[1] Must be equipped with nadir viewing retro-reflectors.

[2] May be on the ground or in space.

[3] In fact it is not a range but a "pseudo-range" that is derived from the code observation, because receiver and emitter clocks are not synchronized.

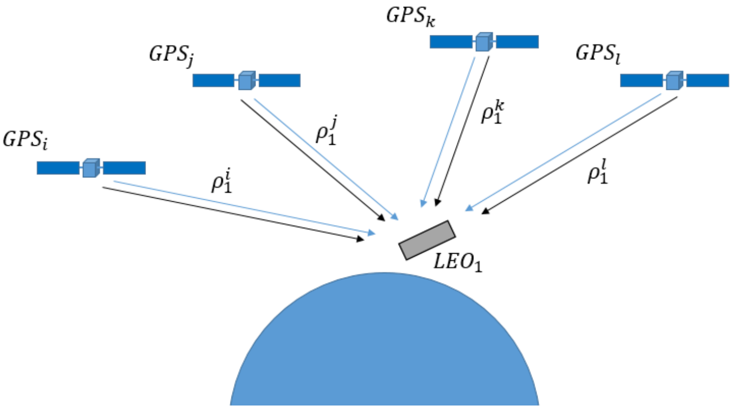

Figure 5.1: Geometric GPS-LEO distance derived by L_1 (blue arrows) and L_2 (black arrows) transmitted by the GPS satellites

measurement error. Finally, the reduced-dynamic method may be seen as a trade-off between the two approaches, especially suitable for optimum orbit modelling [64]. The reduced dynamic orbits solutions in this assignment are computed with the *Bernese GNSS Software*, by making use of Piecewise Constant accelerations (PCA) in the form of additional empirical parameters in the equation of motion[4], Eq. 5.1 [5].

The equation of motion can be written as:

$$\ddot{\vec{r}} = -GM\frac{\vec{r}}{r^3} + \vec{f}_1(t,\vec{r},\dot{\vec{r}},Q_1,...,Q_d,P_1,...,P_s) := \vec{f}\,, \tag{5.1}$$

a particular solution of this equation of motion can be specified by the initial conditions

$$\vec{r}(t_0) = \vec{r}(a,e,i,\Omega,\omega,u_0;t_0) \qquad \text{and} \qquad \dot{\vec{r}}(t_0) = \dot{\vec{r}}(a,e,i,\Omega,\omega,u_0;t_0)\,. \tag{5.2}$$

GM	gravity constant times the mass of the Earth
$\vec{r}$	geocentric position of the satellite
$\vec{f}_1$	perturbing acceleration acting on the satellite
$\vec{f}$	total acceleration
a,e,i,Ω,ω,u_0	6 orbital elements, respectively: semi-major axis, eccentricity, inclination right ascension of ascending node, argument of perigee and true anomaly
$Q_1,...,Q_d$	force model *parameters* (e.g. non-gravitational forces)
$P_1,...,P_s$	pseudo-stochastic empirical parameters

The pseudo-stochastic empirical parameters can be of different types: PCA, instantaneous velocity changes, piecewise linear accelerations, and so on. In this assignment only PCA are used, because they are most suitable to directly show the impact of the implemented non-conservative forces. The vector $\vec{f}_1$ will include the four non-gravitational forces to be implemented.

5.2. MODELLING THE SATELLITE

In this section the chosen method to model the satellite (i.e. the macro-models) will be explained. The three LEOs used in this assignment will be discussed, namely GRACE A, GRACE B and Swarm C (only).

5.2.1. GENERAL ASPECTS

The algorithms presented in previous Chapters 3 and 4, are suited for satellites represented by a number of flat panels. Before the 70's, satellites were modelled as simple geometries such as cones, cylinders or spheres (Fig. 5.2 a). Except for the cannonball satellites such as LAGEOS in Fig.2.2, simple geometries are rough approximations. More elaborated *a priori* models called "ROCK" (based on [65, 66]) where used for GPS satellites because of their characteristic shape (see Fig. 2.3). However, such simplified geometries (of the *a priori* models) cannot precisely model a satellite [67]. Later, spacecrafts of characteristic shape are represented as

---

[4] Without those additional pseudo-stochastic empirical parameters, the equation of motion is the same as for the dynamic approach.

an assembly of simple geometries, the "shape element composition method" [23] (e.g. missiles can be represented as a cylinder and a semi-sphere, Fig. 5.2 b). The most famous for GNSS satellite is the "Box-wing model", so-called because they have two large symmetrical solar panels with a central "box" in the middle (Fig. 5.2 c). Even though box-wing models are still used today for GNSS, they are hardly applicable to all the LEOs because their shapes are very diversified[5]. A more generic method called "panel methods" decomposes the spacecraft into flat panels (often referred to as macro-model) [23] (see Fig. 5.2 d). This method has been requested for this assignment because it can be applied to every single satellite (as far as the data are available). Moreover, the equations used to compute the surface forces are the same, regardless the number of panels contained in the macro-model.

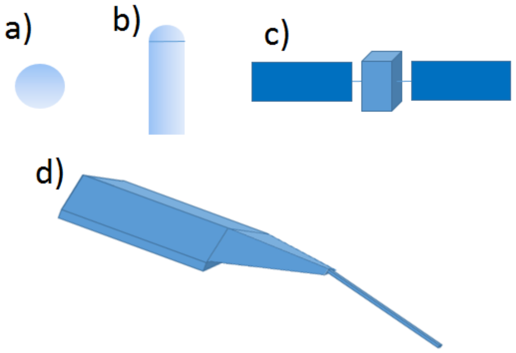

Figure 5.2: Modelling a satellite. a) simple geometry, b) shape element composition method, c) Box-wing model, d) macro-models Swarm satellite

The panel properties may be separated into two categories: the properties used by each non-gravitational model and the ones proper to one type of force. The first category contains the area A_i and the normal vector $\hat{n}_i$ of the panel. The second category contains coefficients specific to an interaction between the satellite surface and a photon (see Sec. 4.2), or the satellite surface and a particle (see Sec. 3.2.1). When the panel is interacting with photons, such as for SRP and ERP, they can be absorbed, diffusely reflected or specularly reflected. The probabilities of the respective interactions to occur are given by a "probability coefficient", respectively p_a, p_d and p_s (see Sec. 4.2). As no other interaction is assumed to take place, $p_a + p_d + p_s = 1$ must hold and if two coefficients are known, the remaining one can be deduced. An important point is that, in general, the probability coefficients are different for the visible and the IR part of the spectrum. Therefore, a minimum of 4 coefficients should be known per panel for computing SRP and ERP, e.g., $p_{s,IR}$ and $p_{d,IR}$ for IR photons, and $p_{s,VI}$ and $p_{s,VI}$ for the visual spectrum photons.

On the other hand, the accommodation coefficient used for computing GSI is not specific to the panel, but is the same for all the panels (due to lack of knowledge about GSI occurring at LEO altitude, see Sec 3.2.1). However, there is a panel property that is required for computing the aerodynamic force: the surface temperature (see Eq. 3.17). Since the thermal re-radiation force will not be implemented (see Chapter 2), the panel temperature is assumed constant at 300 K (rounded from 298 K in [31]).

One cannot discuss precise material properties without mentioning *ageing effects*. Indeed, satellite exposure to atmospheric gas, high-energy photons (like UV) and micrometeorites in space environment lead to inevitable ageing of the material. This effect permanently changes the surface optical properties (especially the specular coefficients) [65] and surface ageing may lead to a manifestation of orbit modelling errors [16]. Material ageing may be modelled, but requires laboratory simulations of the various spacecraft components [68]. Anyhow, such data are difficult to obtain from satellite manufacturers, therefore material properties are in general[6] assumed to be constant. Therefore no material ageing will be implemented.

5.2.2. GRACE A & B

Launched in 2002, the currently operating Gravity Recovery And Climate Experiment (GRACE) is a partnership mission between NASA and Deutsches Zentrum für Luft- und Raumfahrt (DLR). The mission aims to accurately map the variations in Earth's gravity field [69]. This is carried out by two similar satellites (see

---

[5] Except the Jason satellites, LEOs do not share a characteristic shape of GNSS satellite.

[6] Rarely mentioned in the literature of non-gravitational force modelling.

Fig. 5.3) in nearly identical orbits with separations controlled to stay within 170 and 270 km. The reason for controlling the separation is that both satellites possess a horn antenna for the transmission and reception of the $K/Ka-$Band Ranging (KBR) signal which has a μm precision [70]. This important feature provides a very precise external validation instrument for assessing the (relative) precision of the orbit solutions (see Sec. 7.5). The GRACE satellites have circular and near polar orbits with an initial height of 500 km. It is also important to mention that their orbits are not Sun-synchronous, thus the angle between the satellite orbital plane and the Sun (i.e. β_0 angle, see also Fig. 5.12) is continuously varying. This is important factor when testing non-gravitational forces.

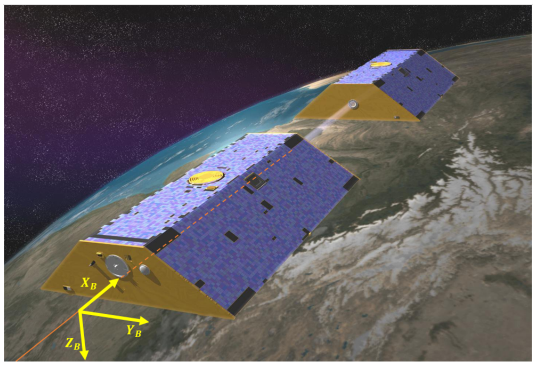

Figure 5.3: GRACE A & B (courtesy: Astrium GmbH). The satellite body-fixed coordinate system is shown in yellow.

GRACE A and B are also equipped with the Super-STAR instrument [71]. It is an ultra-sensitive space accelerometer[7] with a precision of $10^{-10}m/s^2$ in the radial and along-track direction, and $10^{-9}m/s^2$ in the cross-track direction. Such a high precision allows to validate the modelled non-gravitational accelerations (after calibration of the accelerometer data, see Sec. 7.2).

The surface of GRACE A & B have been modelled using 8 panels. The panel properties are detailed in Appendix C.

5.2.3. SWARM

Figure 5.4: Swarm (courtesy: ESA). The satellite body-fixed coordinate system is shown in yellow.

Since 2013 the constellation of three satellites Swarm-A, -B, and -C is measuring the Earth's magnetic field (part of the ESA's Earth explorer missions) [72]. While Swarm A and C are flying on similar orbits with an initial altitude of 450 km, Swarm B has a higher initial orbit of 530 km. The three satellites have circular and near polar orbits which are not Sun-synchronous. Unlike GRACE satellites, they are not equipped for a $K/Ka-$band measurement. They have on board an electrostatic high-sensitive microaccelerometer [73], unfortunately as stated by C. Siemens "(...) the acceleration measurements suffer from a variety of disturbances, the most prominent being slow temperature-induced bias variations and sudden bias changes" [74], but since the disturbances were detected, large efforts have been undertaken to correct the data. Since the corrected data is not available in this assignment, Swarm's accelerometer data is not part of the validation process.

---

[7] It measures both linear and rotational accelerations, the latter is not used for this assignment.

Due to lack of data regarding the optical properties of the Swarm macro-models, they have all been *assumed* based on the data provided by [2]. The detailed composition of the panels is known to us, but not the optical properties it encompasses. The assumptions made, as well as the optical properties used are detailed in Appendix C.

The assumed values for the optical properties are indeed very rough approximations; nevertheless it is not possible to be more accurate without the exact data given by the manufacturer. The influence of the optical properties are investigated in Chapter 6 and Appendix H. The detailed properties used for the Swarm macro-models is given in Appendix C.

5.3. MODELLING THE EARTH

In this section the chosen method to model the Earth's TOA is presented. Moreover, the horizontal wind model HWM14 is introduced. It is included in modelling the aerodynamic forces and tested in Chapters 7 and 8.

5.3.1. TOP-OF-ATMOSPHERE SURFACE ELEMENT

The first obvious approximation of the Earth surface modelling is to consider it as a perfect sphere (see Fig. 5.5 a) and with uniform reflectivity (albedo) of 0.3 [75]. A similar modelling of the Moon has been applied to compute the Moon radiation pressure (see Appendix B). In order to account for *local* surface properties, the reflectivity has to be known, e.g. on a grid over the Earth (see Fig. 5.5 b). The local optical properties are derived by Earth observing satellites missions, like ERBE form the mid-eighties or the current CERES missions. Such space observations measure the Top-Of-Atmosphere (TOA) radiative fluxes. TOA optical properties are less sensitive to model variations when compared with Earth surface properties, because the cloud covering is accounted for [76] and their is no atmospheric absorption to consider. Both missions provided gridded monthly mean values of reflectivity and emissivity. In addition to being more recent, B. A. Wielicki claims that "The improved angular and temporal sampling of the CERES experiment will improve the accuracy of the data relative to ERBE by a factor of 2 to 3, depending on the time and space scales of interest." [61], therefore CERES data are chosen for this assignment. In more details about the CERES data used, the Earth is modelled as a 2.5°x 2.5°grid of the monthly mean emissivity and reflectivity coefficients of the year 2007. Since most of the orbital tests and validations are carried out during the Month of August, Fig. 5.6 and 5.7 show the CERES data for that month.

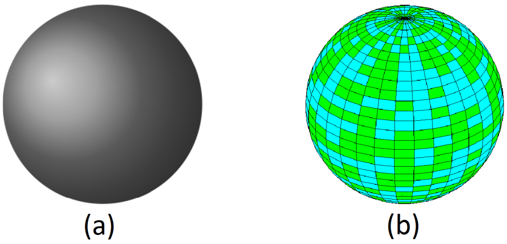

Figure 5.5: Earth modelling, uniform sphere model with a uniform optical properties (a), local properties on a grid (b)

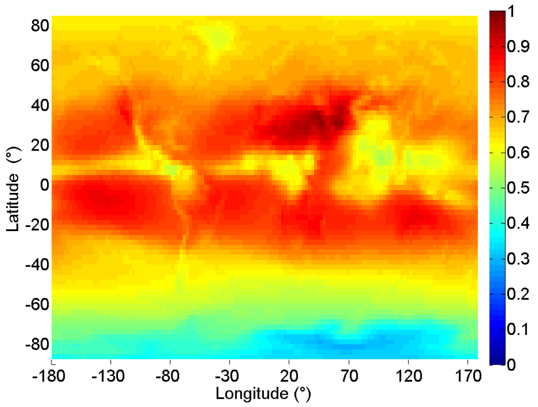

Figure 5.6: CERES emissivity map of August

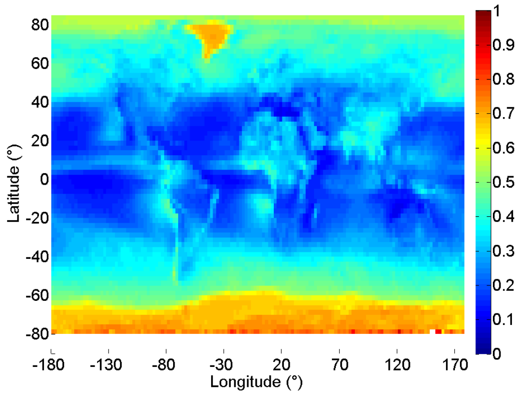

Figure 5.7: CERES reflectivity map of August

The required properties of each TOA element to compute the ERP are indicated by Eqs. 4.19 and 4.18, namely the area, emissivity and reflectivity. Note that data are missing near the poles. Since the optical properties seem correlated with the latitude, the data of the adjacent latitude is used when missing. At the pole, a cap of 2.5° radius is modelled with the optical properties of the previous latitude at the Greenwich meridian. While the optical properties of each TOA surface element are given by CERES, their area ($A_{j,TOA}$) must be computed based on the grid resolution of 2.5°(Eq. 5.4). Computing the area necessitates to know the altitude of the TOA element, which varies with the latitude (Eq. 5.3) because the Earth TOA is assumed ellipsoidal [62].

$$R_{TOA_j} = \frac{ab}{\sqrt{a^2 \sin^2(\theta_j) + b^2 \cos^2(\theta_j)}} \tag{5.3}$$

$$A_{TOA_j} = R^2_{TOA_j} \cos(\theta_j) \quad \delta^2 \tag{5.4}$$

a	semi-major axis of TOA surface ellipsoid, 6’408’1370 m [62]
b	semi-minor axis of TOA surface ellipsoid, 6’386’6517 m [62]
θ_j	geocentric latitude
δ	grid resolution in radians
R_{TOA_j}	geocentric distance of the j^{th} TOA surface element
A_{TOA_j}	area of the j^{th} TOA surface element

Note that the semi-major and semi-minor axes of the TOA surface ellipsoid are indeed some 30 km larger than the Earth’s mean radius surface ellipsoid axes.

5.3.2. WIND

The relative velocity of the satellite with respect to the atmosphere is reasonably estimated with Eq. 5.5, assuming that the atmosphere co-rotates with the Earth [6].

$$\vec{V}_r = \vec{V} - \vec{\omega}_{\oplus} \times \vec{r} \tag{5.5}$$

The velocity of the atmosphere is even more accurate in introducing a horizontal wind correction, given by horizontal wind models such as the HWM14 (which will be used in this assignment). It is an updated version of the most novel "Horizontal Wind Model" series [77], which computes the meridional and zonal directions of the horizontal wind [78]. The wind computed by HWM14 is then subtracted from $\vec{V}_r$ to obtain the corrected satellite velocity w.r.t. the atmosphere

$$\vec{V}_{r,HWM} = \vec{V}_r - \vec{V}_{HWM}. \tag{5.6}$$

$\vec{\omega}_\oplus$	Earth angular velocity $(0,0,7.292115146710^{-5})$ rad/s
$\vec{r}$	satellite position vector
$\vec{V}$	satellite velocity vector
$\vec{V}_r$	satellite velocity with reference to the co-rotating atmosphere
$\vec{V}_{HWM}$	velocity vector of the wind w.r.t. co-rotating atmosphere
$\vec{V}_{r,HWM}$	corrected satellite velocity w.r.t. the atmosphere

The impact of horizontal wind model is small. For instance at the GRACE position the first of August 2014, $\|\vec{V}_r\| = 7659\ m/s$ and $\|\vec{V}_{HWM}\| = 89\ m/s$.

5.4. REFERENCE FRAMES

In order to compute the non-gravitational forces, various reference frames have to be used to account for the different frames of the required information, such as the satellite position, the wind velocity direction, the panel orientation, or the satellite attitude. The reference frames and transformations required for computing the non-gravitational forces will be shortly discussed. The transformations are performed with Eq. 5.7 and the inverse transformation with the transpose matrix with Eq. 5.8. Note that rotation matrices are orthonormal. Therefore, the inverse matrix is equal the transpose matrix. For more details about the frames and transformation matrices, the reader is referred to [79].

$$\vec{X}^P = \boldsymbol{T_{PQ}}\vec{X}^Q \tag{5.7}$$

$$\vec{X}^Q = \boldsymbol{T^t_{PQ}}\vec{X}^P \tag{5.8}$$

P, Q	any reference frame
$\vec{X}^P$	vector $\vec{X}$ expressed in reference frame F_P
$\vec{X}^Q$	vector $\vec{X}$ expressed in reference frame F_Q
T_{PQ}	transformation matrix from F_Q to F_P
T^t_{PQ}	transformation matrix from F_P to F_Q

First of all, two Earth-centered reference frames are used: the Earth-Centered Inertial (ECI) frame F_I and the Earth-Centered, Earth-Fixed (ECEF) frame F_E. The X_I-axis of the F_I frame passes though the equator along the direction where the ecliptic and the equator cross: the Vernal Equinox. The Z_I-axis is directed to the north along the mean rotation axis of the Earth and the Y_I-axis completes the right-handed system. Since the Earth rotation axis shows a nutation and precession, F_I is not constant over time. So two coordinate system references for the ECI are used: J2000, which corresponds to the F_I defined at 12:00 Zulu Time on 1 January 2000 and the True System of Epoch (TOE) which is F_I at the epoch of interest. On the other hand, the F_E frame is very similar to the F_I frame with the difference that the X_E-axis of F_E crosses the Greenwich meridian (also through the equator). Z_E-axis is along the Earth spin axis and Y_E-axis also passes through the equator, perpendicular to the X_E-axis.

In addition, two reference frames are used with the origin located at the center of mass of the satellite: the Satellite Body-Fixed (SBF) frame F_B and the orbital frame (RSW) F_O. The axis directions of the latter are Radial (R), Along-track (S) and Cross-track (W). The radial axis is the reference, it is derived by the Earth-Satellite vector. The Cross-track direction is then defined perpendicular to the satellite velocity vector and the radial direction. Finally, the Along-track axis is perpendicular to the Radial and Cross-track directions. Therefore the satellite velocity vector direction is only aligned with the Along-track for circular orbits (rr at the perigee and apogee of the orbit). Furthermore, the F_B frame is proper to the satellite (see Fig. 5.4 for Swarm and Fig. 5.3 for GRACE). The X_B-axis is usually pointing forward[8], the Z_B-axis is nadir pointing and the Y_B-axis is derived perpendicular to the other two axis. It is important to bear in mind that all the frames used are *right-handed.*

In the *Bernese GNSS Software* the orbit integration is conducted in F_I J2000 and hence the modelled accelerations must be introduced in the POD in F_I J2000. The SRP and the ERP (emitted and reflected) accelerations are modelled in F_I J2000. Since both the Sun and the satellite position are given in F_I J2000, then the shadowing function f_g (see Eq. 4.11), as well as the angles ϕ and β (see Eqs. 4.14 and 4.15, respectively) are directly computed. However, in order to compute the angle γ the normal vector of the satellite is required

---

[8] For GRACE A it is the opposite, because flying "backwards".

Vector used in the force modelling	**Reference frame**
Satellite panel normal	F_B
Earth wind velocity	F_E
Satellite and Sun positions	F_I
GRACE accelerometer data accelerations	F_O

Table 5.1: Example of vectors given in various reference frames

which is given in SBF, therefore frame transformations are necessary. First, each panel normal vector $\vec{n}$ is transformed into the True System of Epoch (TOE) in building the transformation matrix with the attitude of the satellite (given by the qaternions delivered by the star tracker cameras). Then, $\vec{n}$ is transformed into F_I J2000 and γ can be computed. When accelerations due to aerodynamic forces are computed, the use of atmospheric models and the horizontal wind model require the satellite position and velocities inputs in F_E. So the accelerations are computed in F_E and then transformed into F_I J2000 for being used in the POD. The panel normal vector $\vec{n}$ is transformed from F_B to F_E in a similar procedure as described for radiation pressure forces.

5.5. ASSUMPTIONS

Before starting to present the results of the orbit validations for the implemented models, it is important to collect all the assumptions made :

- Aerodynamic forces
  - The GSI is solely diffuse.
  - The satellite is moving in a free molecular flow.
  - Modelled accelerations are equal to the true accelerations, no scaling factor is used.
- Radiation pressure
  - Solar irradiance at a fixed Sun distance is assumed constant in time.
  - The sunlight is reflected by the TOA surface.
  - Modelled accelerations are equal to the true accelerations, no scaling factor is used.
- Satellite modelling
  - Satellite surface is assumed to have a constant temperature of 300 K.
  - The panels are convex (particles and photons interact only once with the satellite surface).
  - The panels are not shadowing each-other (the self-shadowing effect is not accounted for).
  - The surface material is not ageing
- Earth modelling
  - Earth TOA is ellipsoidal.
  - Earth TOA surface is acting like a prefect Lambertian surface.
  - The atmosphere without wind is co-rotating with the Earth.

5.6. VALIDATION OF THE IMPLEMENTATIONS

Before testing the influence of implemented forces upon satellite orbits, one has to make sure that the implementation is correct. To do so, the magnitude, the direction and the consistency with literature has been tested using a single panel satellite. In this section, only the relevant coherence tests will be shown because the implemented models are well described in Chapters 6, 7 and 8.

5.6.1. AERODYNAMIC FORCES

In order to obtained results easily verifiable with the theory, a satellite made of one single panel has been defined. The normal vector of this panel is aligned with the velocity vector when the angle θ is 0. Then the panel has been rotated w.r.t the velocity vector around the perpendicular axis, as shown in Fig. 5.8.

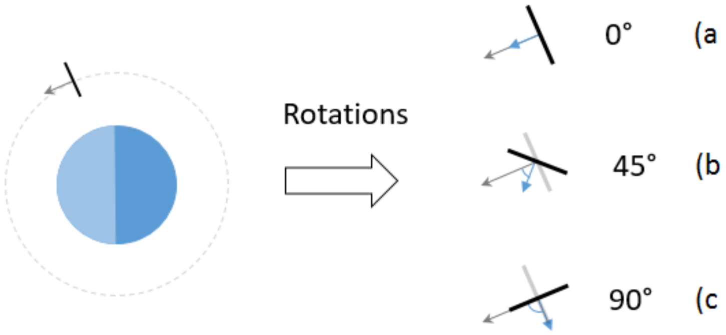

Figure 5.8: Testing the implementation of the aerodynamic forces with a single plate. The panel's velocity vector is indicated in grey and the panel normal vector in blue.

In order to check the implementations of the aerodynamic drag and lift coefficients, they have been computed for a single flat panel for different values of the angle θ, between the plate normal vector and the velocity vector. The computed drag coefficient is expected to be largest when the panel is front looking (i.e perpendicular to the flow, Fig. 5.8 a) and to gradually decrease with increasing θ. Similarly, the lift force is expected to gradually rise until θ=45° (in Fig. 5.8 b), and then to gradually decrease for larger angles [10, 42]. This test has been carried out at the Swarm C position on the first of January, 2015 and the atmosphere has been assumed not rotating, thus $\vec{V}_r = \vec{V}$, and no wind model was used. The computed lift and drag coefficients are shown in Fig. 5.9 at different θ angles.

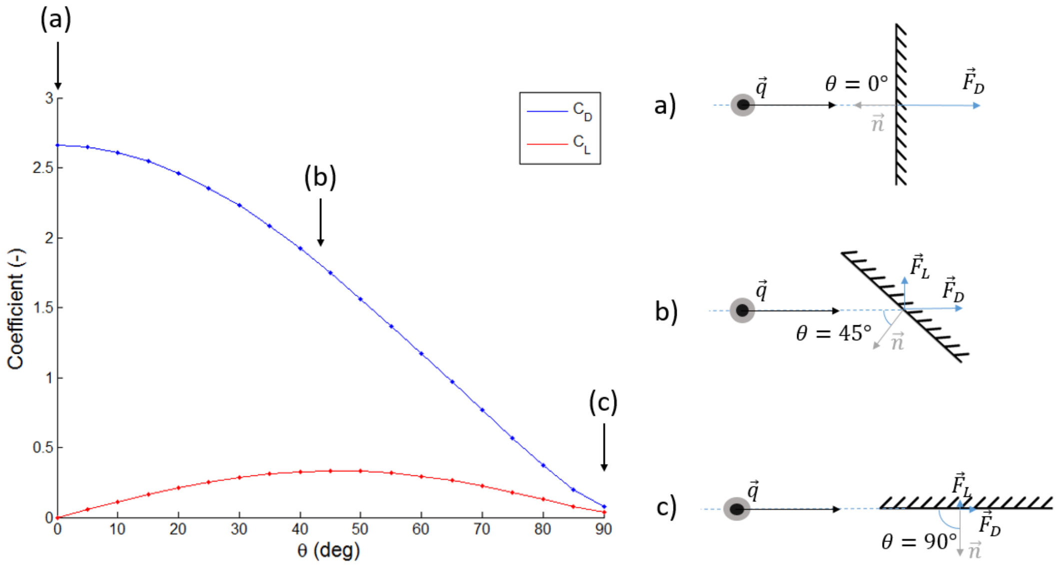

Figure 5.9: Computed C_D and C_L with Swarm C flight conditions. The black dot illustrates the atmospheric particles that are going to hit the panel.

Note that C_D and C_L are not equal to zero when the panel is parallel to the flow (point C). In fact, it is due to the thermal motion of the particles, which may create a small force even when $\theta = 90$ °[10]. The reason why C_L is equal to 0 when $\theta = 0°$ is because the projection parameter l (shown in Eq. 3.11) is 0 when the panel is perpendicular to the flow. Fig. 5.9 demonstrates a full consistency with the expectations regarding the aerodynamic coefficients found in [10, 42].

5.6.2. SOLAR RADIATION PRESSURE

In the same way as the aerodynamic force, the solar radiation pressure has been tested with a single panel. The radiation pressure coefficients $\vec{C}_r$ was computed for different angles θ between the plate normal vector and the direction satellite-Sun (see Fig. 5.10).

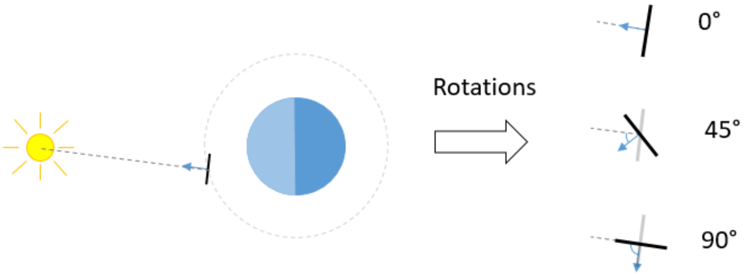

Figure 5.10: Testing the implementation for direct SRP with a single plate. The satellite-Sun direction is indicated with a dotted grey line and the panel normal vector in blue.

This test has been carried out with single panels of different optical properties, namely one absorbing the photons $p_a = 1$, another one reflecting specularly ($p_s = 1$) and one last reflecting diffusively $p_d = 1$. Fig. 5.11 shows the norm of $\vec{C}_r$ (Eq. 4.6).

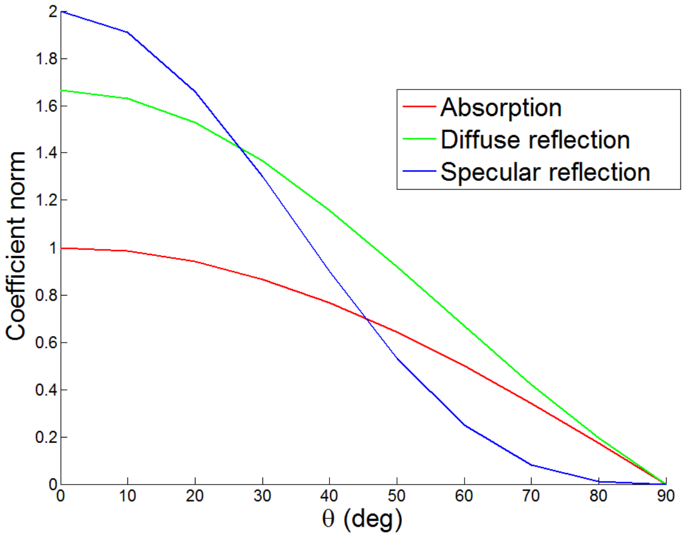

Figure 5.11: Amplitude of the photon-surface interaction coefficient, varying with θ. The areas A and A_{ref} have been set to 1.

When the panel is facing the Sun, the specular reflection coefficient $\vec{C}_s$ is exactly twice as large as the absorption coefficient $\vec{C}_a$ because the momentum transferred to the panel is twice as large. The crossing points of the different coefficients at 26.7°and 45.0°can be algebraically verified, see Appendix D. Thus, the implementation yields results which are in line with the theoretical expectations.

5.6.3. EARTH RADIATION PRESSURE IMPLEMENTATION VALIDATION

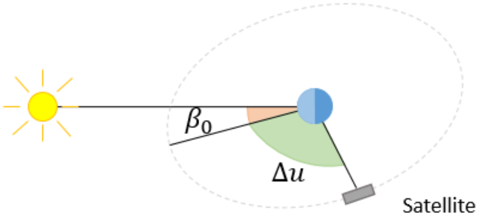

Figure 5.12: ERP key parameters

While SRP and aerodynamic forces are based on one incoming direction of the force, ERP has many (the directions to each relevant TOA element). This makes the use of one single panel satellite pointless, thus the validation of the implementation must be adjusted accordingly. Using the Swarm C macro-models, coherence of the computed ERP w.r.t. the Sun position was verified. To do so, the Sun elevation angle above the orbital plane of the satellite β_0 and the argument of latitude of the satellite w.r.t and the argument of latitude of the Sun Δu have been used (see Fig. 5.12). The largest reflected ERP is expected to occur when β_0 and Δu are close to 0°[57].

In order to compute the accelerations at different beta angles, reflected (Fig. 5.13) and emitted (Fig. 5.14) ERP have been computed for 28 different days of 2014[9]. The CERES data of August have been used and the actual mass of Swarm (468 km) has been used. The radial acceleration caused the reflected ERP (see Fig. 5.14 a) is as expected much larger than in along-track and cross-track directions. For each axis the acceleration drops to 0 for $|\Delta u| > 100°$. The accelerations on the along-track and the cross-track axis are varying in sign, which was also expected. Fig. 5.14 shows larger positive accelerations in the radial direction. Since the emitted ERP was expected to be uniform, the clear acceleration variations (mostly visible in Fig. 5.14 a) are due to the Earth maps of optical properties given by CERES. Indeed the emissivity and the reflectivity maps seems well correlated with the latitude (see Figs. 5.7 and 5.6, at a given latitude the optical properties are varying a little). In summary, the dark blue and light blue parts of Fig. 5.14 (mostly visible in Fig. 5.14 a) are corresponding with the largest and smallest latitude of Fig. 5.15, so the accelerations in dark blue are when the satellite is above the South Pole and the accelerations in light blue when the satellite is above the North Pole. Both Figs. 5.14 and 5.13 are consistent with similar plots shown in [57].

---

[9] Every fifth day from day 200 (19.07.2014) to day 340 (06.12.2014).

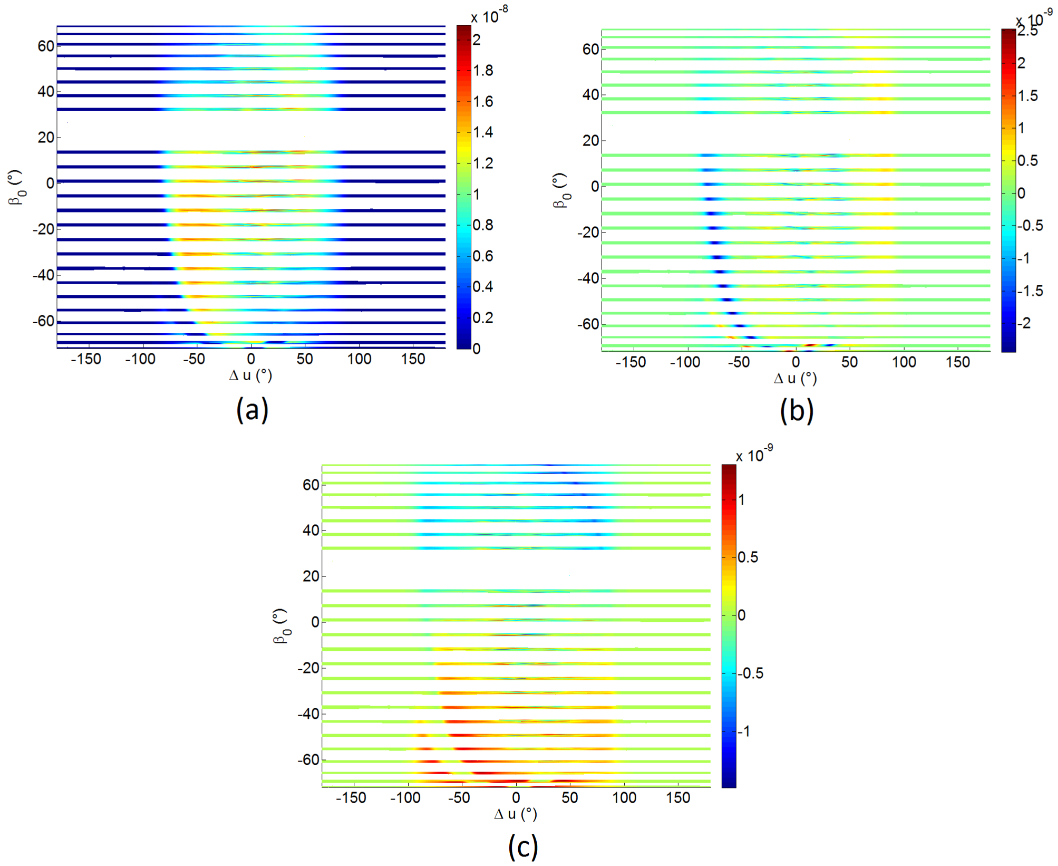

Figure 5.13: β_0 - Δu reflected ERP accelerations in m/s^2. Radial- (a), Along-track- (b) and Cross-track-axis (c).

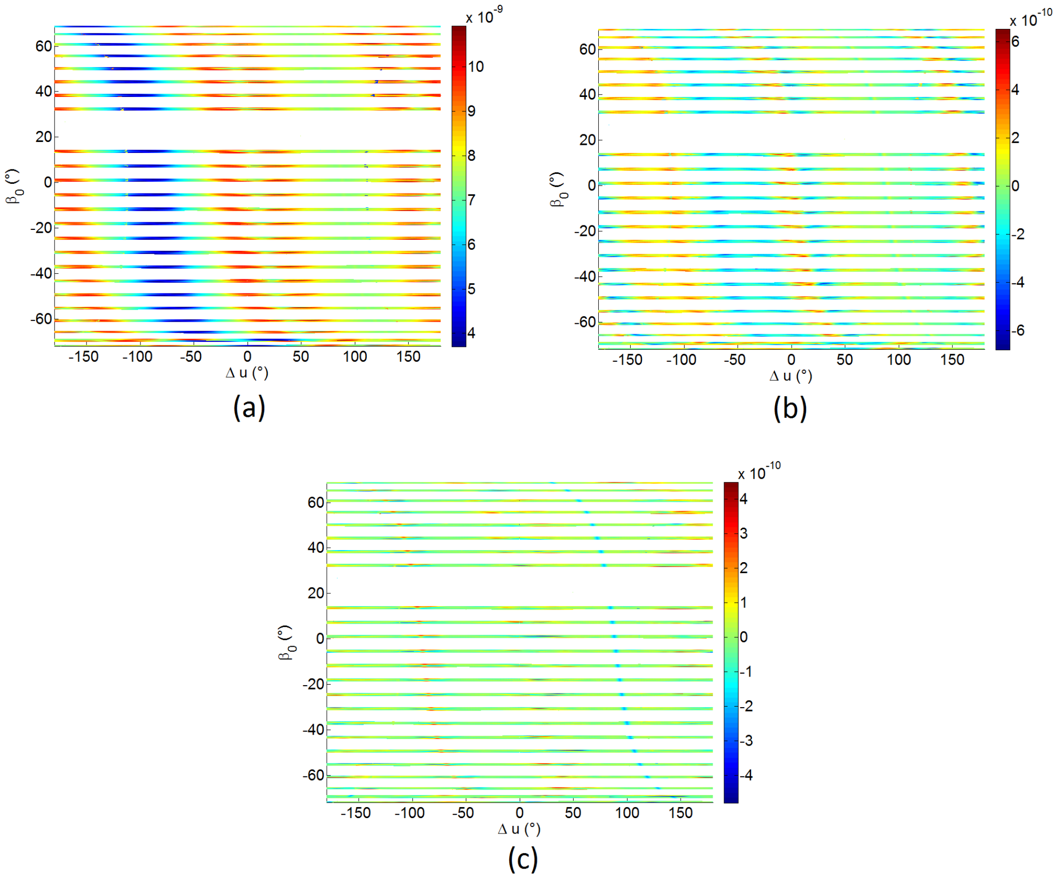

(a)

(b)

(c)

Figure 5.14: β_0 - Δu emitted ERP accelerations in m/s^2. Radial- (a), Along-track- (b) and Cross-track-axis (c).

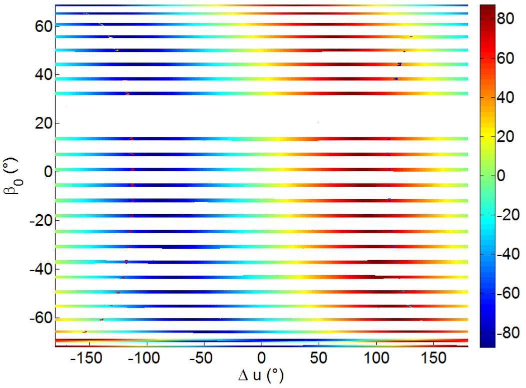

Figure 5.15: Latitude of the satellite in degrees as function of β_0 and Δu.

6

INDIVIDUAL NON-GRAVITATIONAL ACCELERATIONS ANALYSIS

In this Chapter, each modelled acceleration for Swarm C will be compared against external data, kindly provided by E. Doornbos (TU Delft). The purposes of those comparisons are: to verify that the modelled accelerations are consistent with the external data, evaluate the impact of the different parameterizations (wind model, algorithm to compute the accommodation coefficient, atmospheric model and macro-models optical properties) and identify the setting that is closest to external data. Supported by statistics, a discussion will focus on the possible causes of mismatch between modelled and external data. Special attention will be given to the aerodynamic forces because they are the largest non-gravitational forces for Swarm and GRACE by one order of magnitude. The reader is requested to pay particular attention to the scale of the Figures, which varies from one plot to another.

Table 6.1 states the implementation details of the modelled and external data. The NRTDM software (mentioned in Sec. 3.3) uses the ANGARA Monte-Carlo Test Particle method for the radiation pressure and the aerodynamic force coefficient calculations [80]. This will illustrate the difference between the implemented "conventional" method and the test particle method. The sample days are from day 213 to 236 of the year 2014. The accelerations are compared in the satellite body-fixed reference frame (X_B,Y_B,Z_B). In order to allow for numerical comparisons, the epoch of the modelled and external data have been synchronized (every 30 seconds). However, the epoch of the modelled and external accelerations could not be synchronized for the days 217, 221 and 222 (because the two epoch where shifted). In order to numerically compare the acceleration difference, two efficient mathematical tools are employed: the mean value (see Eq. 6.1) and standard deviation (STD) (see Eq. 6.2). The statistics provided in this section are always computed based on all the available days from 213 to 236 of the year 2014, without the days 217, 221 and 222.

$$\overline{\Delta a} = \frac{1}{L}\sum_{i=1}^{L}\Delta a_i \tag{6.1}$$

$$\Delta a_{STD} = \sqrt{\frac{1}{L}\sum_{i=1}^{L}(\Delta a_i - \overline{\Delta a})^2} \tag{6.2}$$

i	epoch i
L	total number of epochs
Δa_i	difference between computed and external accelerations at epoch i
$\overline{\Delta a}$	mean value of the acceleration differences
Δa_{STD}	standard deviation of the acceleration differences

6.1. AERODYNAMIC FORCES

In this Section, the differences w.r.t. the external data are presented first. Then the influence of the wind model, the chosen algorithm to compute the accommodation coefficient, and the atmospheric model are assessed both graphically and numerically.

Implementation detail	**Computed data**	**External data**
Software	Bernese GNSS Software	NRTDM [80]
Accommodation coefficient α	modelled	fixed value: 0.93
Use of scaling factor	No	No
Use of bias	No	No
Atmospheric model	NRLMSISE-00/DTM2013	NRLMSISE-00
Atmospheric density modelling	Directly given by NRLMSISE-00/DTM2013	Iterative algorithm including NRLMSISE-00 and calibrated measured accelerations [80]
Earth modelling, optical properties	Monthly mean map of TOA optical proerties, CERES data	Monthly mean map of TOA optical properties, ERBE data
Earth modelling, shape	Ellipsoid	Sphere for radiation pressure calculations, ellipsoid for altitude and aerodynamic model evaluation
Horizontal wind correction	Directly given by HWM14	Iterative algorithm including HWM07 and calibrated measured accelerations [80]
Satellite modelling	macro-models	macro-models (different from the one used in this assignment)
Satellite optical properties	Fixed (no ageing)	Fixed (no ageing)

Table 6.1: Settings of the modelled and the external data

6.1.1. DIFFERENCE W.R.T. THE EXTERNAL DATA

Fig. 6.2 shows that even if both the computed and the external accelerations have a similar pattern, a difference is visible on each axis (mostly on the X_B-axis). Since the difference seems to change from day to day (Fig. 6.1), a daily least squares adjustment has been applied to rescale the external data of the day 213 and 214 (see Sec. 7.2 for more details about the algorithm involved) in order to determine whether the difference can be reduced with a bias or a scaling factor. Fig. 6.2 also shows the accelerations of days 213 and 214 (because the daily variation is well visible) before and after the rescaling, Table 6.2 details the estimated biases and scaling factors. An important observation is that for each axis, and for both days, the bias is two orders of magnitude smaller than the computed acceleration, which means that the difference is largely due to a scale difference. This important point confirms that the modelled accelerations are consistent with external data.

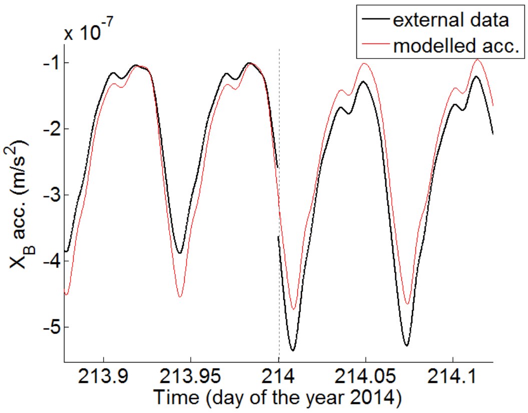

Figure 6.1: External (black) and modelled (red) aerodynamic accelerations for Swarm C in X_B-direction for two subsequent days. The differences between the accelerations change from one day to the next. The external acceleration shows a discontinuity at the day boundary (highlighted with the dotted line).

The reader is probably wondering what could be the origin of this scale. While the modelled accelerations use the NRLMSISE-00 and HWM14 to compute the density and wind, the NRTDM use and iterative algorithm

	Day 213		Day 214	
Axis	**Bias** (m/s^2)	**Scaling factor**	**Bias** (m/s^2)	**Scaling factor**
X_B-axis	-4.13 E-09	1.18	4.73 E-09	0.90
Y_B-axis	-5.89 E-10	1.07	-3.75 E-10	0.92
Z_B-axis	1.24 E-10	1.10	1.54 E-12	0.91

Table 6.2: Scale factors and biases estimated in a least squares adjustment of the external aerodynamic accelerations to the modelled accelerations. The atmospheric model used is NRLMSISE-00 and the Goodman's method with $f = 3.6$ (see Eq. 3.18) has been used to compute the accommodation coefficient α.

to extract the density and wind (based on NRLMSISE-00, HWM07 and calibrated measured accelerations). A different atmospheric density rescale the computed accelerations (see Eq. 3.1), thus lead to the difference visible in Fig. 6.1. Similarly, different solar indices input when using NRLMSISE-00 would also lead to daily changes (of the external data). In Appendix F it is shown that a 5% increase of the solar and geomagnetic indices lead to scaling factors of approximately 0.89 for the three axis and no bias.

Further in this section, the Figures are showing the differences between the modelled and the original external accelerations (otherwise the differences are less visible). On the other hand, the statistics given in Tables have been computed for both the differences between the modelled and the original accelerations, and the differences between the modelled and the daily adjusted accelerations. Both statistics are showing the same trend, but as the least-squares adjustment absorbs the small offset, the mean values of the differences between the modelled and the daily adjusted accelerations are irrelevant. For this reason, the statistics with the adjusted accelerations are given in Appendix F because the STD could interesting. Note that the statistics are always given based on the entire sample days.

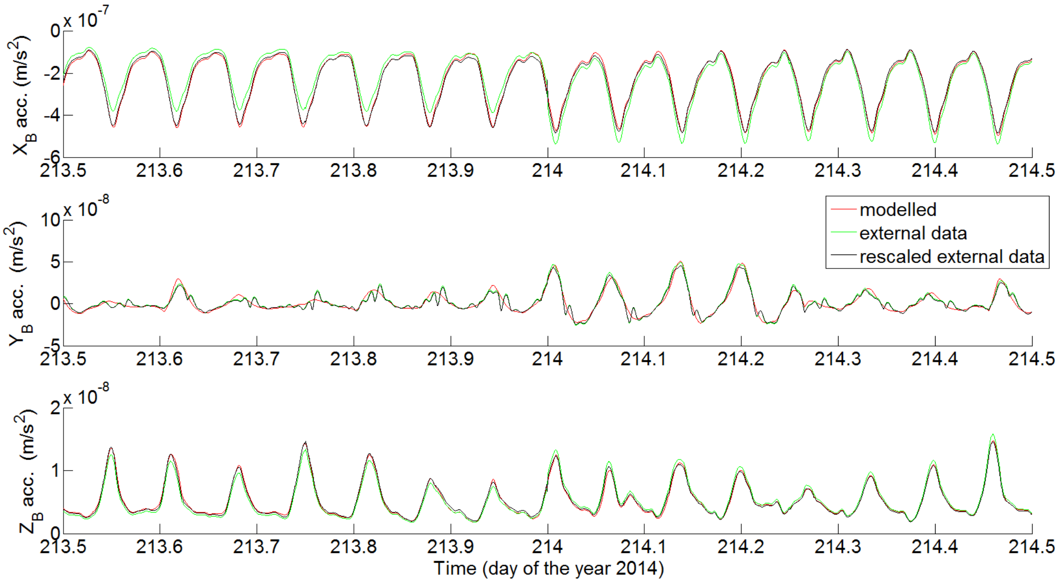

Figure 6.2: Modelled (red), external (green), and adjusted (black) external aerodynamic accelerations for days 213 and 214 of 2014.

6.1.2. WIND MODEL

Fig. 6.3 shows that the influence of the wind model is only visible on the Y_B-axis. Because a horizontal wind model is mostly on the X_O-Y_O plane and since the attitude correction between F_B and F_O frames is small, the X_O-Y_O plane is close to the X_B-Y_B plane. Moreover, it is less visible on the X_B-axis because the velocity correction is much smaller than the satellite velocity. The corresponding statistics of the difference between modelled and adjusted external accelerations are given in Table 6.3, which clearly demonstrates a reduction of both the mean and the STD over the 3 axes. The largest improvement is indeed along the Y_B-axis. In terms of values, the reduction the mean values are -8.91% in X_B direction, -17.78% in Y_B direction and -13.37% in Z_B direction. For the standard deviations, a reduction of -1.26%, -45.33% and -3.16% in X_B-, Y_B- and

	Mean (m/s^2)			**STD** (m/s^2)		
Setting	X_B-axis	Y_B-axis	Z_B-axis	X_B-axis	Y_B-axis	Z_B-axis
No wind model	-3.06E-09	3.13E-10	4.29E-11	3.00E-08	3.24E-09	5.11E-10
HWM14	-2.79E-09	2.57E-10	3.72E-11	2.96E-08	1.77E-09	4.95E-10

Table 6.3: Statistics of the differences between the modelled and **original** external aerodynamic accelerations. The atmospheric model used is the NRLMSISE-00 and Goodman's method with $f = 3.6$ has been used to compute α.

Z_B-axis respectively are observed in using HWM14.

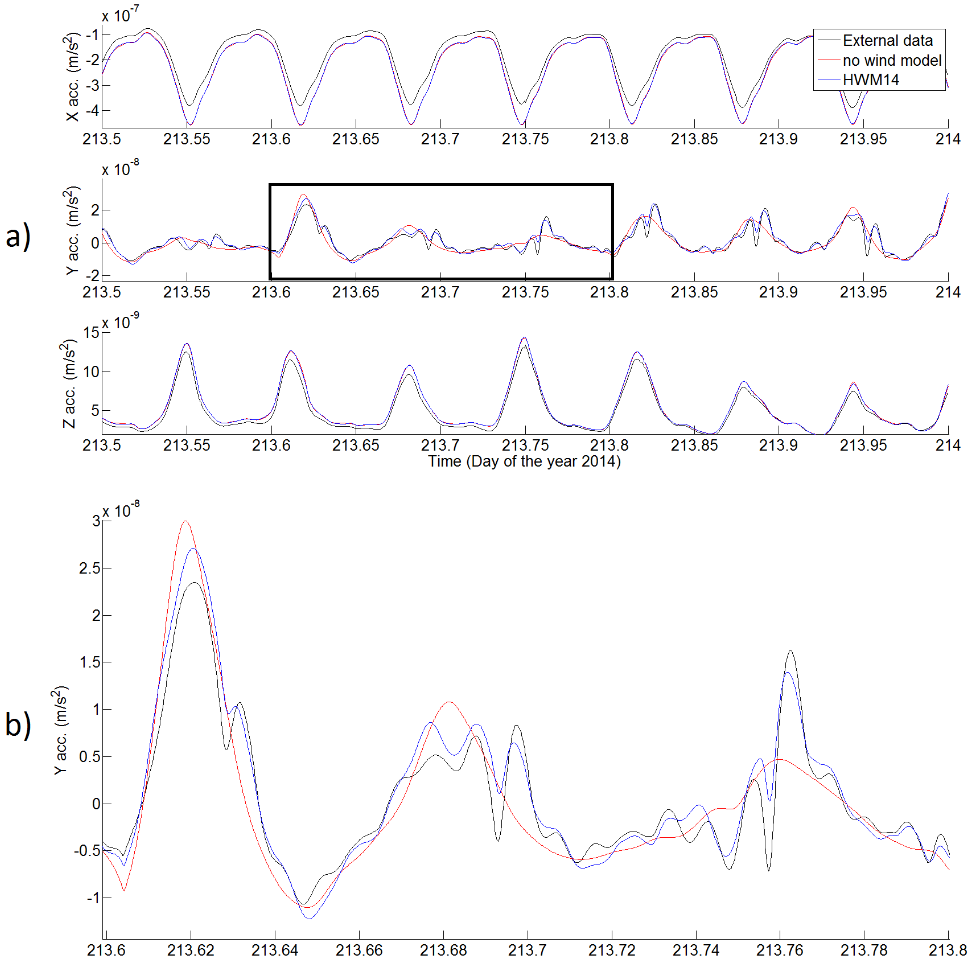

Figure 6.3: Influence of wind model upon aerodynamic acceleration, a) day 213 (2014), b) zoomed-in black rectangle of (a)

6.1.3. ACCOMMODATION COEFFICIENT

While the external accelerations have been computed with a constant accommodation coefficient of 0.93, in the implemented model it is computed at each epoch. In the following, four different methods to compute the accommodation coefficient are tested. On one hand, $\alpha_{G,1}$ and $\alpha_{G,2}$ are defined using Goodman's definition 3.18, with a factor f equal to 2.4 and 3.6 respectively. These two factors have been used in the past and $f = 3.6$ eventually became the benchmark. On the other hand, $\alpha_{P,1}$ and $\alpha_{P,2}$ are defined using Pilinski's definitions 3.20, with a coefficient K equal to 5.0×10^{-17} and 7.5×10^{-17} respectively. The motivation to test those two values are because E. Doornbos uses a factor of 5.0×10^{-17} [10], but Pilinski a factor of 7.5×10^{-17} and no one is *a priori* more precise[1]. However regarding Goodman's and Pilinski's methods, the latter is expected to be

---

[1] Pilinski also claims that $K = 7.5 \times 10^{-17}$ only fits for NRLMSISE-00 atmospheric model.

	Mean (m/s^2)				**STD** (m/s^2)			
Setting	α	X_B-axis	Y_B-axis	Z_B-axis	α	X_B-axis	Y_B-axis	Z_B-axis
$\alpha_{G,1}$	0.60	-2.43E-08	7.50E-10	1.27E-09	0.006	3.28E-08	2.80E-09	9.49E-10
$\alpha_{G,2}$	0.90	-0.28E-08	2.57E-10	0.04E-09	0.009	2.96E-08	1.77E-09	4.95E-10
$\alpha_{P,1}$	0.47	-2.53E-08	4.12E-10	1.35E-09	0.165	3.05E-08	2.71E-09	6.86E-10
$\alpha_{P,2}$	0.56	-2.03E-08	2.77E-10	1.06E-09	0.163	2.99E-08	2.36E-09	5.85E-10

Table 6.4: Statistics of the differences between the modelled and **original** external aerodynamic accelerations. The mean and STD value of the modelled α is also shown. NRLMSISE-00 and HWM14 have been used.

better [10]. In summary the following four expressions for α are tested:

$$\alpha_{G,1} = \frac{2.4\mu}{(1+\mu)^2} \tag{6.3}$$

$$\alpha_{G,2} = \frac{3.6\mu}{(1+\mu)^2} \tag{6.4}$$

$$\alpha_{P,1} = \frac{5.0\times10^{-17}P}{1+5.0\times10^{-17}P} \tag{6.5}$$

$$\alpha_{P,2} = \frac{7.5\times10^{-17}P}{1+7.5\times10^{-17}P} \tag{6.6}$$

For each expression the aerodynamic accelerations are computed and compared to the external data. Fig. 6.4 shows the calculated aerodynamic accelerations when α is computed with Goodman's method or Pilinski's method. For clarity reasons only the accelerations based on $\alpha_{G,2}$ and $\alpha_{P,2}$ are plotted, but the statistics of the four cases are detailed in Table 6.4. The mean value of the computed accommodation coefficient (also computed over all days) based on Goodman's method with $f = 3.6$ (i.e. $\alpha_{G,2}$) is the closest to the external data's fixed value of 0.93. Therefore it is not surprising that the standard deviations of the corresponding acceleration differences of $\alpha_{G,2}$ are the lowest. Note that when the Goodman's method is used, the computed accommodation coefficient is almost constant (very small STD in Table 6.4). In Fig. 6.4, the amplitude seems to always be larger when Pilinski's method is used. Since the accommodation coefficient is smaller when Pilinski's method is used (see Table 6.4), it means that a larger accommodation coefficient tends to reduce the amplitude of the computed force. It makes perfect sense because larger α means larger transfer of thermal energy from the particle to the satellite, then the particle is transferring less momentum.

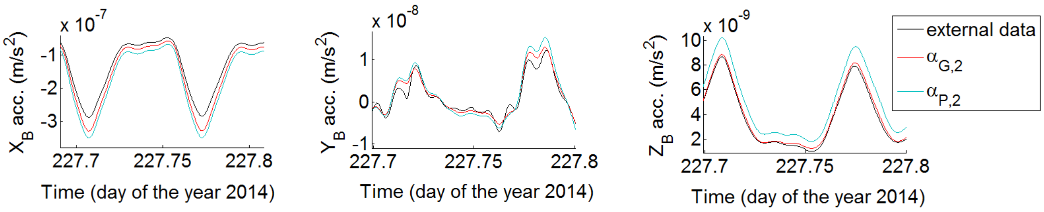

Figure 6.4: Influence of accommodation coefficient upon aerodynamic acceleration for part of day 227. Goodman's method with $f = 3.6$ (red plot) and Pilinki's method with $K = 7.5\times10^{-17}$ (blue plot) have been used.

	Mean (m/s^2)			**STD** (m/s^2)		
Setting	X_B-axis	Y_B-axis	Z_B-axis	X_B-axis	Y_B-axis	Z_B-axis
NRLMSISE-00	-0.28E-09	2.57E-10	0.37E-10	2.96E-08	1.77E-09	4.95E-10
DTM2013	1.20E-08	1.06E-10	-2.61E-10	3.48E-08	2.22E-09	6.65E-10

Table 6.5: Statistics of the differences between the modelled and **original** external aerodynamic accelerations over the available sample days. HWM14 has been used with the two atmospheric models and $\alpha_{G,2}$ definition has been used to compute the accommodation coefficient.

	Mean (m/s^2)			**STD** (m/s^2)		
Setting	X_B-axis	Y_B-axis	Z_B-axis	X_B-axis	Y_B-axis	Z_B-axis
$f_a = 1.0$	3.96E-10	-8.04E-10	1.00E-09	1.70E-09	1.76E-09	1.29E-09
$f_a = 0.5$	3.97E-10	-8.31E-10	1.02E-09	1.72E-09	1.76E-09	1.27E-09

Table 6.6: Statistics of the differences between the modelled and external SRP accelerations when using two different values for f_a.

6.1.4. ATMOSPHERIC MODEL

Table 6.5 details the statistics of the acceleration differences when using either the NRLMSISE-00 or the DTM2013 atmospheric model. Since NRLMSISE-00 has been used by E. Doornbos to compute the external data, it is not surprising that the STD of the acceleration differences are indeed smaller with NRLMSISE-00. Surprisingly, the mean value in the Y_B direction is smaller when DTM2013 is used. This is probably caused by the daily rescaling of the external accelerations w.r.t. the modelled accelerations[2].

6.2. SOLAR RADIATION PRESSURE

Since the physics underlying the modelled (see Sec. 4.3) and external SRP [80] are the same, two sources of differences are expected: the shadowing function modelling and the optical properties of the satellite surface. Therefore this section focuses on the impact of these quantities on the modelled accelerations.

It will be shown that unlike the aerodynamic force, the scaling mismatch of the solar radiation pressure is very small, which may be caused by the macro-models optical properties. Therefore different macro-models will be tested with different optical properties.

6.2.1. SHADOWING FUNCTION

With the chosen shadowing function (see Sec. 4.3), f_a (the amount of refracted sunlight that is not absorbed by the atmosphere) is the only coefficient which suffers from uncertainty. As discussed in Sec. 4.3, no precise value of f_a has been found in the literature and modelling is fairly complex. Initially, assumed equal to one, also $f_a = 0.5$ was used to compute SRP. Fig. 6.5 and Table 6.6 show the impact of changing f_a. Again, the external data have not been adjusted, so it is noteworthy to see in Fig. 6.5 how close the modelled accelerations are to the external data. Changing f_a leads to only marginal change. Since the external data seems to be based on the same shadowing function [80], the smoother transition of external data is due to a larger time interval, but not only. One can guess that the external data are accounting for effects of absorption and refraction which cause the difference[3]. Table 6.6 shows very small differences: the mean values of the case with $f_a = 1.0$ are smaller in magnitude, so closer. The STD of $f_a = 1.0$ is smaller on the X_B-axis and increased on the Z_B-axis. In terms of values, the mean values with $f_a = 0.5$ are larger in the $X_B-, Y_B - and Z_B-$axis by 0.32%, 3.30% and 1.80% respectively. For the standard deviations, a reduction of -0.15% and -1.38% have been computed along Y_B- and Z_B-axis, but an increase of 1.26% in the X_B direction.

6.2.2. SATELLITE OPTICAL PROPERTIES

A proper analysis of the optical properties would require many tests, therefore this section only intends to give the reader an impression about the influence of the photon-surface interaction coefficients p_a, p_d and p_s. Three macro-models with panels of different optical properties have been defined to analyse the impact of the optical properties. In the first modified macro-models all the panels absorb the photons ($p_{a,VI} = 1$), in the

---

[2] This difference is lager when no wind model is used.

[3] It is infered that such corection *will* implemented in the NRTDM: "The precise modelling of the effects of absorption, refraction and the elliptical shape of the Earth on the eclipse have not yet been included in the current version of the processing software." [**?**] page 66. Therefore when E. Doorbos computed the accelerations these corrections have probably been implemented

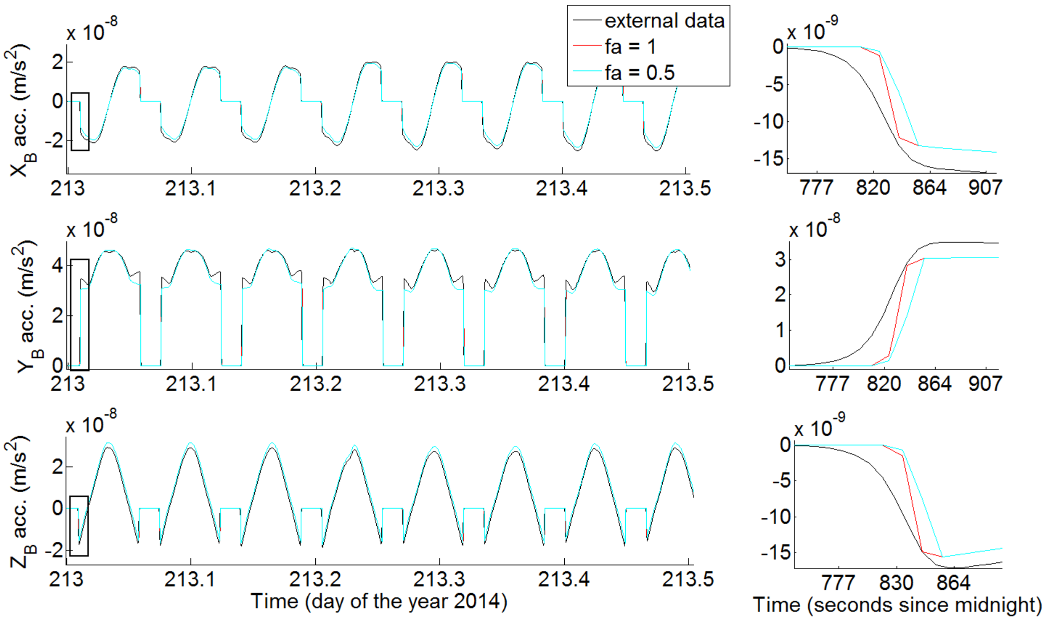

Figure 6.5: Impact of the shadowing function parametrisation upon SRP. On the right, the black rectangles are expanded.

second one all the panels are 100% specular reflecting the photons ($p_{s,VI} = 1$) and in the last one all the panels are 100% diffusely reflecting the photons ($p_{d,VI} = 1$). The mean and STD values of the differences between computed and external accelerations are given in Appendix F, because they don't clearly show the impact of the modified macro-models (they only confirm that the closer results to external data are given when the original macro-models is used). In order to see the impact of the optical properties, the least-squares adjustment between the modified and original macro-models is more suitable. This is because the scaling factor indicates if the acceleration amplitude varies and bias indicates if the acceleration is shifted. Fig. 6.6 shows the accelerations computed with the original macro-models and with 2 of the 3 modified macro-models. Table 6.7 shows the biases and scaling factors of all the modified macro-models with reference to the original one.

In Fig. 6.6 one can see the small wiggles in the Y_B-accelerations, which are visible before and after the eclipse (i.e. when the force is zero). They can be convex, concave or even flat, depending on the macro-models used. Those wiggles in the Y_B-accelerations are the largest difference w.r.t. the external data, but apparently the different optical properties of the macro-models used can explain this difference. On each axis, the different macro-models seem to induce amplitude variations. Note that the acceleration computed with the original macro-models matches best with the external data. Table 6.7 demonstrates that changing the optical properties of the macro-models leads to an increase or a reduction of the amplitude of the computed accelerations (because the scaling factor variation is large). On the other hand, the offset created by the modified macro-models is negligible (one or two orders of magnitude smaller than the computed forces).

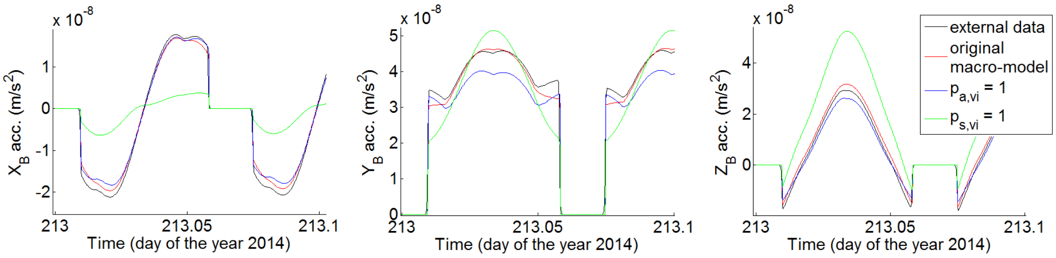

Figure 6.6: Impact of varying the optical properties of the macro-models on the SRP

	X_B-axis		Y_B-axis		Z_B-axis	
Setting	**Bias** (m/s^2)	**Scaling factor**	**Bias** (m/s^2)	**Scaling factor**	**Bias** (m/s^2)	**Scaling factor**
$p_{a,VI} = 1$	4.36E-10	0.94	0.78E-09	0.90	-0.51E-09	0.88
$p_{d,VI} = 1$	2.22E-10	1.12	1.13E-09	1.30	1.50E-09	1.42
$p_{s,VI} = 1$	-5.00E-10	0.34	-1.78E-09	1.05	3.90E-09	1.28

Table 6.7: Scaling factors and biases estimated in a least squares adjustment of the SRP accelerations modelled with various optical properties to the SRP accelerations modelled with the original macro-models. The external data is not included in this Table.

6.3. EARTH RADIATION PRESSURE

ERP is strongly dependent on the Earth's modelling. Different models for Earth albedo and emissivity are used between the computed and external data: therefore it is obvious to have different accelerations. In the same way as for SRP, the influence of the optical properties is tested and shown in Fig. 6.7 and Fig. 6.8. On the X_B-axes the modelled and the external data are hardly following similar patterns, the sign is not always in accordance but this may be due to the different Earth mappings used. On the other axes the pattern of the computed and external data are more coherent, also note that (as expected) the acceleration is one order of magnitude larger in the Z_B-direction. Table 6.8 shows large scaling factor variations, which correspond to amplitude variation of the reflected ERP acceleration differences. Interestingly, the accelerations are so small on the X_B-axis that setting $p_{s,VI} = 1$ leads to an *offset* of $1.80 \times 10^{-10} m/s^2$ which is visible in Fig. 6.7 (the green line on the X_B-axis has a visible offset in addition to a different scale factor, on the other axis the *offset* is so small that it is not visible).

Similarly, the impact of the optical properties is presented in in Fig. 6.8 and Table 6.9. The impact is the same as for the reflected ERP: changing the optical properties lead to amplitude variation (shown by the scale factor variation) in the three directions and may lead to an offset (shown by the bias) along the X_B-axis. Note that the order of magnitude of both the emitted and reflected ERP are extremely small, therefore the differences with external data are probably due to both the optical differences of the macro-models and the Earth models used. Therefore it might be good (later) to use the same Earth model. Note that The mean and STD values of the differences between computed and external accelerations are given in Appendix F because unlike the bias and scale, they don't clearly show the impact of the modified macro-models.

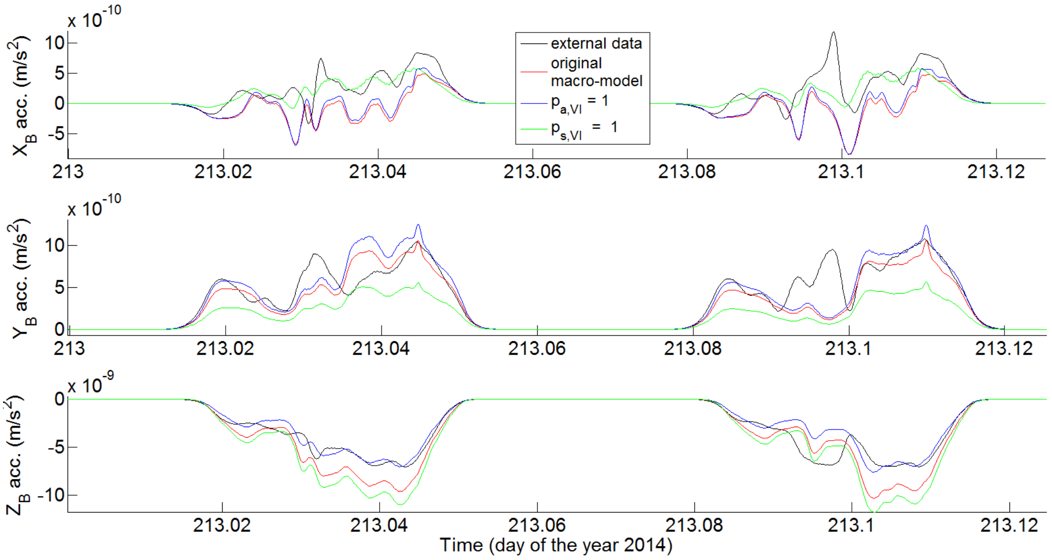

Figure 6.7: Impact of varying the optical properties of the macro-models on the reflected ERP

To conclude this Chapter, the modelled accelerations have shown consistency with the external data. The differences (especially in ERP-induced accelerations) seems to be cause by the different macro-models and Earth models used. To a larger extend, the impact of the: optical properties, the atmospheric models, the accommodation coefficient and the wind model have been evaluated. The set up that gives the closest results to the external data uses: the NRLMSISE-00 atmospheric model, the Goodman's method with a factor f=3.6

	X_B-axis		Y_B-axis		Z_B-axis	
Setting	**Bias** (m/s^2)	**Scaling factor**	**Bias** (m/s^2)	**Scaling factor**	**Bias** (m/s^2)	**Scaling factor**
$p_{a,VI} = 1$	0.35E-10	1.06	-0.81E-12	1.19	-2.27E-12	0.74
$p_{d,VI} = 1$	1.05E-10	1.24	-0.28E-12	1.46	-7.35E-12	1.25
$p_{s,VI} = 1$	1.80E-10	0.36	1.43E-12	0.53	8.52E-12	1.14

Table 6.8: Scaling factors and biases estimated in a least squares adjustment of the reflected ERP accelerations modelled with various optical properties to the reflected ERP accelerations modelled with the original macro-models. The external data are not included in this Table.

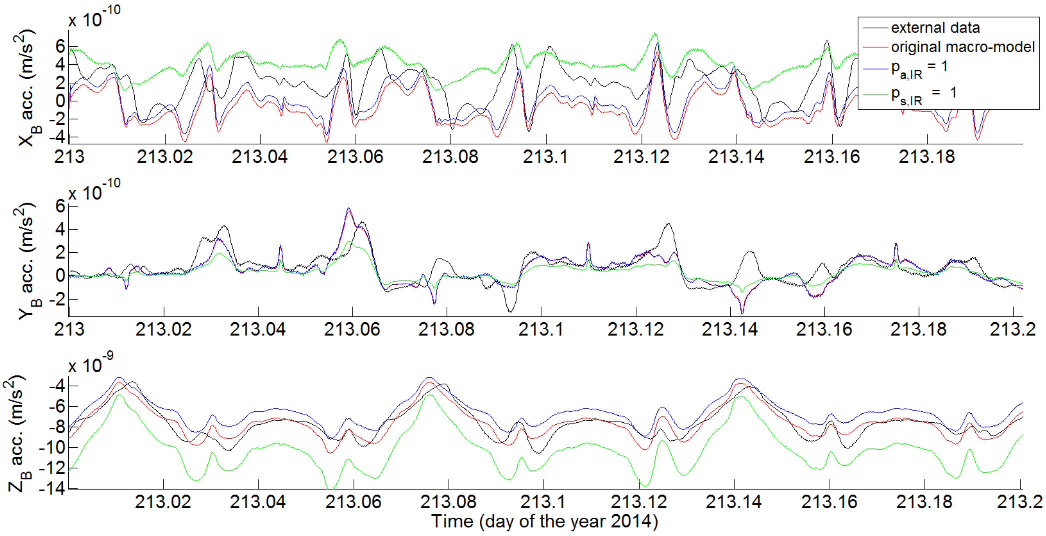

Figure 6.8: Impact of varying the optical properties of the macro-models on the emitted ERP

to compute α, the wind model HWM14, the original macro-models and $f_a = 1$ for the shadowing function.

	X_B-axis		Y_B-axis		Z_B-axis	
Setting	**Bias** (m/s^2)	**Scaling factor**	**Bias** (m/s^2)	**Scaling factor**	**Bias** (m/s^2)	**Scaling factor**
$p_{a,IR} = 1$	0.74E-10	1.01	-1.32E-13	1.04	-0.24E-11	0.87
$p_{s,IR} = 1$	2.42E-10	1.20	0.52E-13	1.32	-1.76E-11	1.48
$p_{d,IR} = 1$	4.35E-10	0.40	4.51E-13	0.55	2.28E-11	1.35

Table 6.9: Scaling factors and biases estimated in a least squares adjustment of the emitted ERP accelerations modelled with various optical properties to the emitted ERP accelerations modelled with the original macro-models. The external data is not included in this Table.

7

VALIDATION BY ORBIT DETERMINATION

In this Chapter, the impact of the implemented forces on the orbit determination of LEOs is assessed. The statistics of the orbits with, and without, modelled surface forces are computed based on time intervals of 15 seconds for all the available days from 213 to 236 of the year 2014, except the day 217 for Swarm. One parameterization[1] will be used, which has been established in the previous section: the NLRMSISE-00 atmospheric model, the Goodman's method with a factor f=3.6 to compute α, the wind model HWM14, the original macro-models and $f_a = 1$ for the shadowing function. Orbits determined with various parameterizations of the non-gravitational models are compared later in Chapter 8.

7.1. PIECEWISE CONSTANT ACCELERATIONS

In this Section, Figures and statistics will detail the impact of implemented non-gravitational forces on the estimated piecewise constant accelerations (PCA) of the reduced-dynamic orbits.

7.1.1. GENERAL ASPECTS

In this project, piecewise constant accelerations are used to absorb unmodelled or mismodelled non-gravitational accelerations in the computation of reduced-dynamic orbits (see also Sec. 5.1). Therefore the implemented non-conservative forces are expected to show a reduction of the PCA. Two aspects are considered as an improvement: amplitude and offset reduction. The amplitude is reflected in the standard deviations and the offset in the mean values of the PCA. Additionally, to compare the statistics, it is interesting to visualize the evolution of the remaining PCA in the process of implementing more and more non-gravitational accelerations. The PCA spacing is six minutes and the a priori sigma (constraints) of the radial, along-track and cross-track accelerations have been set to $5.0 \times 10^{-9} m/s^2$. It is also important to mention that the accelerations are shown in the orbital frame F_O.

7.1.2. SWARM C VALIDATION

Since the non-gravitational forces are computed independently, it is possible to include them one by one to better observe their individual influence on the orbit. Fig. 7.1 shows the influence of the non-gravitational forces upon the PCA when introduced one by one: emitted ERP, reflected ERP, SRP, atmospheric lift and atmospheric drag. The statistics for every additional non-gravitational force are detailed in Table 7.1. In addition the daily means and STD are shown for the case with no surface forces and with all the surface forces (see Fig. 7.2).

The first three lines of Table 7.1 show that the emitted and reflected ERP are reducing the mean value of the PCA of Swarm C in the radial direction but slightly increase the STD. Once SRP is introduced (fourth line), the effect of ERP is counteracted. Because those forces are both acting along the radial axis (except when $\beta_0 = 90°$. Note that during the chosen period, $\beta_0 \cong 58°$ during the day 213 and $\beta_0 \cong 31°$during the day 236. The introduction of SRP also reduces the offset and the amplitude on the along-track and cross-track direction. The introduction of the lift force increases the offset in the radial direction and reduces it in the cross-track direction, but reduces the amplitudes along the same axis. Finally, the implementation of

---

[1] The setting used in the *Bernese GNSS Software* for POD is always the same, the only difference is whether or not the surface forces are modelled.

the drag force lowers the amplitude and offset on the three axes, but mostly in along-track. In the end, the implementation of all the forces reduces the standard deviation of the PCA on each axis (-7% on R, -53% on S and -22% on W). Regarding the mean values a large reduction is observed in: along-track and cross-track direction, but the mean accelerations in radial direction increase by a few percent (8% on R, -141% on S and -98% on W). A further investigation (see Appendix H) revealed that inaccurate optical properties may be the origin of this radial increase. It is important to recall that the drag coefficient is here modelled, estimating it would probably further reduce the PCA. However, that risk to absorb accelerations which are not due to the atmospheric drag.

The daily mean values and standard deviations are shown in Fig. 7.2 for the cases of no surface forces and all surface forces included. It is also visible that the mean values in the radial direction are slowly increasing from day 213 to day 236, in the meantime β_0 angle is decreasing. Then the SRP is probably playing a key role in this "radial anomaly" (see Appendix H). While the amplitude of the PCA is clearly reduced with the implemented non-gravitational forces, the offset reduction depends on the axis. The peak at day 215 is due to one single large peak of the PCA (see Appendix G).

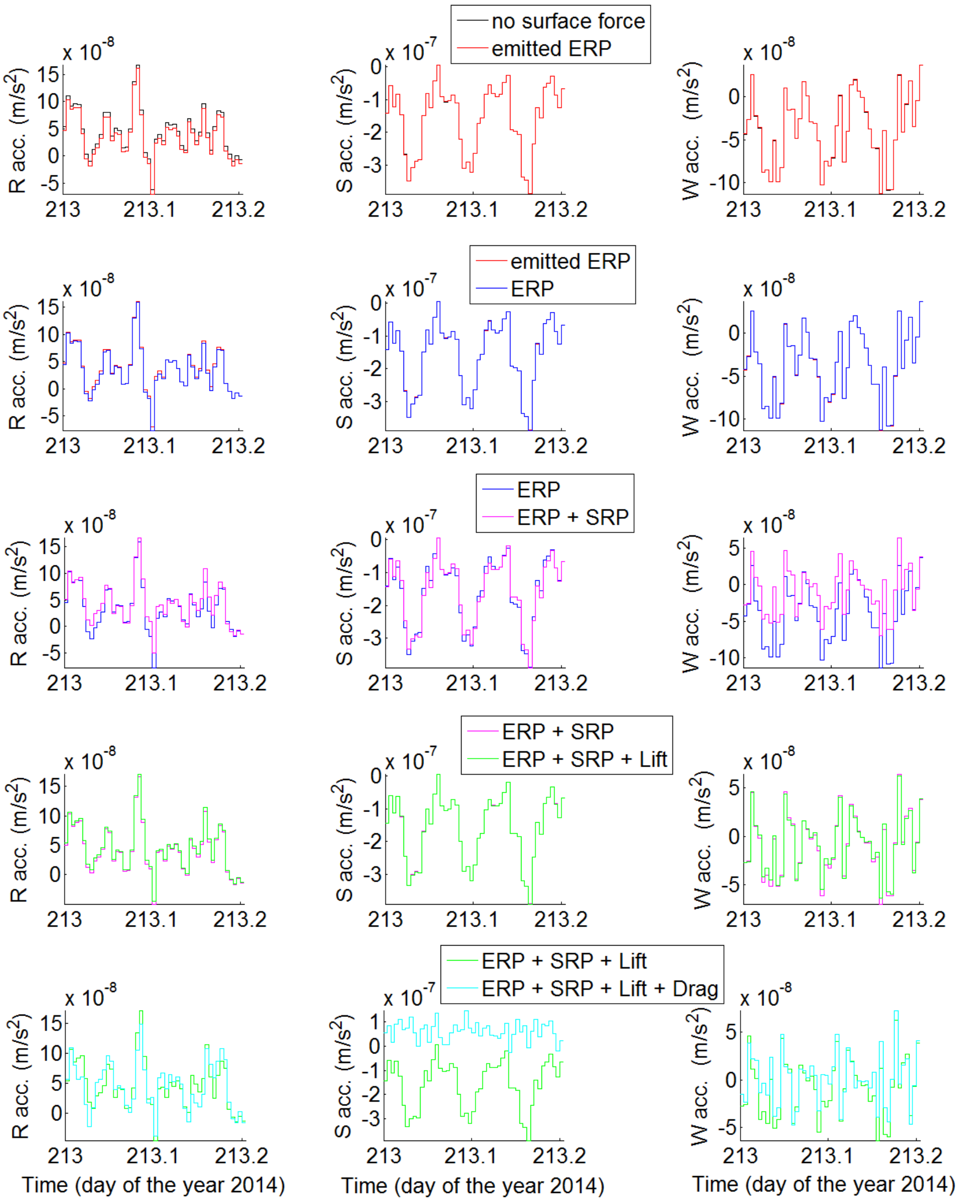

Figure 7.1: Impact of the non-gravitational forces on the piecewise constant accelerations for Swarm C when implemented one by one.

	Mean (m/s^2)			STD (m/s^2)		
Setting	**Radial**	**Along-track**	**Cross-track**	**Radial**	**Along-track**	**Cross-track**
No surface force	4.55E-08	-1.32E-07	-3.04E-08	4.96E-08	9.69E-08	4.51E-08
Emitted ERP	3.80E-08	-1.32E-07	-3.04E-08	4.99E-08	9.70E-08	4.51E-08
+ Reflected ERP	3.45E-08	-1.32E-07	-3.02E-08	5.14E-08	9.70E-08	4.51E-08
+ SRP	4.66E-08	-1.31E-07	-0.82E-08	4.70E-08	9.44E-08	3.75E-08
+ Aerodyn. lift	4.91E-08	-1.31E-07	-0.77E-08	4.69E-08	9.44E-08	3.70E-08
+ Aerodyn. drag	4.90E-08	0.54E-07	-0.06E-08	4.64E-08	4.60E-08	3.51E-08

Table 7.1: Statistics of the piecewise constant accelerations for Swarm C when the non-gravitational forces are implemented one by one. The statistics are computed based on the 23 sample days from day 213 to 236, except day 217, of the year 2014.

	Mean			STD		
Setting	**Radial**	**Along-track**	**Cross-track**	**Radial**	**Along-track**	**Cross-track**
No surface force	5.83E-09	-2.58E-07	2.58E-08	3.44E-08	1.11E-07	1.97E-08
Emitted ERP	-2.87E-09	-2.58E-07	2.57E-08	3.45E-08	1.11E-07	1.97E-08
+ Reflected ERP	-9.06E-09	-2.58E-07	2.55E-08	3.47E-08	1.11E-07	1.97E-08
+ SRP	5.44E-09	-2.58E-07	1.22E-08	3.55E-08	1.13E-07	2.14E-08
+ Aerodyn. lift	2.34E-09	-2.58E-07	1.19E-08	3.54E-08	1.13E-07	2.04E-08
+ Aerodyn. drag	2.76E-09	0.31E-07	1.69E-08	1.06E-08	0.42E-07	1.58E-08

Table 7.2: Statistics of the piecewise constant accelerations of GRACE A when the non-gravitational forces are implemented one by one. They are computed based on the 24 sample days from day 213 to 236 of the year 2014.

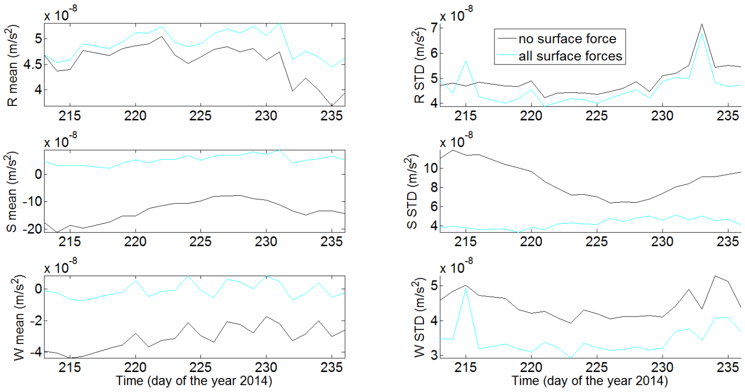

Figure 7.2: Daily mean values (left) and STD (right) of the piecewise constant accelerations for Swarm C.

7.1.3. GRACE A VALIDATION

The influence of the non-gravitational forces upon the piecewise constant accelerations in GRACE A POD is shown in Table 7.2 and in Fig. 7.3. While the inclusion of SRP reduces the offset of the PCA in the radial and the cross-track direction, it increases their amplitudes. For GRACE, $\beta_0 \cong -18°$ during day 213 decreasing down to $\beta_0 \cong -44°$ at day 236. On the other hand, the introduction of the lift force reduces both the amplitudes and the offsets. The introduction of the drag force leads to a large amplitude and offset reduction in the along-track direction. In the end, the implementation of all the forces reduces the amplitudes (-70% on R, -62% on S and -20% on W) and the offsets (-53% on R, -112% on S and -34% on W) of the PCA in each direction.

The daily mean values and STD of PCA for GRACE A shown in Fig. 7.4, reveal a particularly large reduction of the amplitudes due to the modelled non-gravitational accelerations between day 213 and day 225. As the mean values and STD in cross-track direction are not always smaller, it shows a possible imprecision of the modelled cross-track accelerations. The reduction of the mean values is clear except for days 213 to 217 in cross-track direction. Note that a dependency of the results' precision on the β_0 angle is not excluded because during the first days of August the β_0 angle was closer to zero than later.

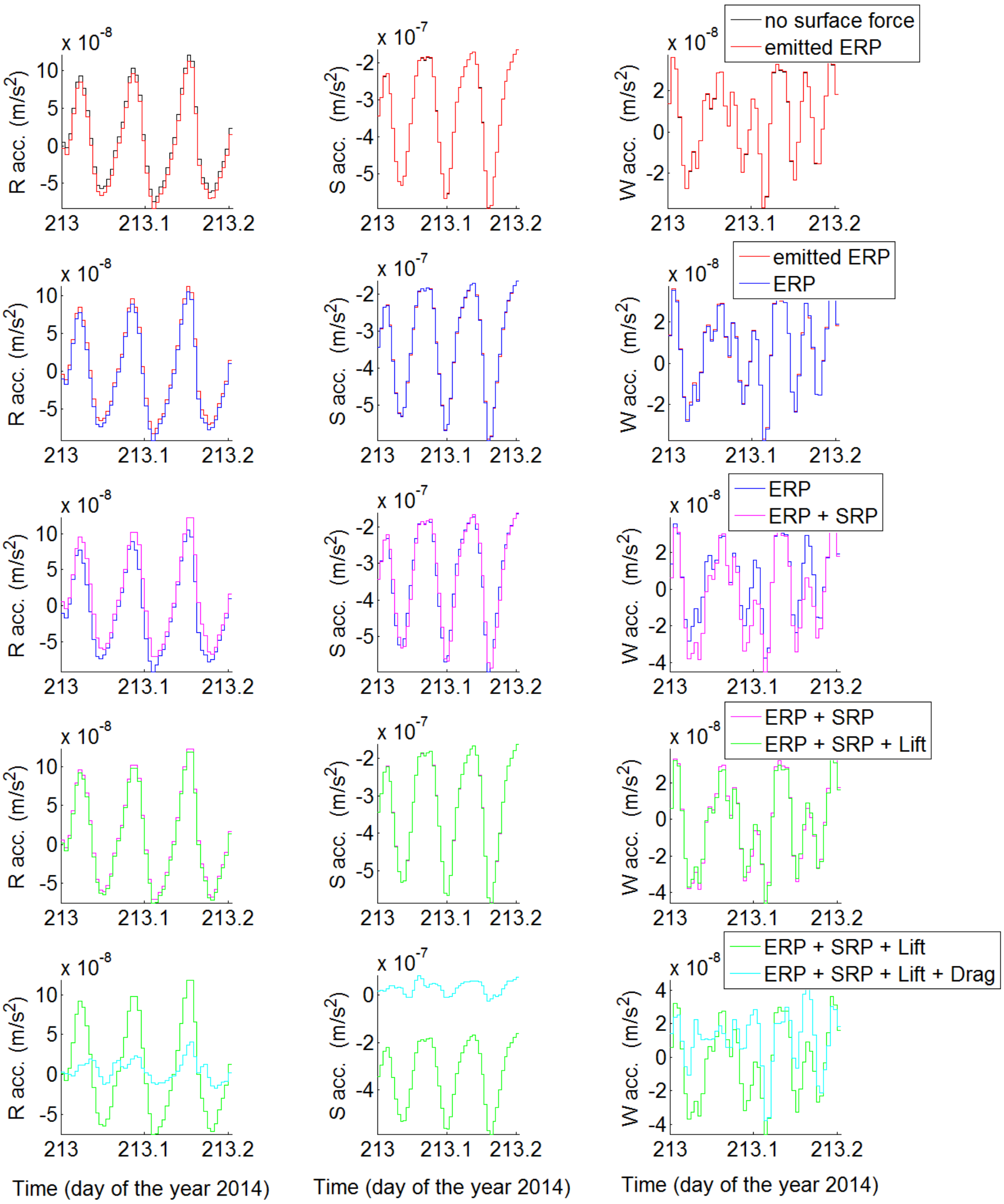

Figure 7.3: Impact of the non-gravitational forces on the piecewise constant accelerations for GRACE A when implemented one by one.

Based on the results presented in this Section, two interesting points can be discussed. First the SRP is depending on the β_0 angle, but more tests over larger periods are required to further assess the impact of the SRP. Then the impact of introducing ERP and SRP (see Tables 7.1 and 7.2) is different for Swarm and GRACE. Further investigations of the individual impact of EAR and SRP are pursued in Appendix H).

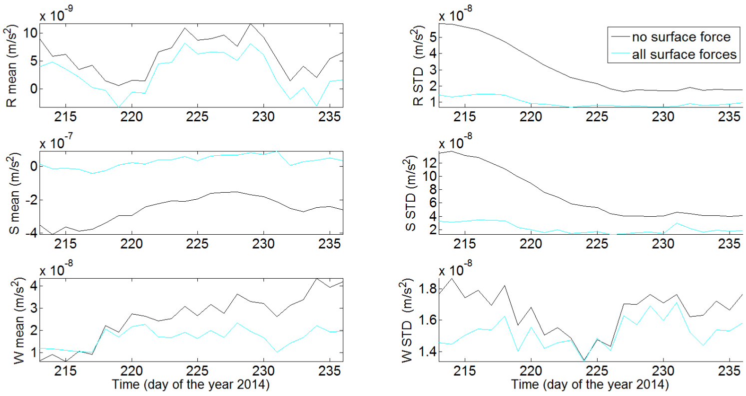

Figure 7.4: Daily mean values and STD of the piecewise constant accelerations for GRACE A.

7.2. ACCELEROMETER DATA

The implemented models are computing accelerations; therefore it is an important validation to compare them with the ones measured by the satellite's accelerometer. The comparison between the measured and modelled accelerations for GRACE A is addressed in this Section. Note that only GRACE accelerometer data is assessed, since the Swarm data is of degraded quality and no access to it was obtained[2] for this assignment.

7.2.1. GENERAL ASPECTS

The accelerometer measures the sum of non-gravitational accelerations acting on the satellite. The scale and the bias of the accelerations are not determined by the accelerometer. Therefore the measured accelerations have to be calibrated. To do so, a scale factor and a bias are estimated by fitting the measured accelerations to the modelled ones in a least squares adjustment[3]. The computed and measured accelerations have been synchronized with epochs spacing of 15 seconds[4]. The so-called "observation equation" is firstly set up, which links computed and measured values with a bias and a scaling factor (see Eq. 7.1). The least-squares adjustment gives the solution to find the bias and scale contained in $\vec{x}$ (one per orbital axis), which actually minimize the residuals. More details about the least-squares adjustment can be found in [5]. The measured accelerations are calibrated daily [82] for the 24 sample days.

$$\vec{l} = A\vec{x}, \qquad \text{where} \qquad \vec{l} = \begin{pmatrix} a_1 \\ a_2 \\ \vdots \\ a_n \end{pmatrix}, \quad A = \begin{pmatrix} 1 & z_1 \\ 1 & z_2 \\ \vdots & \vdots \\ 1 & z_n \end{pmatrix}, \quad \vec{x} = \begin{pmatrix} b \\ s \end{pmatrix} \tag{7.1}$$

$$(A^T A)\vec{x} = A^T\vec{l} \Longleftrightarrow \vec{x} = (A^T A)^{-1} \cdot (A^T\vec{l}) \tag{7.2}$$

a_i	computed accelerations
z_i	measured accelerations (by the accelerometer)
b	bias
s	scaling factor

7.2.2. GRACE A VALIDATION

Fig. 7.5 left shows the calibrated accelerations together with the computed ones. While both data match well in the radial and along-track direction, a noticeable difference appears in cross-track. Since thruster fir-

---

[2] The chosen sample days have been chosen regarding the timespans where the accelerometer data have been corrected for Swarm C [81].

[3] Note that initially the measured accelerations are in "accelerometer frame". They have been transformed into orbital frame in order to be used.

[4] Because the measured accelerations are given every second and the computed ones every 7.5 seconds.

ings are likely to create a small cross-track force [83], the data has been cleaned from thruster firing peaks[5]. However, the measured accelerations cleaned from thruster firing peaks do not lead to a better match with the modelled accelerations (see 7.5 right). Another possible cause of the discrepancy is the impact of the solar/ionosphere activity (which was unusually large in 2014 [84]), meaning the atmospheric model outputs (atmosphere density and composition) may be inaccurate because one sees the similar results with DTM2013. Inaccurate atmospheric model output could lead to a change in the aerodynamic forces. Further investigations showed that the cross-track accelerations are mostly due to the SRP and the atmospheric drag. More specifically, the SRP and the drag seem to compensate each other (see also Appendix G). If the resulting accelerations are too large, it is because one of them is too large and cannot be compensated for, or too small and is over compensated for or both of them are too large at the same time. In Fig. 7.6 the measured accelerations have been calibrated every 100 minutes instead of every day. On the left picture SRP has been scaled by 1.3, and even though the gap is reduced, a large difference remains during the eclipse which cannot be caused by SRP. On the right side the aerodynamic forces have been scaled by 0.7, which seems to give a finer match. It is important to mention that in radial and along-track direction, the rescale leads to invisible changes since the least-squares adjustment seems to well absorb the rescale (see Appendix G). Assuming that the aerodynamic forces should be 30% smaller on the cross-track axis, this could be achieved in increasing the accommodation coefficient or in using smaller solar and geomagnetic indices (those indices may be estimated inaccurately, see also Chapter 6). Moreover it is consistent with a possible poor estimation of the solar/ionosphere activity, which would also lead to scale the aerodynamic force (as shown in Appendix G, only the cross-track direction is affected by the poor least-squares adjustment even after a rescaling of the aerodynamic forces).

The attentive reader sees on Fig. 7.5 (right and left), that the modelled acceleration is a little larger before the eclipse, this small difference vanishes during the eclipse. This mismatch is probably the manifestation of the thermal emission of the satellite surface after being exposed to sunlight. Anyway, such a small accelerations is negligible for POD.

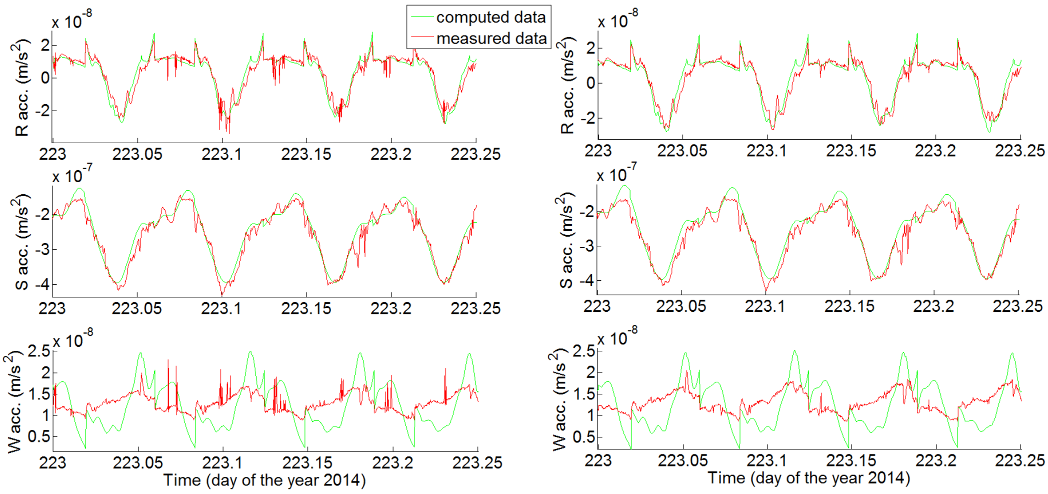

Figure 7.5: Modelled accelerations compared with calibrated measured accelerations for GRACE A with the original data (left) and with thruster firings removed (right).

---

[5] Since the thrusters are always firing for the same duration (1 millisecond), every time a thruster is firing the previous and next epoch have been removed from both the measured and the modelled data. This method is the same as in [82]. It is important to mention that the file "$THR1B\_2014-08-01\_A\_02.asc$" has been used to obtain the epochs when the thrusters are firing.

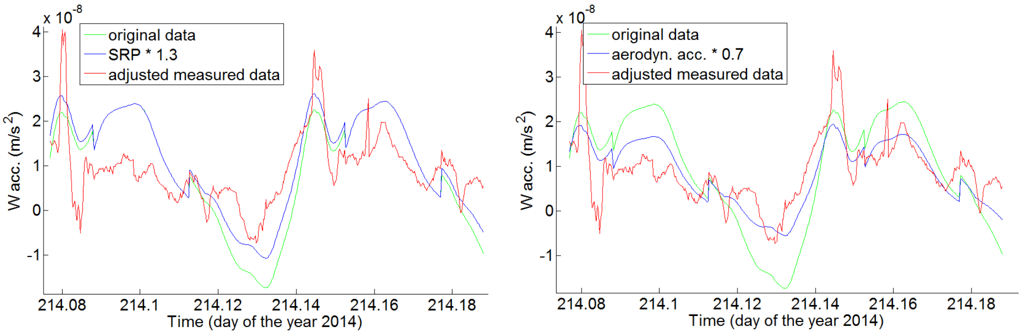

Figure 7.6: Total non-gravitational cross-track accelerations. SRP is rescaled on the left by a factor of 1.3, on the right the aerodynamic forces are rescaled by a factor of 0.7.

7.3. GPS DATA FIT

In this Section, the assessment of the GPS data fit will be twofold. First the GPS carrier phase residuals of the reduced-dynamic POD including the non-gravitational forces will be compared with the values of a POD that does not account for the surface forces. Then the PCA of the POD with no surface forces will be compared with the modelled and measured accelerations in order to evaluate how close they are to the non-gravitational forces.

7.3.1. GENERAL ASPECTS

In order to determine the reduced-dynamic orbit, the *Bernese GNSS Software* makes use of a least-squares adjustment[6] of the GPS carrier phase observations. Once the orbit is computed, the estimated a posteriori standard deviation σ of unit weight, called m_0, gives an indication about the precision of the fitting of the carrier phase observations [5].

The other aspect of the GPS data fit that is evaluated in this Section is to visually, and numerically, see how well the PCA of the reduced-dynamic POD matches with the measured and/or modelled accelerations (for Swarm, the measured accelerations are not available). It is the "same" accelerations[7] that have been obtained by three different methods, thus providing a very interesting opportunity to compare them. First, the implemented models allow computing of the non-conservative forces along an orbit. Secondly when the non-gravitational forces are not implemented, the *Bernese GNSS Software* may be used to estimate PCA that compensate mismodelled forces acting on the satellite. Finally, the accelerometer is measuring the non-gravitational forces acting upon the satellite.

7.3.2. *A posteriori* σ OF UNIT WEIGHT

Figures 7.7 and 7.8 show the daily m_0 for the Swarm C and GRACE A POD respectively. Table 7.3 gives the mean values of the m_0 computed over the available 24 sample days, respectively 23 for Swarm. The results for Swarm are as expected, an almost negligible 2% reduction. Indeed the PCA are assumed to absorb the non-gravitational forces, therefore it was not expected to see an improvement of the reduced-dynamic orbit. However, since the implemented models capture variations in the non-gravitational accelerations that are shorter than the spacing of the PCA, one may have an improvement. Furthermore, using the models allows to tighten the constraints of the PCA and to "stabilize" the orbits. On the other hand, the improvement of GRACE reduced-dynamic orbit is so large (close to 40% smaller), that it revealed an orbit parameterization issue. During Summer 2014 GRACE A was flying significantly lower than in earlier years when the chosen parameterization was well fitting. The lower altitude implies larger aerodynamic forces. Since the atmospheric drag acting on GRACE A was large in 2014, the *a priori* orbit was of poor quality then the way m_0 is computed in the *Bernese GNSS Software* becomes inaccurate. Further investigating the POD parameterization is not in the scope of this assignment, and the orbit that uses the modelled surface forces seems insensitive to this setting issue since better a priori orbits result.

---

[6] It is basically the same procedure that was described in Sec. 7.2 with a linearization prior to the least-squares adjustment.

[7] Of course PCA are always different from continuously modelled ones, but they should show a coherent behaviour.

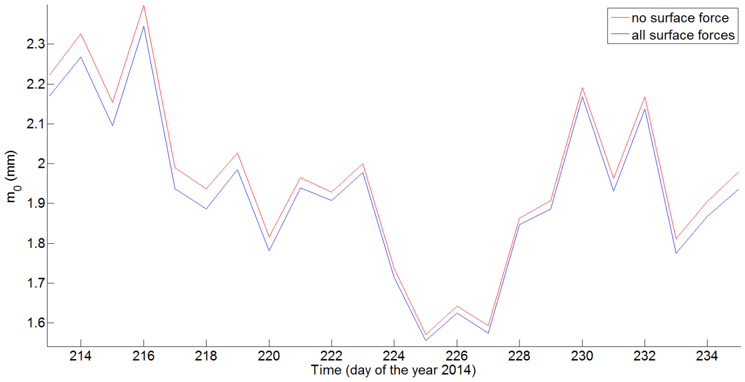

Figure 7.7: Daily m_0 of Swarm's reduced-dynamic POD.

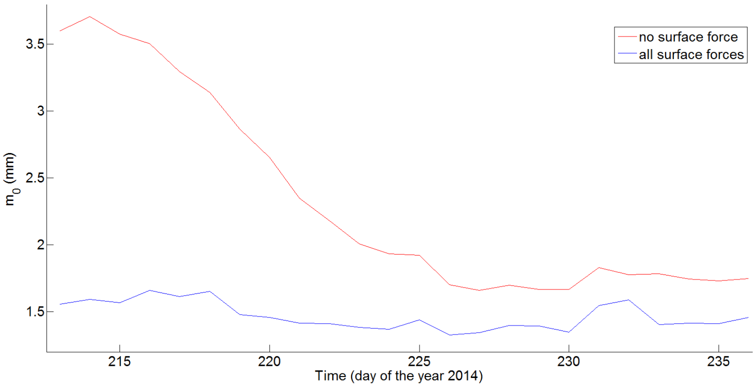

Figure 7.8: Daily m_0 of GRACE's reduced-dynamic POD.

Setting	Swarm mean value (mm)	GRACE mean value (mm)
No surface force	1.961	2.322
All surface forces	1.927	1.467

Table 7.3: Mean m_0 of the reduced-dynamic POD of Swarm C and GRACE A

7.3.3. ASSESSMENT OF THE PCA AND MODELLED ACCELERATIONS FOR SWARM C

In order to give an impression to the reader, three days will be shown: 215, 226 and 235 (see Figures 7.9). The PCA are from the reduced-dynamic POD with no surface force implemented.

Figures 7.9 a obviously strengthen the results shown in Sec. 7.1, but with a better view of the mismatch. During the day 215, one sees that the modelled accelerations on the radial axis seems to suffer from a small offset, along the other axis the modelled accelerations are consistent with the PCA, both in terms of mean value and amplitude. Day 226 shows an even larger offset in the radial direction and a more visible amplitude mismatch in along-track. Day 235 shows a similar trend as day 215 with also an offset on the radial axis. All the points raised are also visible in Fig. 7.2: a larger offset in Fig. 7.9 *a* implies a smaller gap of the mean value in Fig. 7.2 and a large amplitude difference in Fig. 7.9 *a* implies a smaller gap of the standard deviation in Fig. 7.2. In Fig. 7.9 b, the remaining PCA have been added to the modelled accelerations and a close match is visible in the three axes and at the three days. Note that the remaining differences are probably due to time interval differences between the modelled accelerations and the PCA[8]. Table 7.4 details the mean value and the standard deviation of the differences between the various plots of Fig. 7.9.

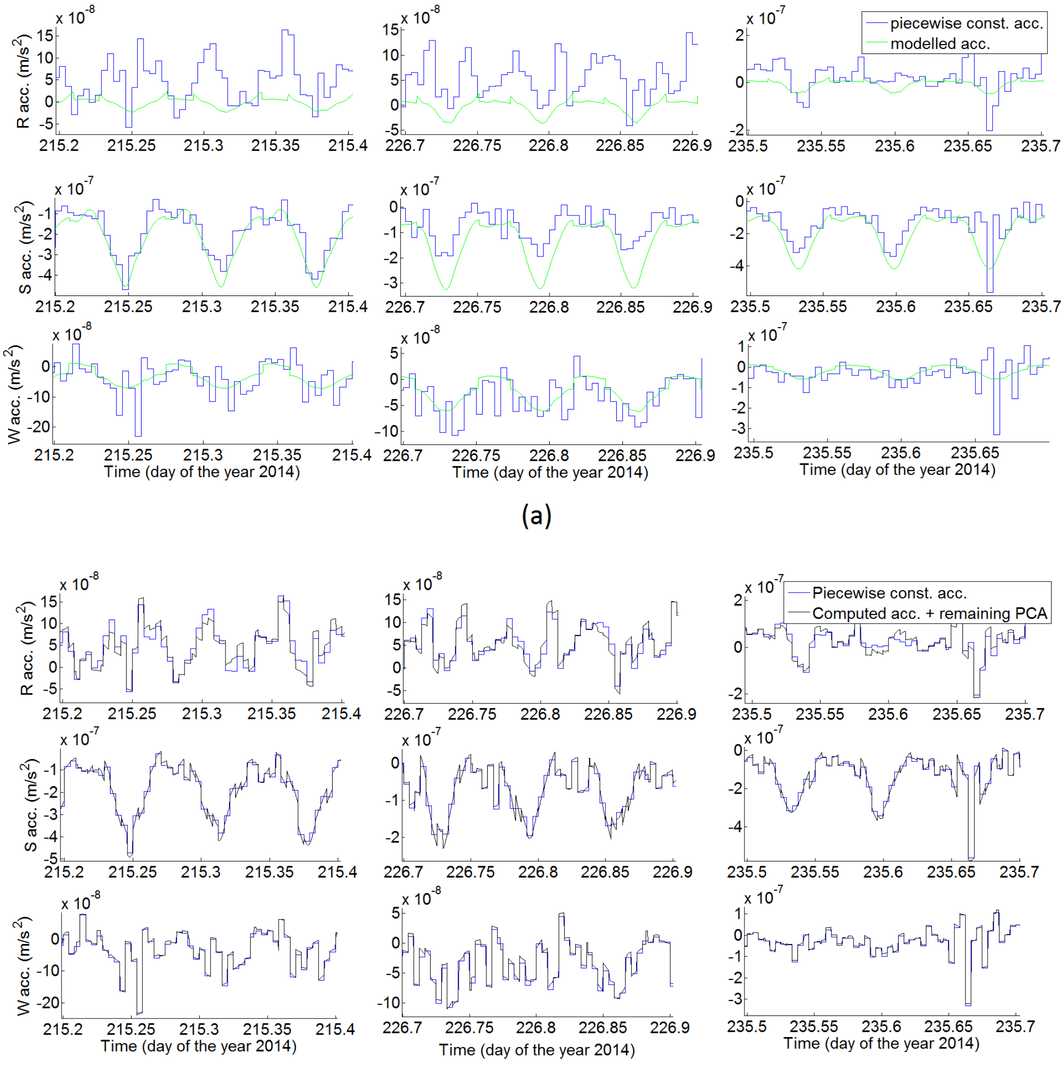

(a)

(b)

Figure 7.9: (a) Piecewise constant accelerations against modelled accelerations for Swarm C. (b) Piecewise constant accelerations against modelled accelerations added to the remaining PCA when the surface forces are modelled.

---

[8] The next step to compare them could be to estimate a mean value of the modelled accelerations between the PCA time intervals

	Mean (m/s^2)			**STD** (m/s^2)		
Setting	**Radial**	**Along-track**	**Cross-track**	**Radial**	**Along-track**	**Cross-track**
No surface force PCA	4.55E-08	-1.32E-07	-3.04E-08	4.96E-08	9.69E-08	4.51E-08
No surface force PCA - modelled acc.	4.94E-08	4.58E-08	-5.63E-09	4.53E-08	6.41E-08	3.56E-08
No surface force PCA - modelled acc. - remaining PCA	-1.30E-10	-7.58E-09	-4.88E-09	1.72E-08	4.03E-08	9.12E-09

Table 7.4: Statistics for Swarm C. First of the PCA with no surface forces modelled. Second of the difference between the PCA and the modelled accelerations. Finally, of the difference between the PCA and the modelled accelerations added to the remaining PCA.

	Mean (m/s^2)			**STD** (m/s^2)		
Setting	**Radial**	**Along-track**	**Cross-track**	**Radial**	**Along-track**	**Cross-track**
No surface force PCA	5.83E-09	-2.58E-07	2.58E-08	3.44E-08	1.11E-07	1.97E-08
No surface force PCA - modelled acc.	1.73E-09	3.14E-08	1.16E-08	3.65E-08	4.71E-08	1.71E-08
No surface force PCA - modelled acc. - remaining PCA	-1.03E-09	1.89E-10	-5.22E-09	3.08E-08	2.69E-08	5.48E-09

Table 7.5: Statistics for GRACE A. First of the PCA with no surface forces modelled. Second of the difference between the PCA and the modelled accelerations. Finally, of the difference between the PCA and the modelled accelerations added to the remaining PCA.

7.3.4. ASSESSMENT OF THE PCA, MODELLED AND MEASURED ACCELERATIONS FOR GRACE A

Similarly to previous section, three days will be shown. Here the adjusted measured accelerations are also shown in Fig. 7.10. Table 7.5 details the mean value and the standard deviation of the differences between the various plots of Fig. 7.10. They have been calibrated daily, the data has been previously cleaned from thruster firing peaks (as described in Sec. 7.2).

For GRACE A, Fig. 7.10 b shows on the radial axis of the day 215 that the PCA are absorbing more than the computed non-gravitational forces because a mismatch remains between the black and the blue lines (this proves that the POD has an issue). So this highlights the setting issue mentioned in the beginning of this Section. Table 7.5 shows that the along-track and cross-track directions are not influenced by this issue because the differences become very small when the remaining PCA are subtracted. Another interesting feature is that a scale difference between the PCA and the along-track modelled accelerations are visible on both Figures 7.9 *a* and 7.10 *a*. During the day 215, a rescale of the modelled accelerations in along-track should reduce the gap with the PCA. This important point underlines the motivation to introduce a scaling factor to the modelled accelerations. This would involve to again modify part of the implementation and to make more tests. Unfortunately, such additional investigations do not fit in the schedule of this assignment, but can motivate further developments.

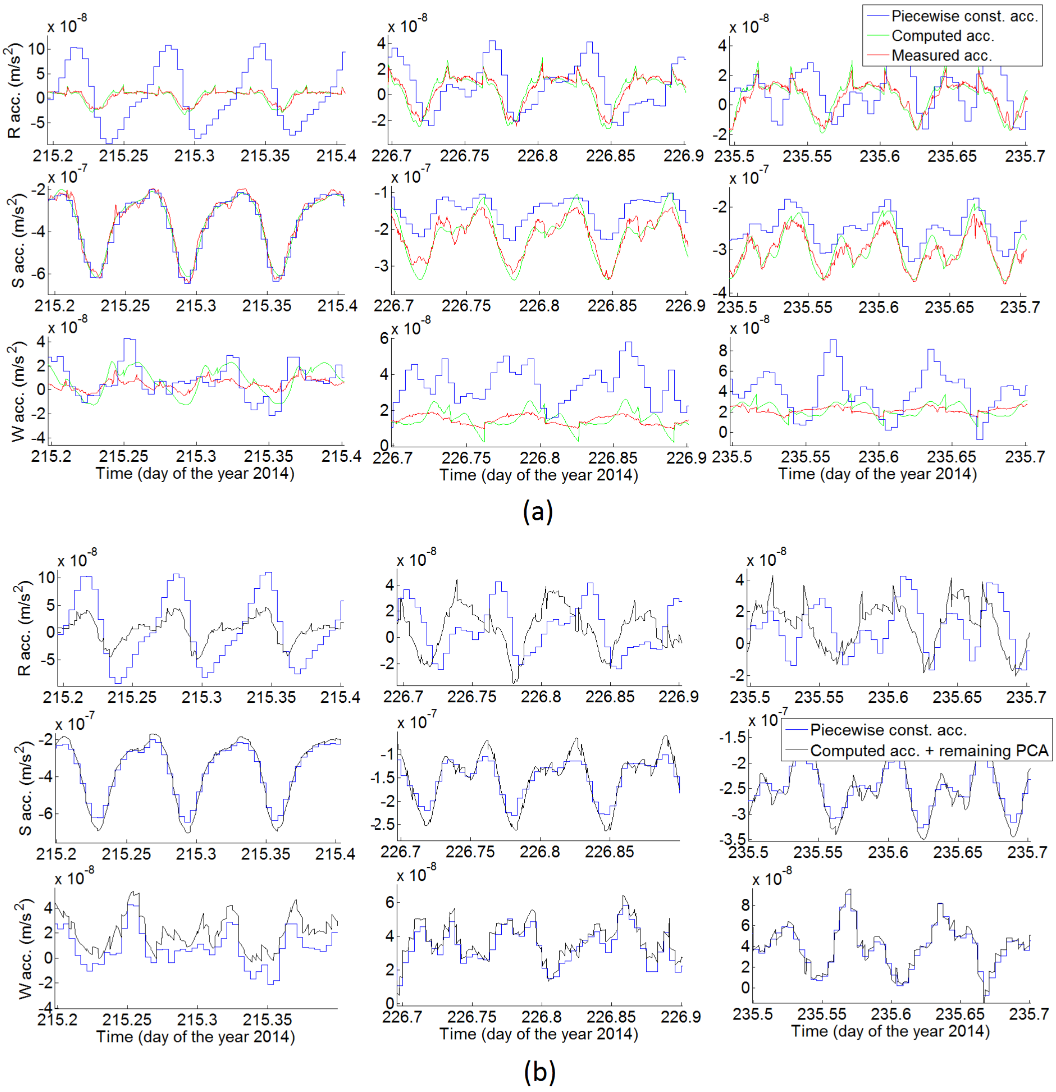

Figure 7.10: (a) Piecewise constant accelerations against modelled and measured accelerations for GRACE A. (b) Piecewise constant accelerations against modelled accelerations added to the remaining PCA when the surface forces are modelled.

7.4. SATELLITE LASER RANGING

In this Section, the orbits using the implemented non-gravitational forces are validated with the SLR observations. SLR provides an external validation method, so the results presented in this Section confirm the orbital improvement due to the modelled surface forces.

7.4.1. GENERAL ASPECTS

Satellite laser ranging measures the durations of emitted laser pulses reflected back by the satellite to the emission source (always a ground station). It provides an independent technique to determine the absolute range between the satellite and the tracking station with no active satellite communication. Moreover, it is essentially free from systematic errors such as ionospheric and tropospheric delays or phase ambiguities [54].

Based on a GPS-based orbit, the standard deviation and mean value of the differences between the computed and the measured range are calculated using the *Bernese GNSS Software*. In order to maintain an acceptable accuracy, the standard deviation and mean values have been computed over the entire timespan, and with an outlier threshold of 40 mm.

Setting	Mean SLR residuals (mm)	STD of SLR residuals (mm)	Observations	Min. value (mm)	Max. value (mm)
No surface force	7.73	19.13	1153	-39.9	40.0
All surface forces	7.74	18.62	1157	-39.6	40.0

Table 7.6: SLR validation for Swarm C.

Setting	Mean SLR residuals (mm)	STD of SLR residuals (mm)	Observations	Min. value (mm)	Max. value (mm)
No surface force	-2.22	19.39	1921	-40.0	39.5
All surface forces	-1.17	17.99	2041	-40.0	39.9

Table 7.7: SLR validation for GRACE A.

7.4.2. SWARM C AND GRACE A EXTERNAL VALIDATION

Tables 7.6 for Swarm C and 7.7 for GRACE A show that the mean SLR residuals are almost not influenced by the modelled accelerations. SLR provides information mainly in the radial direction, which is consistent with the results of the PCA validation of Fig. 7.2 (see Sec. 7.1), which were slightly increased by the surface forces. The implementation of the surface forces slightly increased the mean SLR residuals. But the standard deviation is reduced by 2.7% for Swarm C. On the other hand, Table 7.7 depicts for GRACE A a larger standard deviation reduction of 7.2%. For GRACE A, the mean value of the SLR residuals is clearly reduced with the surface forces modelling (which is consistent with the radial mean PCA reduction, see Fig. 7.4). One can also say that the screening constraint of +/- 4 cm might be too tight (because the smallest and largest value are equal or close to this limit), event though the number of observations is acceptable.

This SLR validation confirms what has been observed with the PCA and the *a posteriori* σ of unit weight: the modelled non-conservative forces are more beneficial for GRACE A than for Swarm C. The most probable reason is the lower altitude of GRACE A when compared to Swarm C (GRACE A was at 426 km and Swarm C 474 km). The lower the satellite, the larger the impact of the aerodynamic forces. In addition, the revealed setting issue (discussed in Sec. 7.3) may also contribute to this large improvement.

7.5. K/Ka-BAND RANGING

The KBR validation of the GRACE A & B orbits are presented in this Section. It is a reliable external validation method, which is mostly directed in the along-track direction. The KBR validation was conducted with the *Bernese GNSS Software.*

7.5.1. GENERAL ASPECTS

$K/Ka-$Band Ranging observes the phase variation of the microwave signal to measure the distance between GRACE A & B to the micron level. The validation process involving KBR is twofold. First, the orbit must be generated for both GRACE A & B, so the reduced-dynamic orbits of GRACE A and B are determined separately. Then the differences between the computed and the measured inter-satellite ranges and range-rates yield the K/Ka-band residuals. Their mean value and standard deviation are a very precise measure for the relative orbit accuracy. The advantage of such a precise satellite-to-satellite validation method is its negligible noise when compared with the orbit errors [5]. Moreover, the $K/Ka-$Band signal is mostly directed in the along-track direction, so is the atmospheric drag (largest implemented surface force).

The tests have been carried out with both GRACE A & B, based on a 30 seconds sampling over the 24 sample days. The analysis of the results is twofold, first the daily result for the range and range-rate residuals are presented. Then the daily values are averaged over the 24 sample days.

7.5.2. GRACE A & B K-BAND VALIDATION

Fig. 7.11 shows the daily mean range and range-rate, as well as the daily standard deviation of the range and range-rate residuals. The mean values of the orbits modelled with the non-conservative forces are less varying from one day to another. The STD of both the range residuals and the range-rate residuals show that even though they are globally smaller when the surface forces are modelled, they may be larger some days. It will be shown in Chapter 8 that parameterization of the aerodynamic forces modelling may further reduce

Setting	Mean range residuals (mm)	STD of the range residuals (mm)	Mean range-rate residuals (μm/s)	STD of the range-rate residuals (μm/s)
No surface force	1.91-07	7.64	0.02	10.04
All surface forces	-1.67E-07	6.65	0.09	7.75

Table 7.8: KBR validation for GRACE

the STD of the residuals. Table 7.8 gives the indications values, but computed over the entire timespan of 24 days.

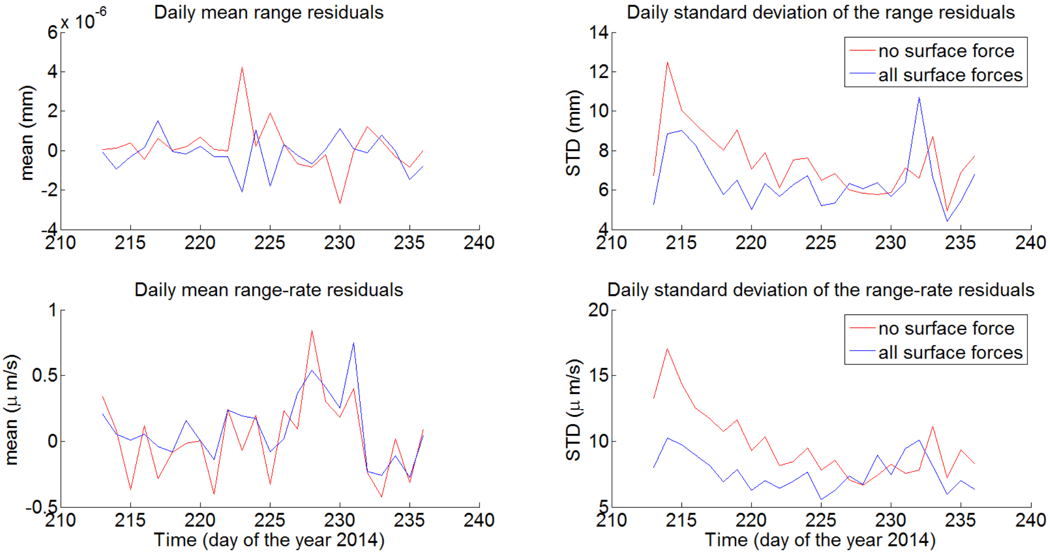

Figure 7.11: Daily results of the KBR validation for GRACE A and B: mean range residuals (top left), standard deviation of the range residuals (top right), mean range-rate residuals (bottom left) and standard deviation of the range-rate residuals (bottom right).

8

PARAMETERIZATION TESTS

In this Chapter, the orbits based on different parameterizations for the computation of the aerodynamic forces are compared. More specifically we have seen in Chapter 6 that the atmospheric model, the horizontal wind model and the choice of the method to compute the accommodation coefficient lead to noticeable differences. Here, their influence on POD is assessed in order to find which parameterization leads to the largest POD improvement.

The four different equations of Sec. 6.1 to calculate the accommodation coefficient will be tested. More specifically, two equations based on Goodman's method with different coefficients $f = 3.6$ and $f = 2.4$, and two equations based on Pilinski's method with $K = 5.0 \times 10^{-17}$and $K = 7.5 \times 10^{-17}$ (see also Sec. 3.2.3). The four cases will be tested with NRLMSISE-00 and DTM2013 atmospheric models. As the DTM2013 model is more recent, one expects to have better results with this model, but the NRLMSIS series has been the standard for decades, so it is not possible so far to select a favourite. Finally, the 8 cases will be tested with, and without, the horizontal wind model HWM14 for a total of 16 different parameterizations. They will all be applied on GRACE A, GRACE B (otherwise K/Ka-band validation is not possible) and Swarm C for a total of 48 tests. The tests are performed on a sample of 24 days, from 01.08.2014 to 24.08.2014 (same sample days as in Chapters 6 and 7). The tests have been carried out with the same validation methods as in the previous Chapter. For the sake of simplicity, only numerical values are given (no plots) and only the results on the along-track are given (the results along other axes are shown in Appendix I) for the PCA and accelerometer measurements. In addition, the lowest value of each table will be highlighted. Note that the results for GRACE B have been verified to be similar to GRACE A, therefore only results of GRACE A will be detailed.

8.1. PARAMETERIZATION FOR SWARM

Tables 8.1 and 8.2 detail the mean value and the standard deviation of the PCA on the along-track orbital axis. The list below summarizes the relevant observations for those two Tables.

- Atmospheric model: DTM2013 shows a larger reduction of both the mean and STD of the PCA.

- Wind model: HWM14 is always reducing the mean values and STD of the PCA.

- Accommodation coefficient: while Goodman's method with $f = 3.6$ gives the best results, it also gives the worst ones when $f = 2.4$. On the other hand, Pilinski's method with $K = 7.5 \times 10^{-17}$ shows lower mean and STD than $K = 5.0 \times 10^{-17}$.

	No wind model		**HWM14**	
Accommodation coefficient	**NRLMSISE-00**	**DTM2013**	**NRLMSISE-00**	**DTM2013**
Goodman, $f = 2.4$	7.55E-08	5.80E-08	7.52E-08	5.76E-08
Goodman, $f = 3.6$	5.41E-08	3.85E-08	5.38E-08	**3.82E-08**
Pilinski, $K = 5.0$ E-17	7.66E-08	5.97E-08	7.63E-08	5.93E-08
Pilinski, $K = 7.5$ E-17	7.16E-08	5.52E-08	7.13E-08	5.48E-08

Table 8.1: Mean piecewise constant accelerations on the along-track axis for various parameterizations for Swarm C, in m/s^2. Value with no surface force: -1.32E-07 m/s^2.

	No wind model		**HWM14**	
Accommodation coefficient	**NRLMSISE-00**	**DTM2013**	**NRLMSISE-00**	**DTM2013**
Goodman, $f = 2.4$	5.21E-08	4.89E-08	5.19E-08	4.85E-08
Goodman, $f = 3.6$	4.65E-08	4.29E-08	4.63E-08	**4.25E-08**
Pilinski, $K = 5.0$ E-17	4.92E-08	4.60E-08	4.90E-08	4.55E-08
Pilinski, $K = 7.5$ E-17	4.78E-08	4.45E-08	4.76E-08	4.41E-08

Table 8.2: Standard deviation of the PCA on the along-track axis for Swarm, in m/s^2. Value with no surface force: 9.69E-08 m/s^2.

Table 8.3 gives the mean values of the daily standard deviations of unit weight m_0. Interestingly, the exact same trend as for the PCA is visible: the best result is given when using DTM2013 with HWM14 and Goodman's method with $f = 3.6$. Note, however, that the differences are very small.

Table 8.4 shows the mean SLR residuals and Table. 8.5 the standard deviations of the SLR residuals. The list below summarizes the important points for those two Tables.

- Atmospheric model: most of the tests show smaller mean and STD when the NRLMSISE-00 model is used.

- Wind model: the influence of the HWM14 depends on the method used to compute the accommodation coefficient. The smallest STD are obtained without using the wind model.

- Accommodation coefficient: the results depends on the atmospheric model used. When the DTM2013 is used, Pilinski's method yields smaller values, but Goodman's method gives the smallest values with the NRLMSISE-00.

	No wind model		**HWM14**	
Accommodation coefficient	**NRLMSISE-00**	**DTM2013**	**NRLMSISE-00**	**DTM2013**
Goodman, $f = 2.4$	1.929	1.928	1.929	1.928
Goodman, $f = 3.6$	1.927	1.925	1.927	**1.925**
Pilinski, $K = 5.0$ E-17	1.928	1.927	1.928	1.927
Pilinski, $K = 7.5$ E-17	1.927	1.926	1.927	1.926

Table 8.3: Mean value of the daily estimated standard deviation of unit weight m_0 for Swarm, in mm. Value with no surface force: 1.961 mm.

	No wind model		HWM14	
Accommodation coefficient	**NRLMSISE-00**	**DTM2013**	**NRLMSISE-00**	**DTM2013**
Goodman, $f = 2.4$	**7.66**	7.68	7.68	7.78
Goodman, $f = 3.6$	7.69	7.74	7.80	7.78
Pilinski, $K = 5.0$ E-17	7.71	7.69	7.75	7.71
Pilinski, $K = 7.5$ E-17	7.71	7.74	7.75	7.76

Table 8.4: Mean offset of the SLR residuals of Swarm, in mm. The residuals have been screen with ±40 mm. Value with no surface force: 7.73 mm.

	No wind model		HWM14	
Accommodation coefficient	**NRLMSISE-00**	**DTM2013**	**NRLMSISE-00**	**DTM2013**
Goodman, $f = 2.4$	18.50	18.53	18.52	18.59
Goodman, $f = 3.6$	**18.49**	18.60	18.57	18.77
Pilinski, $K = 5.0$ E-17	18.57	18.52	18.52	18.54
Pilinski, $K = 7.5$ E-17	18.52	18.62	18.50	18.60

Table 8.5: STD of the SLR residuals of Swarm, in mm. The residuals have been screen with ±40 mm. Value with no surface force: 19.13 mm

8.2. PARAMETERIZATION FOR GRACE

Similarly to Swarm C, Tables 8.6 and 8.7 detail the mean values and the standard deviations of the PCA of the GRACE A POD in the along-track direction. Their results are listed below.

- Atmospheric model: the DTM2013 shows a larger reduction of both the mean values and STD of the PCA.
- Wind model: HWM14 gives smaller STD when DTM2013 is used, but not when NRLMSISE-00 is used. Except for the best result, the HWM14 model is always reducing the STD of the PCA.
- Accommodation coefficient: Goodman's method with $f = 3.6$ gives the smallest mean value and the smallest standard deviation.

Table 8.8 depicts the standard deviations of the acceleration differences between the modelled and (calibrated) measured ones. Since the measured accelerations have been calibrated daily, the mean values are extremely close to zero, thus irrelevant. Only the results in the along-track direction are shown (see Appendix I for results along the radial and cross-track directions). The list below summarizes the relevant points of the Table.

- Atmospheric model: NRLMSISE-00 gives a smaller standard deviation of the acceleration differences.
- Wind model: the use of HWM14 does not seem to be beneficial for NRLMSISE-00.
- Accommodation coefficient: Pilinski's method with $K = 7.5 \times 10^{-17}$ yields the smallest acceleration differences, closely followed by Goodman's method with $f = 3.6$.

Table 8.9 gives the mean values of the daily standard deviations of unit weight m_0. The list below assesses the impact of the atmospheric model, wind model and algorithm to compute α.

	No wind model		HWM14	
Accommodation coefficient	**NRLMSISE-00**	**DTM2013**	**NRLMSISE-00**	**DTM2013**
Goodman, $f = 2.4$	6.28E-08	3.30E-08	6.18E-08	3.20E-08
Goodman, $f = 3.6$	3.21E-08	**5.34E-09**	3.12E-08	3.20E-08
Pilinski, $K = 5.0$ E-17	5.52E-08	2.77E-08	5.43E-08	2.67E-08
Pilinski, $K = 7.5$ E-17	4.79E-08	2.11E-08	4.70E-08	2.01E-08

Table 8.6: Mean PCA in the along-track for GRACE A, in m/s^2. Value with no surface force: -2.58E-07 m/s^2.

	No wind model		HWM14	
Accommodation coefficient	**NRLMSISE-00**	**DTM2013**	**NRLMSISE-00**	**DTM2013**
Goodman, $f = 2.4$	3.82E-08	2.89E-08	3.83E-08	**2.80E-08**
Goodman, $f = 3.6$	4.19E-08	2.91E-08	4.22E-08	**2.80E-08**
Pilinski, $K = 5.0$ E-17	4.21E-08	2.92E-08	4.24E-08	2.87E-08
Pilinski, $K = 7.5$ E-17	4.30E-08	2.97E-08	4.33E-08	2.93E-08

Table 8.7: Standard deviations of the PCA in along-track for GRACE A, in m/s^2. Value with no surface force: 1.11E-07 m/s^2.

	No wind model		HWM14	
Accommodation coefficient	**NRLMSISE-00**	**DTM2013**	**NRLMSISE-00**	**DTM2013**
Goodman, $f = 2.4$	2.78E-08	3.14E-08	2.79E-08	3.01E-08
Goodman, $f = 3.6$	2.51E-08	2.82E-08	2.54E-08	3.01E-08
Pilinski, $K = 5.0$ E-17	2.55E-08	2.89E-08	2.58E-08	2.77E-08
Pilinski, $K = 7.5$ E-17	**2.49E-08**	2.81E-08	2.53E-08	2.70E-08

Table 8.8: Standard deviation of the acceleration differences between the modelled and (daily calibrated) measured accelerations on the along-track axis of GRACE A. The unit of the acceleration differences is m/s^2.

- Atmospheric model: DTM2013 leads to smaller values of m_0 for all the tests.
- Wind model: while the orbits based on NRLMSISE-00 are not sensitive to HWM14, it has a beneficial impact on the orbit fit when DTM2013 is used.
- Accommodation coefficient: for the first time in this Section, the two algorithms using the Pilinski's method to compute the accommodation coefficient yield the smallest values.

Tables 8.10 and 8.11 show the mean SLR residuals and the standard deviations of the SLR residuals. The list below outlines the relevant points.

- Atmospheric model: most of the tests show smaller STD when the DTM2013 model is used, except the most precise results. On the other hand, the NRLMSISE-00 model yields a mean offset closer to zero.
- Wind model: HWM14 enlarges the mean SLR residuals. It is difficult to make a general statement about the horizontal wind model's influence on the STD.
- Accommodation coefficient: the results depend on the atmospheric model used. When the DTM2013 is used, Pilinski's method yields smaller values, but Goodman's method gives the smallest values with NRLMSISE-00.

	No wind model		HWM14	
Accommodation coefficient	**NRLMSISE-00**	**DTM2013**	**NRLMSISE-00**	**DTM2013**
Goodman, $f = 2.4$	1.456	1.465	1.452	1.450
Goodman, $f = 3.6$	1.467	1.451	1.467	1.450
Pilinski, $K = 5.0$ E-17	1.472	1.456	1.472	**1.445**
Pilinski, $K = 7.5$ E-17	1.476	1.455	1.477	1.446

Table 8.9: Mean values of the daily standard deviations of unit weight m_0 for GRACE A, in mm. Value with no surface force: 2.322 mm

	No wind model		**HWM14**	
Accommodation coefficient	**NRLMSISE-00**	**DTM2013**	**NRLMSISE-00**	**DTM2013**
Goodman, $f = 2.4$	**-0.95**	-1.09	-1.07	-1.31
Goodman, $f = 3.6$	-1.06	-1.18	-1.17	-1.31
Pilinski, $K = 5.0$ E-17	-1.04	-1.20	-1.19	-1.26
Pilinski, $K = 7.5$ E-17	-1.05	-1.20	-1.15	-1.28

Table 8.10: Mean SLR residuals for GRACE A, in mm. Value with no surface force: -2.22 mm.

	No wind model		**HWM14**	
Accommodation coefficient	**NRLMSISE-00**	**DTM2013**	**NRLMSISE-00**	**DTM2013**
Goodman, $f = 2.4$	**17.79**	17.93	17.87	17.92
Goodman, $f = 3.6$	17.93	17.91	17.99	17.92
Pilinski, $K = 5.0$ E-17	17.97	17.92	18.10	17.89
Pilinski, $K = 7.5$ E-17	17.98	17.90	18.02	17.89

Table 8.11: STD of the SLR residuals for GRACE A, in mm. Value with no surface force: 19.39 mm.

Tables 8.12 and 8.13 present the STD of the range and the range-rate K-band residuals for GRACE A & B. The list below outlines the relevant points of the different parameterizations, validated with KBR. The results of both Tables are mostly consistent.

- Atmospheric model: when DTM2013 is used, the STD of the range residuals are is always smaller. DTM2013 gives smaller values for the STD of the range-rate residuals when used with the horizontal wind model.
- Wind model: the effect of the HWM14 is beneficial for all the cases using DTM2013. It is mostly the opposite with NRLMSISE-00.
- Accommodation coefficient: Goodman's method gives the smallest STD of the range residuals. On the other hand, it is difficult to derive a trend based on the results of the STD of the range-rate residuals.

	No wind model		**HWM14**	
Accommodation coefficient	**NRLMSISE-00**	**DTM2013**	**NRLMSISE-00**	**DTM2013**
Goodman, $f = 2.4$	6.71	6.56	6.64	**6.52**
Goodman, $f = 3.6$	6.62	6.59	6.65	**6.52**
Pilinski, $K = 5.0$ E-17	6.65	6.59	6.64	6.56
Pilinski, $K = 7.5$ E-17	6.75	6.60	6.64	6.55

Table 8.12: STD of the K-band range residuals for GRACE, in mm. Value with no surface force: 7.64 mm.

	No wind model		HWM14	
Accommodation coefficient	**NRLMSISE-00**	**DTM2013**	**NRLMSISE-00**	**DTM2013**
Goodman, $f = 2.4$	**6.10**	7.55	7.76	7.51
Goodman, $f = 3.6$	7.71	7.59	7.75	7.51
Pilinski, $K = 5.0$ E-17	7.75	7.62	7.74	7.56
Pilinski, $K = 7.5$ E-17	6.17	7.61	7.73	7.54

Table 8.13: STD of the K-band range-rate residuals for GRACE, in μm/s. Value with no surface force: 10.04 μm/s.

Validation method	**LEO**	**Mean of**	**NRLMSISE -00**	**DTM 2013**	**HWM 14**	$\alpha_{G,1}$	$\alpha_{G,2}$	$\alpha_{P,1}$	$\alpha_{P,2}$
PCA	Swarm C	along-track PCA		X	X		X		
PCA	GRACE A	along-track PCA		X			X		
GPS data fit	Swarm C	daily m_0		X	X		X		
GPS data fit	GRACE A	daily m_0		X	X			X	
SLR	Swarm C	SLR residuals	X			X			
SLR	GRACE A	SLR residuals	X			X			

Table 8.14: Summary of the best results shown in this Section, **based on mean values**.

8.3. BEST PARAMETERIZATION

Depending on the validation method used, the best setting is not always the same. Therefore Tables 8.14 and 8.15 review the best results shown in this Section. While Table 8.14 summarizes the settings leading to the smallest mean values, Table 8.15 outlines the parameterizations yielding the smallest standard deviations of the quality metrics presented in this Section. A capital "X" indicates that the parameterization is better than all the other with no ambiguity, otherwise an "x" indicates the two parameterizations that gave the smallest value.

Interestingly, DTM2013 seems to give generally smaller values, except for the SLR observations, accelerometer and KBR range-rate residuals. The use of the horizontal wind model HWM14 seems to improve the results for DTM2013 only. Anyway, since HWM14 is supposed to have a beneficial influence in the along-track and cross-track directions, it is not surprising that SLR do not show improvements with HWM14. Pilinski's method to compute the accommodation coefficient seems less appropriate than Goodman's method. Moreover, the use of $f = 3.6$ gives the best results in most of the cases.

Validation method	**LEO**	**STD of**	**NRLMSISE -00**	**DTM 2013**	**HWM 14**	$\alpha_{G,1}$	$\alpha_{G,2}$	$\alpha_{P,1}$	$\alpha_{P,2}$
Measured acc.	GRACE A	along-track acc. diff.	X						X
PCA	Swarm C	along-track PCA		X	X		X		
PCA	GRACE A	along-track PCA		X	X	x	x		
SLR	Swarm C	SLR residuals	X				X		
SLR	GRACE A	SLR residuals	X			X			
KBR	GRACE A	range residuals		X	X	x	x		
KBR	GRACE A	range-rate residuals	X			X			

Table 8.15: Summary of the best results shown in this Section, **based on standard deviations**.

9

CONCLUSION & DISCUSSION

9.1. CONCLUSION

In this project four non-conservative forces acting on LEOs have been implemented into the *Bernese GNSS Software*: aerodynamic forces (atmospheric lift and drag), the solar radiation pressure and emitted and reflected Earth radiation pressure. In order to compute those forces, modelling the Earth TOA and satellite surface are needed. While the latter have been constructed as macro-models of the Swarm and GRACE satellites, gridded values of monthly mean albedo and emissivity have been used based on the CERES observations data. The statistics of all the tests and validations are based on a sample of 24 days during Summer 2014[1]. It is important to mention that the force coefficients are modelled, i.e. C_D, C_L and $\vec{C}_r$ are computed.

For Swarm C the modelled accelerations have been individually compared with external data provided by E. Doornbos (TU Delft). This intercomparison showed the consistency of the modelled accelerations and their sensitivity to the setting changes. For the aerodynamic forces the atmospheric model, the method to compute the density[2] and the algorithm to compute the accommodation coefficient influence the amplitude of the modelled accelerations. For the other forces, varying the optical properties of the macro-models also leads to amplitude variations and even a bias in the radial direction. The bias is mostly due the ERP, which is mainly acting in radial direction. In general, the modelled and external accelerations are consistent, even though the latter makes use of the more advanced Monte-Carlo test particle method.

Since the literature could not explain the best parameterization that should be used, tests have been carried out in order to determine the best setting for LEO POD (for Swarm C and GRACE A & B[3] for August 2014). They involved four different GSI algorithms for computing the accommodation coefficient (required to determine the lift and drag coefficients) and two different atmospheric models (the NRLMSISE-00 and the DTM2013) both with, and without, additional horizontal wind model (HWM14). The mean values and standard deviations of the differences with observations or measurement have been used to compare the different results. In most of the cases, the setting that gave the smallest mean values also gave the smallest STD. It is also important to mention that the few validations available for both Swarm C and GRACE A often showed similar results, their outcomes are listed bellow.

- Atmospheric model : DTM2013 is more precise for Swarm C in most of the cases, except for the SLR validation. However, for GRACE, the KBR range-rate and the differences with the measured accelerometer data are smaller when NRLMSISE-00 is used.

- Wind model : the effect of the horizontal wind model HWM14 is beneficial for all the cases using DTM2013. It is the opposite with NRLMSISE-00.

- Accommodation coefficient: the Goodman's method yields the best orbits for most of the cases. Moreover, the coefficient $f = 3.6$ yields the smallest values, except for SLR validations.

---

[1] From the 1^{st} to the 24^{th} of August.

[2] If an iterative algorithm is used (such as the external accelerations) or if the atmospheric model output is directly employed (such as modelled accelerations).

[3] The results for GRACE B are similar.

	Mean value reduction (%)			Reduction of the STD (%)		
Setting	**Radial**	**Along-track**	**Cross-track**	**Radial**	**Along-track**	**Cross-track**
Swarm C	7.06	-128.91	-96.69	-8.28	-56.11	-22.23
GRACE A	-87.51	-112.39	-22.71	-72.76	-74.74	-19.81

Table 9.1: Reduction of the piecewise constant accelerations of Swarm C and GRACE A when all the non-gravitational forces are implemented. The atmospheric model used is DTM2013 with HWM14, and the Goodman's method with $f = 3.6$ (see Eq. 3.18) has been used to compute the accommodation coefficient α.

Validation method	Value evaluated	Main orbital axis	Reduction (%)
GPS data fit	A posteriori STD of unit weight	all	-1.82
SLR	Mean range SLR residuals	Radial	0.71
SLR	STD of the SLR residuals	Radial	-1.87

Table 9.2: Improvement of the reduced-dynamic orbit Swarm C when all the non-gravitational forces are implemented. The atmospheric model used is DTM2013 with HWM14, and the Goodman's method with $f = 3.6$ (see Eq. 3.18) has been used to compute the accommodation coefficient α.

This "deduced" most precise parameterization has been used to obtain the results shown in Tables 9.1, 9.2 and 9.3.

The piecewise constant accelerations (PCA) of the reduced-dynamic orbits have shown the individual influences of the modelled non-gravitational forces. Table 9.1 shows the percentage reduction of the mean and standard deviation of the piecewise constant accelerations when all the forces are implemented. More specifically about the individually modelled forces:

- the impact of the SRP in terms of offset and amplitude variations is very sensitive to the optical properties of the macro-models used.
- the coupling[4] of the SRP and ERP force on the radial and cross-track axis is such that they shall be implemented together to ensure a POD improvement (see also Appendix H). To a larger extent, the most precise reduced-dynamic orbits have been computed when all the non-conservative forces are implemented.
- the reduction of the mean PCA is large on each axis, except in the radial direction of Swarm C probably due to inaccurate optical properties of the Swarm macro-models.
- the reduction of the STD in radial, along-track and cross track directions is large for both Swarm A and GRACE C.

The PCA of the reduced-dynamic orbit are absorbing the non-gravitational accelerations when not explicitly modelled. Since the implemented models capture variations in the non-gravitational accelerations that are shorter than the spacing of the PCA, one has an improvement. Tables 9.2 for Swarm and 9.3 for GRACE show, with various validation methods, the improvements of the reduced-dynamic POD (in percent). The improvement has been verified by SLR and KBR validations in addition to m_0, which gives an indication of the quality of the GPS data fit in the POD. The improvement of the GRACE A m_0 orbit is so large that it revealed a setting issue. The underlying cause of this larger improvement of GRACE A when compared with Swarm C is probably due to the lower altitude of GRACE A in 2014. Its lower altitude than in earlier years implies larger aerodynamic forces. So the *a priori* orbit was of poor quality then the way m_0 is computed in the *Bernese GNSS Software* becomes inaccurate.

One can also mention the side benefits of this assignment. Indeed a few interesting issues have been found while testing the implementation of the surface forces. First the setting issue of the GRACE *a priori* orbit. Secondly, an anomaly of the already implemented CERES data near the poles. Thirdly, a sign error in

---

[4] Forces which are acting along the same orbital axis.

Validation method	**Value evaluated**	**Orbital axis**	**Reduction (%)**
GPS data fit	A posteriori STD of unit weight	all	-37.56
SLR	Mean range SLR residuals	Radial	-41.00
SLR	STD of the SLR residuals	Radial	-7.60
KRB	STD of the range residuals	Along-track	-14.58
KBR	STD of the range-rate residuals	Along-track	-25.20

Table 9.3: Improvement of the reduced-dynamic orbit of GRACE when all the non-gravitational forces are implemented. The atmospheric model used is DTM2013 with HWM14, and the Goodman's method with $f = 3.6$ (see Eq. 3.18) has been used to compute the accommodation coefficient α.

equation 3.46 of [10]: $\hat{n}_i$ should be $-\hat{n}_i$. Finally, a possible attitude issue of GRACE A and B, which is currently under consideration.

9.2. LIMITS AND WEAKNESSES OF THE MODELS

Two relevant inconsistencies have been noticed: the excessive cross-track acceleration measured on-board of GRACE A (see Sec. 7.2) and the radial offset of the PCA of Swarm C (see Sec. 7.1). While the latter is mostly due to SRP and ERP, the cross-track acceleration involves the aerodynamic force and SRP. Further investigations of the accelerometer's issue suggests that the aerodynamic forces might be overestimated by 30%. It may be caused by inaccurate values given by the atmospheric model. Anyway, in both cases the solar radiation pressure seems to play a key role. A more in-depth investigation showed that different optical properties of the satellite surface are likely to solve a large part of the problem. The macro-models' optical properties of Swarm have been assumed; therefore a few imprecisions are not excluded. Additionally the different methods to compute the accommodation coefficient (key parameter in the computation of the atmospheric drag) have a noticeable impact on the resulting aerodynamic forces. In theory, the inconsistencies can be explained by the uncertainties concerning the inputs of the models (i.e. the various parameterization). However a simple test about the impact of the SRP upon POD, shown in Appendix H, demonstrates the strong coupling between the different non-conservative forces. It is shown that even though an individual force does not improve the accuracy, the same force gives better results when implemented with others than when it is excluded. So it is difficult to identify the force causing an inconsistency. Even if SRP seems to play a key role, it may well be caused by another force acting along the same orbital axis (i.e. coupled with SRP).

The precision limit of the modelled non-gravitational forces are essentially caused by the accuracy of the atmospheric models, macro-models, GSI algorithm and the gridded values of the Earth albedo and emissivity. Since the impact of varying atmospheric models, optical properties of the macro-models and GSI algorithms essentially led to change the acceleration's amplitude (similarly to a scale), this may justify to introduce scaling factors (it has not been explicitly tested in this assignment).

9.3. RECOMMENDATIONS FOR FUTURE RESEARCHES

Before implementing additional non-conservative forces or ameliorate the implemented models, it seems legitimate to conduct further validations over longer period of time. That would also gives more indications about the impact of the solar and geomagnetic indices on the results. In addition, evaluating the impact of surface forces when the Sun elevation angle is close to zero would give a better impression of the influence of SRP. On the other hand the effect of optical properties should be investigated in a more systematic way. Such an investigation would also require the implementation of material ageing (which was excluded in the scope of this project). As the influence of the optical properties is larger than initially expected the ageing of the satellite surface could be relevant for POD. Another interesting validations may be carried out to further assess the impact and precision of the implemented non-gravitational forces: purely dynamic orbit modelling. Indeed a purely dynamic orbit does not absorb the non-conservative forces with PCA, therefore the true impact of their implementation would be more visible and easier to compare with different parameterizations.

One should bear in mind that a scale difference between the modelled accelerations, the external data for Swarm C, the PCA and the modelled acceleration of GRACE A have been observed. Especially visible on the along-track or X_B-axis, it could justify to further investigate on the rescaling of the modelled aerodynamic forces, either in estimating C_D and $\vec{C}_r$ together with the PCA or in introducing scaling factors (estimated during the POD) that multiply each modelled acceleration. In other words, the influence of the computed non-gravitational accelerations could be scaled to minimize the PCA of the reduced-dynamic orbit, in order to compensate for the imprecision of the atmospheric models, optical properties of the macro-models and GSI algorithm. For instance, advanced corrections of existing atmospheric models, such as the HASDM (see also Sec. 3.3) are estimating a scale to correct the density given by the NRLMSISE-00. Focusing on the implementation of additional scaling factors, they may be introduced as force model parameters Q in the reduced-dynamic equation of motion (Eq. 5.1).

Finally, one would be tempted to implement additional forces and corrections like the thermal re-emissivity, solar irradiance variation or more elaborated shadow functions [52]. However, based on the results seen in this assignment, they would probably not improve POD. The implemented models are computing all the relevant non-conservative forces for LEO POD improvement.

BIBLIOGRAPHY

[1] L. H. Sentman, *Free molecule flow theory and its application to the determination of aerodynamic forces*, Tech. Rep. (DTIC Document, 1961).

[2] S. Bruinsma and R. Biancale, *Total densities derived from accelerometer data,* Journal of Spacecraft and Rockets **40**, 230 (2003).

[3] R. Dach, S. Lutz, P. Walser, and P. Fridez, *Bernese GNSS Software*, AIUB, 5th ed. (2015).

[4] H. Klinkrad, C. Koeck, and P. Renard, *Key features of a satellite skin force modelling technique by means of monte-carlo ray tracing,* Advances in Space Research **11**, 147 (1991).

[5] A. Jäggi, *Pseudo stochastic orbit modelling of low earth satellites using the global positioning system. geodätisch-geophysikalische arbeiten in der schweiz, 73, schweizerische geodätische kommission,* Technische Hochschule Zürich, Zürich (2007).

[6] O. Montenbruck and E. Gill, *Satellite orbits: models, methods and applications* (Springer Science & Business Media, 2012).

[7] G. Afonso, F. Barlier, C. Berger, F. Mignard, and J. Walch, *Reassessment of the charge and neutral drag of lageos and its geophysical implications,* Journal of Geophysical Research: Solid Earth **90**, 9381 (1985).

[8] X. Zhu, E. Talaat, J. Baker, and J.-H. Yee, *A self-consistent derivation of ion drag and joule heating for atmospheric dynamics in the thermosphere,* Annales Geophysicae **23**, 3313 (2005).

[9] C. A. Belk, J. H. Robinson, M. B. Alexander, W. J. Cooke, and S. D. Pavelitz, *Meteoroids and orbital debris: effects on spacecraft*, Tech. Rep. (NASA, 1997).

[10] E. Doornbos, *Thermospheric density and wind determination from satellite dynamics* (Springer Science & Business Media, 2012).

[11] D. Vokrouhlicky, P. Farinella, and F. Mignard, *Solar radiation pressure perturbations for earth satellites. iv. effects of the earth's polar flattening on the shadow structure and the penumbra transitions.* Astronomy and Astrophysics **307**, 635 (1996).

[12] D. P. Rubincam and N. R. Weiss, *Earth albedo and the orbit of lageos,* Celestial mechanics **38**, 233 (1986).

[13] M. Ziebart, *Generalized analytical solar radiation pressure modeling algorithm for spacecraft of complex shape,* Journal of spacecraft and rockets **41**, 840 (2004).

[14] G. Beutler, *Methods of celestial mechanics. Vol. II: Application to planetary system geodynamics and satellite geodesy. Astronomy and Astrophysics Library. Berlin: Springer, ISBN 3-540-40750-2*, Vol. 2 (2005).

[15] P. C. Knocke, J. C. Ries, and B. D. Tapley, *Earth radiation pressure effects on satellites 88-4292-cp. aiaa,* , 577.

[16] D. Sidorov, *Orbit/SRP Modelling for Long Term Prediction*, Tech. Rep. (AIUB, 2015).

[17] E. Doornbos, *Non-gravitational force modelling for pod of altimetry satellites,* (2002).

[18] J. Duha, G. B. Afonso, and L. D. D. Ferreira, *Thermal re-emission effects on gps satellites,* Journal of Geodesy **80**, 665 (2006).

[19] J. Andrés, R. Noomen, G. Bianco, D. Currie, and T. Otsubo, *Spin axis behavior of the lageos satellites,* Journal of Geophysical Research: Solid Earth **109** (2004).

[20] *S-Band Patch Antenna*, Tech. Rep. (SURREY Satellite Technology Ltd, 2015).

[21] J. D. Anderson Jr, *Fundamentals of aerodynamics* (Tata McGraw-Hill Education, 2010).

[22] D. A. Vallado and D. Finkleman, *A critical assessment of satellite drag and atmospheric density modeling,* Acta Astronautica **95**, 141 (2014).

[23] E. Doornbos, M. Förster, B. Fritsche, T. van Helleputte, J. van den IJssel, G. Koppenwallner, H. Lühr, D. Rees, P. Visser, and M. Kern, *Air density models derived from multi-satellite drag observations,* in *Proceedings of ESAs second swarm international science meeting, Potsdam Germany* (2009) pp. 24–26.

[24] K. Moe, M. M. Moe, and C. J. Rice, *Simultaneous analysis of multi-instrument satellite measurements of atmospheric density,* Journal of spacecraft and rockets **41**, 849 (2004).

[25] R. Schamberg, *Analytic representation of surface interaction for free molecule flow with application to drag of various bodies,* Aerodynamics of the Upper Atmosphere , 12 (1959).

[26] G. Cook, *Satellite drag coefficients,* Planetary and Space Science **13**, 929 (1965).

[27] S. A. Schaaf and P. L. Chambré, *Flow of rarefied gases* (Princeton University Press, 1961).

[28] J. C. Gregory and P. N. Peters, *A measurement of the angular distribution of 5 ev atomic oxygen scattered off a solid surface in earth orbit,* Proceedings of the 15th International Symposium on Rarefied Gas Dynamics (1987).

[29] K. Moe, M. M. Moe, and S. D. Wallace, *Improved satellite drag coefficient calculations from orbital measurements of energy accommodation,* Journal of spacecraft and rockets **35**, 266 (1998).

[30] E. K. Sutton, *Normalized force coefficients for satellites with elongated shapes,* Journal of Spacecraft and Rockets **46**, 112 (2009).

[31] S. Adhya, M. Ziebart, A. Sibthorpe, P. Arrowsmith, and P. Cross, *Thermal force modeling for precise prediction and determination of spacecraft orbits,* Navigation **52**, 131 (2005).

[32] E. K. Sutton, R. S. Nerem, and J. M. Forbes, *Density and winds in the thermosphere deduced from accelerometer data,* Journal of Spacecraft and Rockets **44**, 1210 (2007).

[33] K. Moe and M. M. Moe, *Gas–surface interactions and satellite drag coefficients,* Planetary and Space Science **53**, 793 (2005).

[34] G. Koppenwallner, *Comment on special section: new perspectives on the satellite drag environments of earth, mars, and venus,* Journal of Spacecraft and Rockets **45**, 1324 (2008).

[35] E. Hecht, *Physique*, edited by de boek (2009).

[36] C. Pardini, L. Anselmo, K. Moe, and M. Moe, *Drag and energy accommodation coefficients during sunspot maximum,* Advances in Space Research **45**, 638 (2010).

[37] M. R. Reddy, *Effect of low earth orbit atomic oxygen on spacecraft materials,* Journal of Materials Science **30**, 281 (1995).

[38] G. Koppenwallner, D. A. Levin, I. J. Wysong, and A. L. Garcia, *Satellite aerodynamics and determination of thermospheric density and wind,* in *AIP Conference Proceedings-American Institute of Physics*, Vol. 1333 (2011) p. 1307.

[39] B. Fritsche, M. Ivanov, A. Kashkovsky, G. Koppenwallner, A. Kudryavtsev, U. Voskoboinikov, and G. Zhukova, *Radiation pressure forces on complex spacecraft,* HTG, Germany and ITAM Russia, ESOC contract **11908**, 96 (1998).

[40] D. Johannsmeier and K. G., *Analytical and Numerical Formulation of Lift and Drag for Satellites in Free Molecular Flow*, Report 90-3 (HTG, 1990).

[41] G. A. Bird, *Molecular gas dynamics and the direct simulation of gas flows. clarendon,* (1994).

[42] G. Koppenwallner, *Energy accommodation coefficient and momentum transfer modeling,* Tech. Rep. (Hyperschall Technologie Göttingen GmbH TN-08-11, Katlenburg Lindau, Germany, 2009).

[43] M. Knudsen, *Die molekulare Wärmeleitung der Gase und der Akkommodationskoeffizient*, Vol. 339 (Wiley Online Library, 1911) pp. 593–656.

[44] F. O. Goodman, *Three-dimensional hard spheres theory of scattering of gas atoms from a solid surface i. limit of large incident speed,* (1967).

[45] M. D. Pilinski, B. M. Argrow, and S. E. Palo, *Semiempirical model for satellite energy-accommodation coefficients,* Journal of Spacecraft and Rockets **47**, 951 (2010).

[46] A. W. Adamson, A. P. Gast, *et al.*, *Physical chemistry of surfaces* (Interscience New York, 1967).

[47] E. Doornbos, H. Klinkrad, R. Scharroo, and P. Visser, *Thermosphere density calibration in the orbit determination of ers-2 and envisat,* Proceedings of the Envisat Sympo (2000).

[48] M. D. Pilinski, B. M. Argrow, S. E. Palo, and B. R. Bowman, *Semi-empirical satellite accommodation model for spherical and randomly tumbling objects,* Journal of Spacecraft and Rockets **50**, 556 (2013).

[49] J. Picone, A. Hedin, D. P. Drob, and A. Aikin, *Nrlmsise-00 empirical model of the atmosphere: Statistical comparisons and scientific issues,* Journal of Geophysical Research: Space Physics **107** (2002).

[50] S. Bruinsma, *The dtm-2013 thermosphere model,* Journal of Space Weather and Space Climate **5**, A1 (2015).

[51] M. F. Storz, B. R. Bowman, and J. I. Major Branson, *High accuracy satellite drag model (hasdm),* AIAA/AAS Astrodynamics Specialist Conference and Exhibit 5-8 August 2002 (2002).

[52] R. Robertson, J. Flury, T. Bandikova, and M. Schilling, *Highly physical penumbra solar radiation pressure modeling with atmospheric effects,* Celestial Mechanics and Dynamical Astronomy **123**, 169 (2015).

[53] O. Montenbruck, P. Steigenberger, and U. Hugentobler, *Enhanced solar radiation pressure modeling for galileo satellites,* Journal of Geodesy **89**, 283 (2015).

[54] D. Arnold, M. Meindl, G. Beutler, R. Dach, S. Schaer, S. Lutz, L. Prange, K. Sośnica, L. Mervart, and A. Jäggi, *Code's new solar radiation pressure model for gnss orbit determination,* Journal of Geodesy **89**, 775 (2015).

[55] H. Klinkrad and B. Fritsche, *Orbit and attitude perturbations due to aerodynamics and radiation pressure,* in *ESA Workshop on Space Weather, ESTEC, Noordwijk, Netherlands* (1998).

[56] J. Ries, C. Shum, and B. Tapley, *Surface force modeling for precision orbit determination,* Environmental Effects on Spacecraft Positioning and Trajectories , 111 (1993).

[57] K. Sośnica, *Determination of precise satellite orbits and geodetic parameters using satellite laser ranging* (Astronomical Institute, University of Bern, Switzerland, 2014).

[58] D. Vokrouhlicky, P. Farinella, and F. Mignard, *Solar radiation pressure perturbations for earth satellites. 1: A complete theory including penumbra transitions,* Astronomy and Astrophysics **280**, 295 (1993).

[59] P. C. Knocke, J. C. Ries, and B. D. Tapley, *Earth radiation pressure effects on satellites,* AIAA , 577 (1988).

[60] B. R. Barkstrom, E. F. Harrison, and R. B. Lee, *Earth radiation budget experiment,* Eos, Transactions American Geophysical Union **71**, 297 (1990).

[61] W. B. A., B. R. Barkstrom, E. F. Harrison, L. I. R. B., G. L. Smith, and J. E. Cooper, *Clouds and the earth's radiant energy system (ceres): An earth observing system experiment,* Bulletin of the American Meterological Society **77** (1996).

[62] C. L.-H. and J. L. Robbins, *Clouds and the Earth Radiant Energy System, DRAFT ES-8 Collection Guide*, Tech. Rep. (NASA, 2003).

[63] P. Dong-ju and W. Bin, *Kinematic precise orbit determination for leo satellites using space-borne dual-frequency gps measurements,* Chinese Astronomy and Astrophysics **36**, 291 (2012).

[64] O. Montenbruck, T. Van Helleputte, R. Kroes, and E. Gill, *Reduced dynamic orbit determination using gps code and carrier measurements,* Aerospace Science and Technology **9**, 261 (2005).

[65] H. Fliegel, T. Gallini, and E. Swift, *Global positioning system radiation force model for geodetic applications,* Journal of Geophysical Research: Solid Earth **97**, 559 (1992).

[66] H. F. Fliegel and T. E. Gallini, *Solar force modeling of block iir global positioning system satellites,* Journal of Spacecraft and Rockets **33**, 863 (1996).

[67] T. Springer, G. Beutler, and M. Rothacher, *A new solar radiation pressure model for gps satellites,* GPS solutions **2**, 50 (1999).

[68] L. Berthoud and J. Mandeville, *Material damage in space from microparticle impact,* Journal of materials science **32**, 3043 (1997).

[69] B. Tapley and C. Reigber, *The grace mission: status and future plans, AGU Fall Meeting Abstracts,* **1**, 02 (2001).

[70] C. Dunn, W. Bertiger, Y. Bar-Sever, S. Desai, B. Haines, D. Kuang, G. Franklin, I. Harris, G. Kruizinga, T. Meehan, *et al.*, *Application challenge-instrument of grace-gps augments gravity measurements-twin satellites trail each other in earth orbit. as they pass over contours in the gravity field, they first,* GPS world **14**, 16 (2003).

[71] P. Touboul, E. Willemenot, B. Foulon, and V. Josselin, *Accelerometers for champ, grace and goce space missions: synergy and evolution,* Boll. Geof. Teor. Appl **40**, 321 (1999).

[72] E. Friis-Christensen, H. Lühr, D. Knudsen, and R. Haagmans, *Swarm–an earth observation mission investigating geospace,* Advances in Space Research **41**, 210 (2008).

[73] V. Fedosov and R. Peřestỳ, *Measurement of microaccelerations on board of the leo spacecraft,* IFAC Proceedings Volumes **44**, 1883 (2011).

[74] C. Siemens, E. Encarnação J. T., E. Doornbos, J. Van den IJssel, J. Kraus, R. Pereštý, L. Grunwaldt, G. Apelbaum, J. Flury, and P. E. H. Olsen, *Swarm accelerometer data processing from raw accelerations to thermospheric neutral densities,* Earth, Planets and Space **68** (2016), 10.1186/s40623-016-0474-5.

[75] D. P. Rubincam and N. R. Weiss, *Earth albedo and the orbit of lageos,* Celestial mechanics **38**, 233 (1986).

[76] E. Raschke, S. Kinne, W. B. Rossow, P. W. Stackhouse Jr, and M. Wild, *Comparison of radiative energy flows in observational datasets and climate modeling,* Journal of Applied Meteorology and Climatology **55**, 93 (2016).

[77] D. Drob, J. Emmert, G. Crowley, J. Picone, G. Shepherd, W. Skinner, P. Hays, R. Niciejewski, M. Larsen, C. She, *et al.*, *An empirical model of the earth's horizontal wind fields: Hwm07,* Journal of Geophysical Research: Space Physics **113** (2008).

[78] D. P. Drob, J. T. Emmert, J. W. Meriwether, J. J. Makela, E. Doornbos, M. Conde, G. Hernandez, J. Noto, K. A. Zawdie, S. E. McDonald, *et al.*, *An update to the horizontal wind model (hwm): The quiet time thermosphere,* Earth and Space Science **2**, 301 (2015).

[79] B. L. Stevens and F. L. Lewis, *Aircraft control and simulation, john wiley & sons,* Inc., New York (1992).

[80] E. Doornbos, S. Bruinsma, S. Fritsche, G. Koppenwallner, P. Visser, J. van den IJssel, and J. d. T. de Encarnacao, *GOCE+ theme 3: Air density and wind retrieval using GOCE data final report*, Tech. Rep. (4000102847/NL/EL, 2014).

[81] D. Knudsen, J. Burchill, S. Buchert, I. Coco, L. Toffner-Clausen, and P. L. Holmdahl-Olsen, *Swarm preliminary plasma dataset user note,* (2015).

[82] B. Klinger and T. Mayer-Gürr, *The role of accelerometer data calibration within grace gravity field recovery: Results from itsg-grace2016,* Advances in Space Research (2016).

[83] U. Meyer, A. Jäggi, and G. Beutler, *The impact of attitude control on grace accelerometry and orbits, Geodesy for Planet Earth,* , 139 (2012).

[84] U. Meyer, A. Jäggi, Y. Jean, and D. Arnold, *Improving the noise model for aiub monthly gravity field solution,* (2015).

[85] C. J. R. Solano, *Impact of albedo modelling on gps orbits,* (2009).

[86] P. Lucey, G. Neumann, M. Riner, E. Mazarico, D. Smith, M. Zuber, D. Paige, D. Bussey, J. Cahill, A. McGovern, *et al.*, *The global albedo of the moon at 1064 nm from lola,* Journal of Geophysical Research: Planets **119**, 1665 (2014).

[87] H. Araki, S. Tazawa, H. Noda, Y. Ishihara, S. Goossens, S. Sasaki, N. Kawano, I. Kamiya, H. Otake, J. Oberst, *et al.*, *Lunar global shape and polar topography derived from kaguya-lalt laser altimetry,* Science **323**, 897 (2009).

A

ACRONYMS

AIUB	Astronomical Institute of the University of Bern
ANGARA	Analysis of Non-Gravitational Accelerations due to Radiation and Aerodynamics
CERES	Clouds Earth's Radiant Energy System
C/A	Coarse-Acquisition code
DLR	Deutsches Zentrum für Luft- und Raumfahrt
DGFI	Deutsches Geodätisches Forschungsinstitut
DSMC	Direct Simulation Monte Carlo
ECEF	Earth-Centered, Earth-Fixed frame (F_E)
ECI	Earth-Centered Inertial (F_I)
ERBE	Earth Radiation Budget Experiment
ERP	Earth Radiation Pressure
ERS	European Remote-Sensing Satellite
ESA	European Space Agency
FEM	Finite Element Method
GNSS	Global Navigation Satellite System
GPS	Global Positioning System
GRACE	Gravity Recovery And Climate Experiment
GSI	Gas-Surface Interaction
HWM14	Horizontal Wind Model 2014
IR	Infrared
KBR	K/Ka-Band Ranging
LAGEOS	Laser Geodynamics Satellite
LEO	Low Earth Orbiter
MEO	Medium Earth Orbiter
OSR	Optical Solar reflectors
P	Precise code
PCA	Piecewise Constant Accelerations
POD	Precise Orbit Determination
RAMSES	Rarified Aerodynamics Modeling System for Earth Satellites
RMS	Root Mean Square
RSW	Radial, Along-track and Cross-track Orbital frame
RTP	Ray Tracing Panel
RTV	Room temperature vulcanized
SBF	Satellite Body-Fixed (F_B)
SLR	Satellite Laser Ranging
SRP	Solar Radiation pressure
SLR	Satellite Laser Ranging

STD	Standard Deviation
TOA	Top-Of-Atmosphere
TOE	True System of Epoch
TPMC	Test Particle Monte Carlo
UT	Universal Time
UV	Ultra-Violet
Y	Encrypted P-code

B

Moon Radiation Pressure

The Moon radiation pressure on Swarm C was estimated for the 19^{th} of July 2014 (three days before full Moon) using an analytical method adapted for the Moon (Eq. B.1) [85]. This equation includes both the emitted and reflected Moon radiation pressure. Since one is considering the Moon as one single Lambertian surface, the emissivity coefficient is deduced by $1 - a_{\leftmoon}$. The Moon is assumed to not emit infrared radiations when not illuminated. For Swarm C, the estimated Moon radiation pressure led to a maximum acceleration of $10^{-27} m/s^2$, that is far too small for any POD improvement.

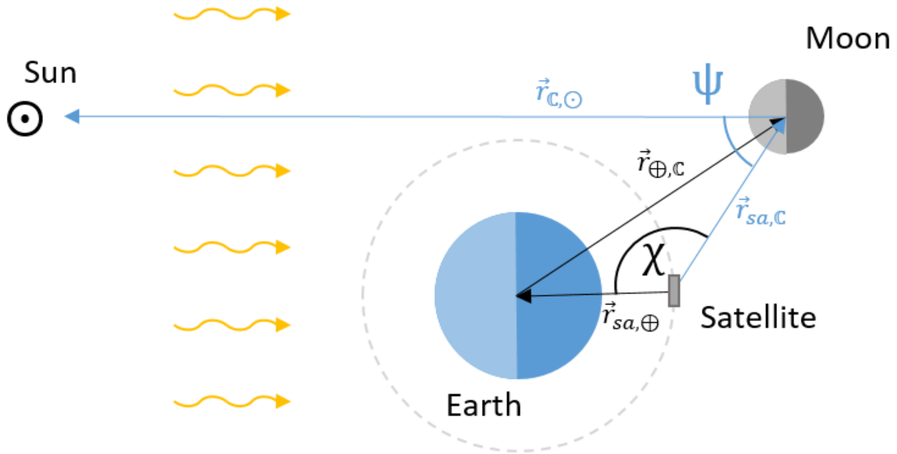

Figure B.1: Graphical representation of the vectors used to model the Moon radiation pressure.

If $\psi < \frac{\pi}{2}$ (because an analytical method is used, the Moon-Sun vector is the only source of radiation pressure) and $\chi < \arcsin\left(\frac{R_\oplus}{\|\vec{r}_{\oplus,sa}\|}\right)$ the satellite is visible for the Moon and the reflected solar radiations can reach the satellite

$$\ddot{\vec{r}}_{MRP} = \vec{C}_r \frac{A_{ref}}{m}\left(\frac{1AU}{\|\vec{r}_{\leftmoon,\odot}\|}\right)^2 P_{1AU}\frac{\pi R_{\leftmoon}^2}{\|\vec{r}_{\leftmoon,sa}\|}\left[\frac{2a_{\leftmoon}}{3\pi^2}\left((\pi-\psi)cos(\psi)+sin(\psi)\right)+\frac{(1-a_{\leftmoon})}{4\pi}\right]. \qquad \text{(B.1)}$$

ψ	angle satellite - Moon - Sun
χ	angle Earth - satellite - Moon
$\vec{r}_{\leftmoon,\odot}$	Moon-Sun vector
$\vec{r}_{\leftmoon,sa}$	Moon - satellite vector
$\vec{r}_{\oplus,sa}$	Earth-satellite vector
$\vec{r}_{\oplus,\leftmoon}$	Earth-Moon vector
$a_{\leftmoon}$	Moon albedo 0.3 [86]
$R_{\leftmoon}$	Moon mean radius 1737150 m [87]
$R_\oplus$	Earth mean radius 6371000 m

C

Macro-models

Panel	**Area (m^2)**	**Unit normal**			**Material**	$p_{s,IR}$	$p_{d,IR}$	$p_{s,VI}$	$p_{d,VI}$
Front	0.955	1.0	0.0	0.0	SiO_2/Kapton	0.23	0.15	0.4	0.26
Rear	0.955	-1.0	0.0	0.0	SiO_2/Kapton	0.23	0.15	0.4	0.26
Starboard outer	3.156	0.0	0.766	-0.643	SiO_2	0.03	0.16	0.05	0.3
Starboard inner	0.228	0.0	-0.766	0.643	SiO_2/Kapton	0.23	0.15	0.4	0.26
Port outer	3.156	0.0	-0.766	-0.643	SiO_2	0.03	0.16	0.05	0.3
Port inner	0.228	0.0	0.766	0.643	SiO_2/Kapton	0.23	0.15	0.4	0.26
Nadir	6.071	0.0	0.0	1.0	$Teflon$®	0.19	0.06	0.68	0.20
Zenith	2.167	0.0	0.0	-1.0	SiO_2	0.03	0.16	0.05	0.3

Table C.1: Macro-model used for GRACE.

Panel	**Part of panel Area (%)**	**Actual material**
Nadir I	15	Aluminum/ Alodine Foil
	70	OSR Radiator
	10	Black Kapton
	5	Beta Cloth
Nadir II	12	OSR Radiator
	10	Beta Cloth
	78	Black Kapton
Nadir III	8	OSR Radiator
	92	Black Kapton
Solar Array +Y	78	Solar Cell
	22	RTV Adhesive
Solar Array -Y	78	Solar Cell
	22	RTV Adhesive
Zenith	100	Black Kapton
Front	90	Aluminum/ Alodine Foil
	10	OSR Radiator
Side Wall +Y	95	Black Kapton
	5	Beta Cloth
Side Wall -Y	95	Black Kapton
	5	Beta Cloth
Shear Panel Nadir Front	100	Beta Cloth
Shear Panel Nadir Back	100	Black Kapton
Boom +Y	40	Black Kapton
	60	Beta Cloth
Boom -Y	40	Black Kapton
	60	Beta Cloth
Boom Zenith	80	Black Kapton
	20	Beta Cloth
Boom Nadir	100	Beta Cloth

Table C.2: Composition of the panels for Swarm.

Swarm material	**Assumed similar material properties material properties**	$p_{s,IR}$	$p_{d,IR}$	$p_{s,VI}$	$p_{d,VI}$
Aluminium/ Alodine Foil	Kapton/al	0.64	0.20	0.71	0.22
Black Kapton	SiO_2/Kapton	0.03	0.16	0.05	0.30
Beta Cloth	$Teflon^{®}$	0.19	0.06	0.68	0.20
OSR Radiator	Gold foil	0.40	0.26	0.23	0.15
Solar cell	SiO_2	0.03	0.16	0.05	0.30
RTV Adhesive	Sandblasted Aluminium	0.20	0.40	0.26	0.51
White Paint	-	0.00	1.00	0.00	1.00

Table C.3: Assumed Swarm material surface properties, based on the available surface properties given by [2].

Panel	**Area (m^2)**	**Unit normal**			$\boldsymbol{p_{s,IR}}$	$\boldsymbol{p_{d,IR}}$	$\boldsymbol{p_{s,VI}}$	$\boldsymbol{p_{d,VI}}$
Nadir I	1.540	0.0	0.0	1.0	0.25	0.09	0.61	0.21
Nadir II	1.400	-0.198	0.0	0.980	0.07	0.15	0.19	0.29
Nadir III	1.600	-0.138	0.0	0.990	0.05	0.16	0.08	0.30
Solar Array +Y	3.450	0.0	0.588	-0.809	0.02	0.34	0.04	0.27
Solar Array -Y	3.450	0.0	-0.588	-0.809	0.02	0.34	0.04	0.27
Zenith	0.500	0.0	0.0	-1.0	0.03	0.16	0.05	0.30
Front	0.560	1.0	0.0	0.0	0.64	0.30	0.42	0.58
Side Wall +Y	0.753	0.0	1.0	0.0	0.04	0.16	0.08	0.30
Side Wall -Y	0.753	0.0	-1.0	0.0	0.04	0.16	0.08	0.30
Shear Panel Nadir Front Nadir Front	0.800	1.0	0.0	0.0	0.19	0.06	0.68	0.20
Shear Panel Nadir Back	0.800	-1.0	0.0	0.0	0.19	0.06	0.68	0.20
Boom +Y	0.600	0.0	1.0	0.0	0.13	0.10	0.43	0.24
Boom -Y	0.600	0.0	-1.0	0.0	0.13	0.10	0.43	0.24
Boom Zenith	0.600	-0.239	0.0	-0.971	0.06	0.14	0.18	0.28
Boom Nadir	0.600	0.228	0.0	0.974	0.19	0.06	0.68	0.20

Table C.4: Macro-model used for Swarm. The optical properties have been computed based on the material composition of the panels given in Table C.2, with the corresponding material properties of Table C.3.

D

ALGEBRAIC PROOF OF THE PHOTON-SURFACE INTERACTION CROSSING ANGLES

Fig. 5.11 shows that $\vec{C}_s = \vec{C}_d$ once for $\theta \in [0,90]°$. Recall the definition of gamma: $\gamma = -\hat{r}_{so,sa} \cdot \hat{n}$

$$\begin{aligned}
&\vec{C}_s = \vec{C}_d \\
&\iff -2\gamma\hat{n}\frac{A_i\gamma}{A_{ref}} = (\hat{r}_{so,sa} - \frac{2}{3}\hat{n})\frac{A_i\gamma}{A_{ref}} \\
&\iff -2\gamma\hat{n} = \hat{r}_{so,sa} - \frac{2}{3}\hat{n} \\
&\iff -2\gamma(\hat{r}_{so,sa}\hat{n}) = \hat{r}_{so,sa}\cdot\hat{r}_{so,sa} - \frac{2}{3}\hat{r}_{so,sa}\cdot\hat{n} \\
&\iff -2\gamma(-\gamma) = \|\hat{r}_{so,sa}\|^2 - \frac{2}{3}(-\gamma) \\
&\iff 2\gamma^2 = 1 + \frac{2}{3}\gamma \\
&\iff 2\gamma^2 - \frac{2}{3}\gamma - 1 = 0 \\
&\implies \gamma = \frac{2 \pm \sqrt{4+72}}{12} \\
&\iff \theta = \arccos\left(\frac{2 \pm \sqrt{4+72}}{12}\right) = 26.7° \text{ or } 124.0°,
\end{aligned} \tag{D.1}$$

then the only possibility between 0 and 90 ° is 26.7 °.

The second equality visible on Fig. 5.11 is when $\vec{C}_s = \vec{C}_a$,

$$\begin{aligned}
&\vec{C}_s = \vec{C}_a \\
&\iff -2\gamma\hat{n}\frac{A_i\gamma}{A_{ref}} = \hat{r}_{so,sa}\frac{A_i\gamma}{A_{ref}} \\
&\iff -2\gamma\hat{n} = \hat{r}_{so,sa} \\
&\iff -2\gamma(\hat{r}_{so,sa}\hat{n}) = (\hat{r}_{so,sa}\hat{r}_{so,sa}) \\
&\iff -2\gamma(-\gamma) = \|\hat{r}_{so,sa}\|^2 \\
&\iff 2\gamma^2 = 1 \\
&\iff \gamma = \sqrt{\frac{1}{2}} = \frac{\sqrt{2}}{2} \\
&\iff \theta = \arccos(\frac{\sqrt{2}}{2}) = \pm 45.0°,
\end{aligned} \tag{D.2}$$

then the only possibility between 0 and 90 ° is 45.0 °.

E

IMPACT OF INDIVIDUAL NON-GRAVITATIONAL FORCES

The reader will find the statistics of the piecewise constant accelerations and the *a posteriori* σ of unit weight of the reduced-dynamic orbit when individual non-gravitational forces are modelled. The statistics are based on 24 sample days from day 213 to 236 of year 2014 (for Swarm C, day 217 is missing). MRLMSISE-00 with HWM14 have been used. In addition, the Goodman's method with $f = 3.6$ has been used to model the accommodation coefficient.

Tables E.1 for Swarm C, and E.2 for GRACE A, show the mean values and standard deviations of the PCA (of the reduced-dynamic orbit) when only one non-gravitational force is modelled (see Sec. 7.1 for more details about PCA). The most important observation is the ambiguous impact of the SRP. For Swarm C, it leads to a larger radial PCA but a smaller STD along the three axes. For GRACE A it also increases the radial PCA, but the STD increases along the three axes. Further investigations on the SRP (shown in Appendix H) showed that the SRP is strongly coupled with ERP and aerodynamic lift, so implementing them individually does not always improve the reduced-dynamic orbit. This is also visible in Table E.3, which shows the *a posteriori* σ of unit weight m_0 (see Sec. 7.3 for more details about m_0). For Swarm C, ERP increases m_0 and SRP reduces it. For GRACE A it is the opposite. Note that for both, the lowest values of m_0 are obtained when all the forces are implemented.

	Mean (m/s^2)			**STD (m/s^2)**		
Setting	**Radial**	**Along-track**	**Cross-track**	**Radial**	**Along-track**	**Cross-track**
No surface force	4.55E-08	-1.32E-07	-3.04E-08	4.96E-08	9.69E-08	4.51E-08
Emitted ERP	3.80E-08	-1.32E-07	-3.04E-08	4.99E-08	9.70E-08	4.51E-08
Reflected ERP	4.18E-08	-1.32E-07	-3.03E-08	5.06E-08	9.71E-08	4.51E-08
SRP	5.76E-08	-1.31E-07	-0.84E-08	4.60E-08	9.44E-08	3.75E-08
Aerodyn. lift	4.80E-08	-1.32E-07	-2.99E-08	4.93E-08	9.69E-08	4.44E-08
Aerodyn. drag	4.53E-08	0.53E-07	-2.33E-08	4.91E-08	4.94E-08	4.00E-08
All the forces	4.90E-08	0.54E-07	-0.06E-08	4.64E-08	4.60E-08	3.51E-08

Table E.1: Statistics of the piecewise constant accelerations of Swarm C if individual non-gravitational forces are implemented. The statistical values are computed based on the 23 sample days from day 213 to 236, except day 217, of year 2014.

	Mean (m/s^2)			STD (m/s^2)		
Setting	**Radial**	**Along-track**	**Cross-track**	**Radial**	**Along-track**	**Cross-track**
No surface force	0.58E-08	-2.58E-07	2.58E-08	3.44E-08	1.11E-07	1.97E-08
Emitted ERP	-0.29E-08	-2.58E-07	2.57E-08	3.45E-08	1.11E-07	1.97E-08
Reflected ERP	-0.03E-08	-2.58E-07	2.55E-08	3.45E-08	1.11E-07	1.97E-08
SRP	2.04E-08	-2.58E-07	1.23E-08	3.57E-08	1.13E-07	2.13E-08
Aerodyn. lift	0.28E-08	-2.58E-07	2.54E-08	3.44E-08	1.11E-07	1.95E-08
Aerodyn. drag	0.63E-08	0.31E-07	3.06E-08	1.28E-08	0.44E-07	2.08E-08
All the forces	0.28E-08	0.31E-07	1.69E-08	1.06E-08	0.42E-07	1.58E-08

Table E.2: Statistics of the piecewise constant accelerations of GRACE A if individual non-gravitational forces are implemented. The statistical values are computed based on the 24 sample days from day 213 to 236 of year 2014.

Setting	Swarm C mean value (mm)	GRACE A mean value (mm)
No surface force	1.9608	2.322
Emitted ERP	1.9608	2.321
Reflected ERP	1.9609	2.324
SRP	1.9537	2.381
Aerodyn. lift	1.9604	2.318
Aerodyn. drag	1.9310	1.535
All the forces	1.9266	1.467

Table E.3: Mean m_0 of the reduced-dynamic orbit of Swarm C and GRACE A

F

Supplement to Chapter 6

Fig. F.1 aims to show that different solar (F10.7 and the 81 day average of the F10.7) and geomagnetic indices (ap) may cause the daily changing variation with the external data presented in Sec. 6.1 for two reasons. First the variation is changing daily, so are the solar indices. On the other hand, varying these indices by 5 % (see Fig. F.1) leads to a similar difference as between the modelled and external accelerations (see Fig. 6.1).

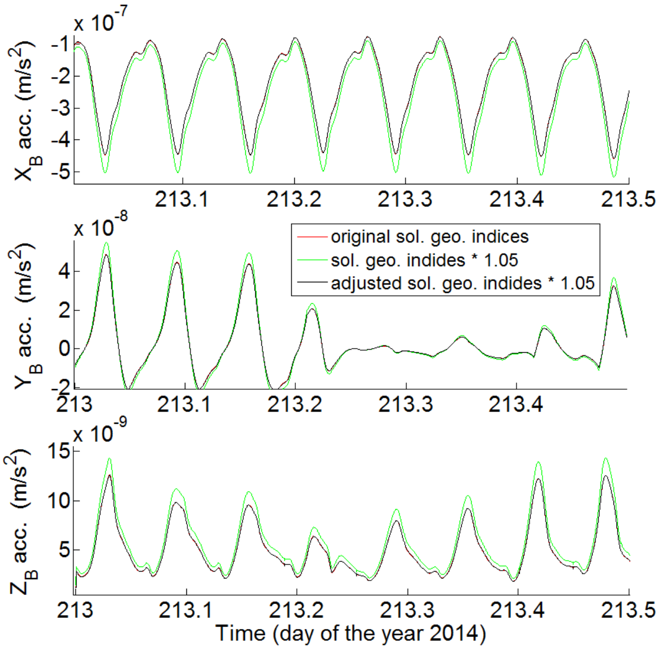

Figure F.1: Impact of increasing solar and geomagnetic indices by 5 % on the aerodynamic accelerations. The modelled accelerations with the original solar and geomagnetic indices (in red). modelled accelerations with 5 % larger solar and geomagnetic indices (in green). Least-squares adjusted accelerations (in black) of the green curve.

Setting	**Mean** (m/s^2)			**STD** (m/s^2)		
	X_B-axis	Y_B-axis	Z_B-axis	X_B-axis	Y_B-axis	Z_B-axis
No wind model	-1.02E-12	3.11E-13	3.44E-14	1.11E-08	2.97E-09	2.77E-10
HWM14	-1.18E-12	2.43E-13	2.30E-14	1.01E-08	1.45E-09	2.52E-10

Table F.1: Statistics of the differences between the modelled and **adjusted** external data. The atmospheric model used is the NRLMSISE-00 and Goodman's method with $f = 3.6$ has been used to compute α.

	Mean (m/s^2)				**STD** (m/s^2)			
Setting	α	X_B-axis	Y_B-axis	Z_B-axis	α	X_B-axis	Y_B-axis	Z_B-axis
$\alpha_{G,1}$	0.60	-1.39E-12	2.88E-13	0.82E-14	0.006	1.13E-08	1.72E-09	3.84E-10
$\alpha_{G,2}$	0.90	-1.18E-12	2.43E-13	2.30E-14	0.009	1.01E-08	1.45E-09	2.52E-10
$\alpha_{P,1}$	0.47	-0.86E-12	2.42E-13	-5.79E-14	0.165	1.07E-08	1.70E-09	3.62E-10
$\alpha_{P,2}$	0.56	-0.84E-12	2.35E-13	-5.31E-14	0.163	1.04E-08	1.65E-09	3.40E-10

Table F.2: Statistics of the differences between the modelled and **adjusted** external aerodynamic accelerations. The mean and STD value of the modelled α is also shown. NRLMSISE-00 and HWM14 have been used.

Setting	**Mean** (m/s^2)			**STD** (m/s^2)		
	X_B-axis	Y_B-axis	Z_B-axis	X_B-axis	Y_B-axis	Z_B-axis
NRLMSISE-00	-1.18E-12	2.43E-13	2.30E-14	1.01E-08	1.45E-09	2.52E-10
DTM2013	-0.29E-12	2.06E-13	0.30E-14	1.48E-08	1.59E-09	3.79E-10

Table F.3: Statistics of the differences between the modelled and **adjusted** external data over the available sample days. HWM14 and $\alpha_{G,2}$ have been used to compute the accommodation coefficient.

	Mean (m/s^2)			**STD** (m/s^2)		
Setting	X_B-axis	Y_B-axis	Z_B-axis	X_B-axis	Y_B-axis	Z_B-axis
Original macro-model	3.96E-10	-0.80E-09	1.00E-09	1.70E-09	1.76E-09	1.29E-09
$p_{a,VI}$	8.77E-10	-2.28E-09	-1.02E-09	2.56E-09	2.50E-09	2.30E-09
$p_{d,VI}$	5.20E-10	6.80E-09	7.66E-09	2.13E-09	5.27E-09	8.49E-09
$p_{s,VI}$	4.31E-10	-1.43E-09	8.26E-09	1.35E-08	4.82E-09	7.24E-09

Table F.4: Statistics of the differences between the modelled and **adjusted** external data. The atmospheric model used is the NRLMSISE-00 and Goodman's method with $f = 3.6$ has been used to compute α.

G

Supplement to Chapter 7

G.1. Swarm C statistics biased by one large peak

While Fig. G.1 shows the peaks that bias the STD of the PCA of day 215, Table G.1 shows the STD of the PCA of day 215 when the peaks are excluded. The reduction in the three orbital directions are larger for the case with all the surface forces.

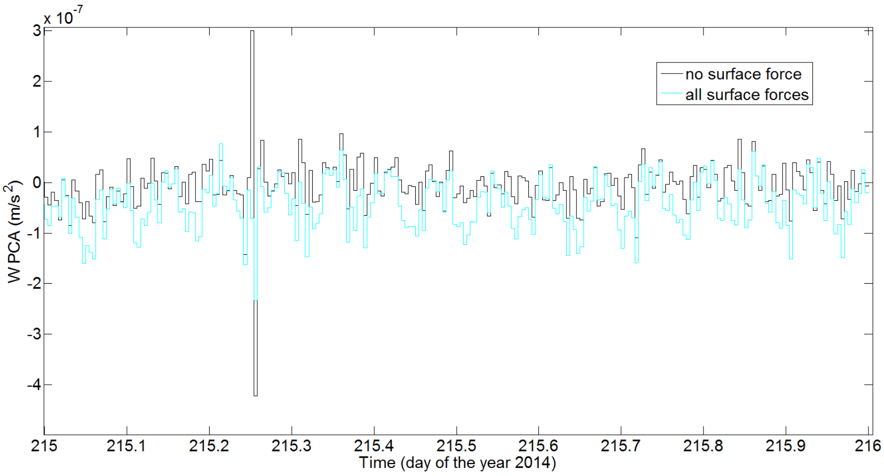

Figure G.1: Large peaks during day 215 that bias the statistics of Swarm C.

G.2. Larger view of the impact of the forces rescaling

Fig. G.2 shows that for various β_0 the SRP and atmospheric drag are dominating the cross-track acceleration of GRACE A. Indeed the Sun elevation angle above the orbital plane $\beta_0 \cong -20^\circ$ at day 214 and $\beta_0 \cong -43^\circ$ at day 235. Since a mismatch between the measured and modelled accelerations for GRACE A in cross-track direction has been revealed in Sec. 7.2, there is an issue with SRP or atmospheric drag. Similarly to Fig. 7.6,

Setting	Orbital axis	Peak	Peak removed
No surface force	R	4.72E-08	4.65E-08
	S	1.14E-07	1.12E-07
	W	5.02E-08	4.83E-08
All surface forces	R	5.72E-08	4.80E-08
	S	3.82E-07	3.65E-07
	W	4.95E-08	3.53E-08

Table G.1: Impact of two large peaks on STD of PCA of day 215 for Swarm.

Figs. G.3 and G.4 show the impact of manually scaling the SRP and aerodynamic forces (both the lift and the drag) on all the orbital axis. Fig. G.3 shows that when the measured accelerations are adjusted to the original modelled accelerations (on the left) or adjusted to the modelled accelerations with a rescaled SRP (on the right), the mismatch of the adjusted accelerations only appears in the cross-track direction. Similarly, Fig. G.4 shows the same trend when the aerodynamic forces (i.e. drag and lift) are rescaled.

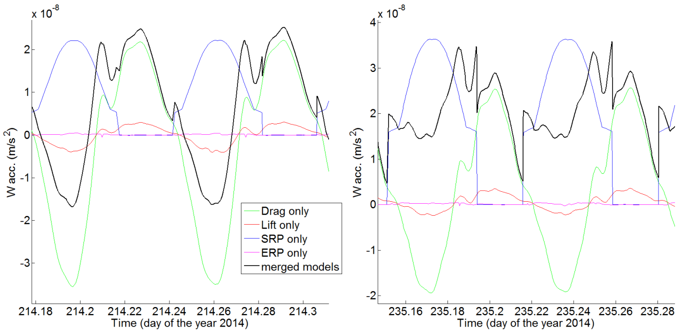

Figure G.2: Detail of the contributing forces to the cross-track accelerations of GRACE A. While ERP (in magenta) and lift (in red) have marginal impact on the resulting force (in black), SRP (in blue) and drag (in green) are the largest forces. Day 214 on the left and day 235 on the right.

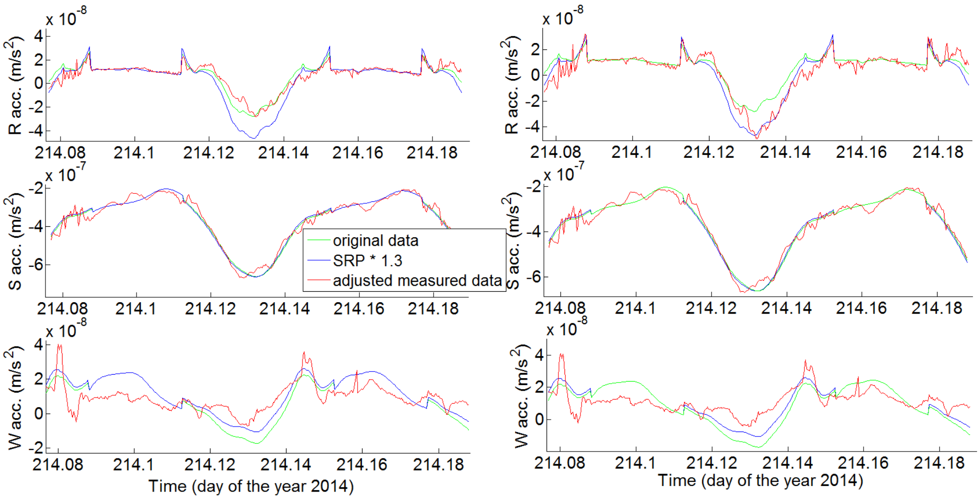

Figure G.3: Adjusted measured accelerations with the original modelled accelerations (on the left). Adjusted measured accelerations with the modelled accelerations when the SRP has been rescaled by 1.3 (on the right).

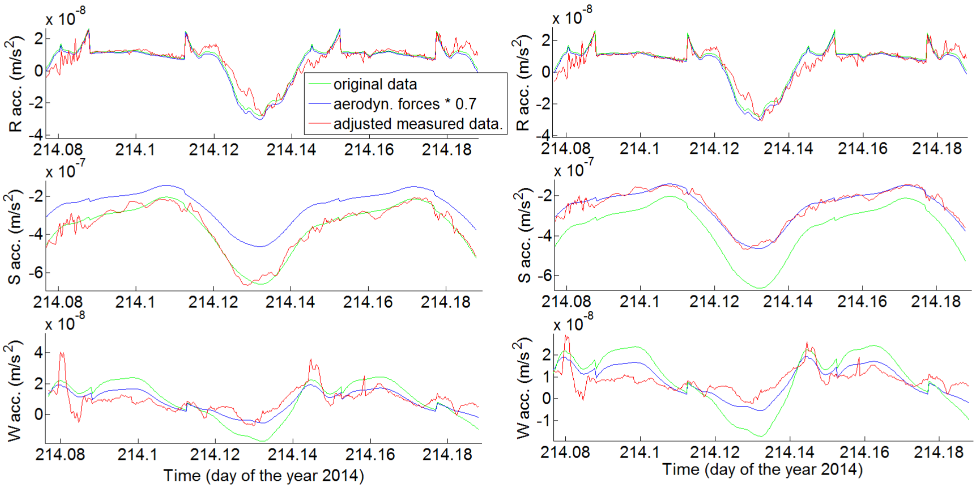

Figure G.4: Adjusted measured accelerations with the original modelled accelerations (on the left). Adjusted measured accelerations with the modelled accelerations when the aerodynamic forces have been rescaled by 0.7 (on the right).

H

FURTHER INVESTIGATIONS ON SRP

The individual influence of SRP has shown an undesired impact on the PCA of Swarm C and GRACE A. Here it is verified that it is not due to an issue with the modelled SRP. Table H.1 shows the *a posteriori* σ of unit weight m_0 (see Sec. 7.3 for more details about m_0) of different settings regarding the implemented forces. For GRACE A, the implementation of SRP alone increases m_0, so lowers the quality of the reduced-dynamic orbit! However, for both Swarm C and GRACE A the reduced-dynamic orbit is better when all the surface forces are implemented (including SRP) and when the SRP is excluded. This demonstrates that SRP is coupled with other forces and excluding one of the non-conservative forces could lead to a deterioration of the POD.

On the other hand, this does not explain why the radial axis of Swarm C suffers from an offset caused by SRP/ERP. In Chapter 6 it has been shown that setting all the panels of the satellite to a fully spectacularly reflecting behaviour lead to amplitude variation and a small offset of the SRP and ERP. Here, a more realistic modified macro-models has been used to further assess the influence of the optical properties. The nadir viewing surfaces of Swarm C (i.e. Nadir I, II and III panels, see Appendix C), have been set more reflective, assuming Kapton/aluminium optical properties (see Sec. 5.2). The reader should bear in mind that these changes are only made for better understanding of the effect of optical properties. Fig. H.1 and Table H.2 compare the PCA of two reduced-dynamic orbits: one with the original macro-models and another with the modified one. The reduced-dynamic orbit modelled with the modified macro-models have a lower mean PCA in the radial direction, a higher mean PCA in the cross-track direction and the standard deviation has marginally changed. This simple test shows that the macro-models properties may lead to mean PCA offsets. Since the optical properties of Swarm C have been assumed (see Sec. 5.2), then the larger mean PCA of Swarm C in the radial direction *could* be due to the use of inaccurate optical properties. Fig. H.1 shows the PCA offset due to the modified macro-models.

Setting	Swarm C mean value (mm)	GRACE A mean value (mm)
No surface force	1.9608	2.322
SRP only	1.9537	2.381
All surface forces but SRP	1.9301	1.565
All the forces	1.9266	1.467

Table H.1: Mean m_0 of the reduced-dynamic orbit of Swarm C and GRACE A

	Mean (m/s^2)			STD (m/s^2)		
Setting	**Radial**	**Along-track**	**Cross-track**	**Radial**	**Along-track**	**Cross-track**
No surface force	4.55E-08	-1.32E-07	-3.04E-08	4.96E-08	9.69E-08	4.51E-08
Original macro-models	4.90E-08	0.54E-07	-0.06E-08	4.64E-08	4.60E-08	3.51E-08
Modified macro-models	4.56E-08	0.53E-07	-0.11E-08	4.64E-08	0.459E-08	3.51E-08

Table H.2: Statistics of the piecewise constant accelerations of reduced-dynamic orbits using different Swarm C macro-models. They are computed based on the 23 sample days from day 213 to 236, except day 217, of year 2014.

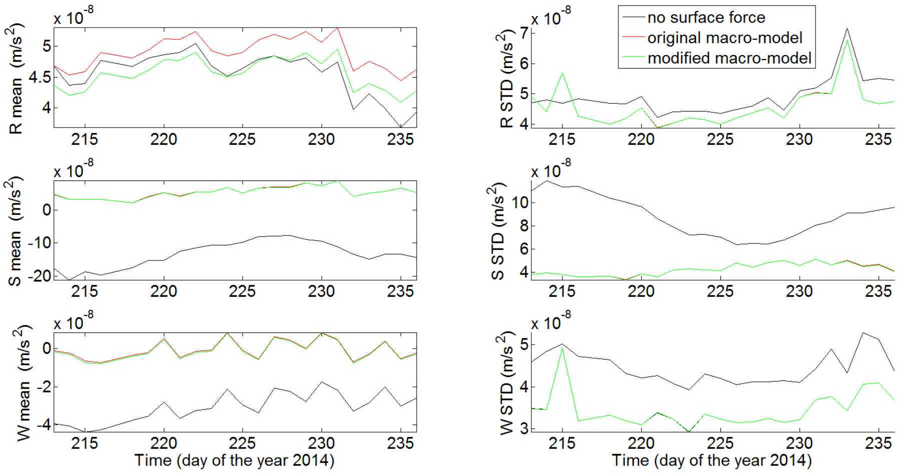

Figure H.1: Daily mean and STD of the piecewise constant accelerations of Swarm C. Impact of the modified macro-models, Nadir I, II and III panels have optical properties of Kapton/Aluminium (i.e. larger reflectivity than the original macro-models).

I

SUPPLEMENT TO CHAPTER 8

	No wind model		**HWM14**	
Accommodation coefficient	**NRLMSISE-00**	**DTM2013**	**NRLMSISE-00**	**DTM2013**
Goodman, $f = 2.4$	4.99E-08	4.97E-08	4.99E-08	4.97E-08
Goodman, $f = 3.6$	4.89E-08	4.87E-08	4.88E-08	**4.87E-08**
Pilinski, $k = 5.0$ E-17	4.99E-08	4.98E-08	4.99E-08	4.98E-08
Pilinski, $k = 7.5$ E-17	4.97E-08	4.96E-08	4.97E-08	4.95E-08

Table I.1: Mean piecewise constant accelerations in radial direction for various parametrizations for Swarm C, in m/s^2. Value with no surface force: 4.55E-08 m/s^2.

	No wind model		HWM14	
Accommodation coefficient	**NRLMSISE-00**	**DTM2013**	**NRLMSISE-00**	**DTM2013**
Goodman, $f = 2.4$	5.44E-10	1.11E-10	4.37E-10	0.03E-09
Goodman, $f = 3.6$	-5.61E-10	-9.36E-10	-6.54E-10	**-1.01E-09**
Pilinski, $k = 5.0$ E-17	-4.40E-11	-3.72E-10	-1.02E-10	-0.41E-09
Pilinski, $k = 7.5$ E-17	-3.40E-10	-6.54E-10	-3.95E-10	-0.69E-09

Table I.2: Mean piecewise constant accelerations in cross-track direction for various parametrizations for Swarm C, in m/s^2. Value with no surface force: -3.04E-07 m/s^2.

	No wind model		HWM14	
Accommodation coefficient	**NRLMSISE-00**	**DTM2013**	**NRLMSISE-00**	**DTM2013**
Goodman, $f = 2.4$	4.60E-08	4.57E-08	4.60E-08	4.58E-08
Goodman, $f = 3.6$	4.57E-08	**4.55E-08**	4.57E-08	**4.55E-08**
Pilinski, $k = 5.0$ E-17	4.58E-08	4.56E-08	4.58E-08	4.56E-08
Pilinski, $k = 7.5$ E-17	4.57E-08	4.56E-08	4.58E-08	4.56E-08

Table I.3: Standard deviation of the PCA in radial direction for Swarm C, in m/s^2. Value with no surface force: 4.96E-08 m/s^2.

	No wind model		HWM14	
Accommodation coefficient	**NRLMSISE-00**	**DTM2013**	**NRLMSISE-00**	**DTM2013**
Goodman, $f = 2.4$	3.51E-08	3.50E-08	3.51E-08	3.50E-08
Goodman, $f = 3.6$	3.51E-08	3.50E-08	3.51E-08	3.51E-08
Pilinski, $k = 5.0$ E-17	3.51E-08	3.50E-08	3.51E-08	3.50E-08
Pilinski, $k = 7.5$ E-17	3.51E-08	3.50E-08	3.51E-08	3.50E-08

Table I.4: Standard deviation of the PCA in cross-track direction for Swarm C, in m/s^2. Value with no surface force: 9.51E-08 m/s^2.

	No wind model		HWM14	
Accommodation coefficient	**NRLMSISE-00**	**DTM2013**	**NRLMSISE-00**	**DTM2013**
Goodman, $f = 2.4$	0.98E-08	9.82E-09	0.97E-08	9.36E-09
Goodman, $f = 3.6$	1.05E-08	9.50E-09	1.06E-08	9.36E-09
Pilinski, $k = 5.0$ E-17	1.06E-08	9.62E-09	1.07E-08	**9.32E-09**
Pilinski, $k = 7.5$ E-17	1.08E-08	9.66E-09	1.09E-08	9.42E-09

Table I.5: Mean piecewise constant accelerations in radial direction for various parametrizations for GRACE A, in m/s^2. Value with no surface force: 5.83E-09 m/s^2.

	No wind model		HWM14	
Accommodation coefficient	**NRLMSISE-00**	**DTM2013**	**NRLMSISE-00**	**DTM2013**
Goodman, $f = 2.4$	1.69E-08	1.65E-08	1.63E-08	1.58E-08
Goodman, $f = 3.6$	1.62E-08	1.59E-08	1.58E-08	1.58E-08
Pilinski, $k = 5.0$ E-17	1.66E-08	1.62E-08	1.61E-08	1.57E-08
Pilinski, $k = 7.5$ E-17	1.65E-08	1.61E-08	1.60E-08	**1.56E-08**

Table I.6: Mean piecewise constant accelerations in cross-track direction for various parametrizations for GRACE A, in m/s^2. Value with no surface force: 2.58E-08 m/s^2.

	No wind model		HWM14	
Accommodation coefficient	**NRLMSISE-00**	**DTM2013**	**NRLMSISE-00**	**DTM2013**
Goodman, $f = 2.4$	1.24E-12	1.16E-12	1.22E-12	1.15E-12
Goodman, $f = 3.6$	**0.89E-12**	0.85E-12	0.88E-12	1.15E-12
Pilinski, $k = 5.0$ E-17	1.15E-12	1.10E-12	1.13E-12	1.08E-12
Pilinski, $k = 7.5$ E-17	1.07E-12	1.02E-12	1.05E-12	1.01E-12

Table I.7: Standard deviation of the PCA in radial direction for GRACE A, in m/s^2. Value with no surface force: 3.44E-08 m/s^2.

	No wind model		**HWM14**	
Accommodation coefficient	**NRLMSISE-00**	**DTM2013**	**NRLMSISE-00**	**DTM2013**
Goodman, $f = 2.4$	1.24E-13	1.66E-13	1.17E-13	1.31E-13
Goodman, $f = 3.6$	1.09E-13	1.43E-13	1.04E-13	1.31E-13
Pilinski, $k = 5.0$ E-17	0.85E-13	1.14E-13	0.85E-13	0.89E-13
Pilinski, $k = 7.5$ E-17	0.84E-13	1.12E-13	0.84E-13	0.89E-13

Table I.8: Standard deviation of the PCA in cross-track direction for GRACE A, in m/s^2. Value with no surface force: 1.97E-08 m/s^2.

	No wind model		**HWM14**	
Accommodation coefficient	**NRLMSISE-00**	**DTM2013**	**NRLMSISE-00**	**DTM2013**
Goodman, $f = 2.4$	3.83E-09	3.93E-09	**3.74E-09**	3.85E-09
Goodman, $f = 3.6$	3.86E-09	3.92E-09	3.81E-09	3.85E-09
Pilinski, $k = 5.0$ E-17	3.82E-09	3.92E-09	3.75E-09	3.85E-09
Pilinski, $k = 7.5$ E-17	3.82E-09	3.91E-09	3.76E-09	3.85E-09

Table I.9: Standard deviation of the acceleration differences between the modelled and (daily calibrated) measured accelerations in radial direction for GRACE A. The unit of the acceleration differences is m/s^2.

	No wind model		**HWM14**	
Accommodation coefficient	**NRLMSISE-00**	**DTM2013**	**NRLMSISE-00**	**DTM2013**
Goodman, $f = 2.4$	9.30E-09	8.67E-09	8.54E-09	7.74E-09
Goodman, $f = 3.6$	7.19E-09	6.75E-09	6.57E-09	7.74E-09
Pilinski, $k = 5.0$ E-17	8.50E-09	7.90E-09	7.89E-09	7.14E-09
Pilinski, $k = 7.5$ E-17	8.01E-09	7.45E-09	7.42E-09	6.72E-09

Table I.10: Standard deviation of the acceleration differences between the modelled and (daily calibrated) measured accelerations in radial direction for GRACE A. The unit of the acceleration differences is m/s^2.